Exploration of Platelet and Mast Cell Communication: A Study of Membrane Lipids, Asthma, and Inflammation

A DISSERTATION
SUBMITTED TO THE FACULTY OF
UNIVERSITY OF MINNESOTA
BY

Sarah Melissa Gruba

IN PARTIAL FULFILLMENT OF THE REQUIREMENTS
FOR THE DEGREE OF
DOCTOR OF PHILOSOPHY

Christy L. Haynes, Advisor

May, 2016

Acknowledgements

My pathway to a Ph.D. would not have been accomplished without the support of many people who have mentored, collaborated, and supported me through the process. I am extremely thankful to my advisor Christy Haynes who helped develop my love of science and research through her mentorship and support. Her passion for science and attention to group dynamics has fostered an environment between the graduate students that inspire science discussion, collaboration, mentorship, and friendship that lasts beyond graduate school and gets you through failed experiments and when the HPLC is throwing a fit.

For this reason, I have been blessed to work with many great people who have made it fun to come to work every day with the random conversations and support and who I owe my thanks to. I'm especially grateful to my graduate student mentors Dr. Audrey Meyer, Dr. Secil Koseoglu, and Dr. Ben Manning who helped me learn both skills in lab and how to critically think about my research. I would also like to thank Dr. Solaire Finkenstaedt-Quinn who has been my platelet companion for the past four years and always available for platelet discussions, commiserating, loaning books, and walks to get free food and Yik Yak bling. I would also like to thank Joe Buchman, Dr. Katie Hurley, and Dr. Hattie Ring for keeping work lively through discussions about life, careers, the world, and for their support. Many of these people have contributed to the work presented in my thesis along with others; I would like to particularly thank Dr. Audrey Meyer for her work in chapters 4, 5, 6, 7, and 8; Dr. Ben Manning for work in chapters 7 and 8; Ben Meyer for helping with chapter 4 and 5; Xiaojie Wu who helped with chapters 1 and 6; Dr. Solaire Finkenstaedt-Quinn for her work in chapter 2; Dr. Dongyuk Kim for his work in chapter 4, Dr. Secil Koseoglu and Dr. Melissa Mauer-Jones for their help with chapter 3, and finally my undergrad Danielle Francis who worked on chapter 5. I would also like to acknowledge the other current and previous Haynes group members for their support and help.

Finally, I would like to thank the people who have helped me outside of lab including my parents Sheila and Steve for their love and support. I also want to acknowledge my neighbor Patrick who has spent many mornings and afternoon walking to and from work with me and his unique perspectives on life, stories about his dog, and support through my graduate career.

Dedication

This thesis is dedicated to my parents Sheila and Steve who have always been there to support my endeavors and celebrate my achievements.

Abstract

This work examines how environmental factors such as lipid membrane concentration, opioid agonist exposure, and inflammatory diseases impact cell communication. It explores the use of different cell models, specifically platelets and mast cells, to understand how disease states can impact cellular function. Throughout the thesis, a variety of analytical techniques including electrochemistry, mass spectrometry, dark field imaging, and microfluidics, are used to understand exocytosis, lipid concentration, manufactured inflammatory mediators, adhesion, and shape change in platelets and mast cells.

Platelets are cell-like bodies that travel through the bloodstream and are known for their role in hemostasis and diseases like stroke and myocardial infarction. They have also been implicated in inflammatory diseases such as asthma. In addition, their anucleate nature and easy isolation make them an ideal model for studying variations in cell communication upon the modification of their lipid content. Platelets communicate through the exocytosis of their three distinct granule types (δ, α, and lysosome). These granules contain molecules that assist in the transmigration of immune cells to the site of activation and help with additional platelet aggregation and adhesion.

In contrast, mast cells are found throughout the body in connective tissue and are one of the immune system's first lines of defense. They are primarily known for their role in allergies and asthma. Upon detection of antigens that they are sensitized to, the mast cell secretes manufactured chemokines and pre-formed granule mediators, including histamine and serotonin, calling other inflammatory cells to the site of infection.

Chapter One reviews single cell analysis techniques with a particular emphasis on the techniques used in this thesis, including electrochemistry and mass spectrometry.

Chapter Two through four are focused on understanding how variations in membrane lipids and structure affect platelet function and exocytosis in general. Chapter Two focuses on

understanding the variations that the fusion pore undergoes when granules are being exocytosed. Traditionally, a granule release event, monitored using carbon-fiber microelectrode amperometry, has a quick rise in current (spike) and gradual decay. The variations to this spike are classified as different forms of pre- and post-spike features and non-traditional granule secretion events. The role of cholesterol in changing the frequency and duration of these features is also discussed. Chapter Three discusses the role of phosphatidylserine (PS) in cellular communication using a platelet model. In this chapter, we explore how the stereochemistry of the head group and concentration of PS affects various platelet functions including granular content secretion, manufactured lipid release, and adhesion. The cholesterol level change upon addition of PS is also monitored. Finally, Chapter Four aims to understand how natural lipid variations affect cell function by comparing platelets from different species. This chapter highlights the importance of understanding your cell model relative to the actual cells involved in the disease or function being studied.

Chapter Five and Six progresses from lipid function into developing a better understanding of how platelets respond to their environment, particularly in the context of inflammatory diseases. Chapter Five's focus is on platelet response to opioids like those that are used in the treatment of pain due to inflammatory diseases, cancer, or surgery. Specifically, the effects on cell exocytosis as well as the presence of and role that opioid receptors play in platelets are characterized. Chapter Six focuses on studying how platelets respond to allergic asthma, including response to allergens and the chemoattractants (CXCL10 and CCL5) released during an asthma attack. Using bulk and single cell methods in conjunction allows us to obtain in-depth information on both the overall response and the granule fusion pore during exocytosis.

Chapter Seven and Eight focus on mouse peritoneal mast cell (MPMC) function in the context of inflammatory diseases including allergic asthma and neurogenic inflammation, respectively. Chapter Seven aims to state the importance of understanding the cell line you are using since variations in response to allergens are noted between commonly used mast cell models (rat basophilic leukocytes cell line and primary culture MPMC). In addition, MPMC response to CXCL10 and CCL5 was monitored. Finally, Chapter Eight explores the role of MPMC in neurogenic inflammation, a process wherein neurons release the neuropeptides substance P and calcitonin gene-related peptide. Mast cell response to these neuropeptides has been highly disputed, and this chapter focuses on the impact of IgE on MPMC bulk granular content secretion. It also aims to understand how these neuropeptides affect the fusion pore opening and closing during exocytosis.

Table of Contents

Chapter 1

Chapter 2

Chapter 3

Chapter 4

Chapter 5

Chapter 6

Chapter 7

Time- and Concentration-Dependent Effects of Exogenous Serotonin and Inflammatory Cytokines on Mast Cell Function……..106

Chapter 8

Analysis of Neuropeptide-Induced Mast Cell Degranulation and Characterization of Signaling Modulation in Response to IgE Conditioning……….. 123

List of Tables

Chapter 2

Chapter 3

Chapter 4

Chapter 7

List of Figures

Chapter 1

Chapter 2

Chapter 3

Chapter 4

Chapter 5

Chapter 6

Chapter 7

Chapter 8

List of Acronyms

5-HT, Serotonin	5-hydroxytryptamine
A23187	Calcimycin
AA	Arachidonic acid
AD	Alzheimer's disease
ACD	Acid citrate dextrose
ACN	Acetonitrile
ADP	Adenosine diphosphate
ANOVA	Analysis of variance
ATCC	American type culture collection
ATP	Adenosine triphosphate
β-Hex	β-Hexosaminidase
BCA	Bicinchoninic acid
BCS	Bovine calf serum
CARS	Coherent anti-stokes Raman scattering
CCL5	Chemokine ligand 5 (CCL5)
CFMA	Carbon-fiber microelectrode amperometry
CgA	Chromogranin A
CGRP	Calcitonin gene-related peptide
CMFDA	5-chloromethylfluorescein diacetate
CRL	Calcitonin receptor-like receptor
CXCL10	C-X-C motif chemokine 10
CXCL12	C-X-C-motif chemokine 12
D-PS	Phosphatidyl-D-serine
DAMGO	[D-Ala^2, N-MePhe^4, Gly-ol]-Enkephalin
DPDPE	[D-Pen^{2,5}]Enkephalin, [D-Pen^2,D-Pen^5]Enkephalin
DMEM	Dulbecco's Modified Eagle Medium
EDTA	Ethylenediamine tetraacetic acid
ELISA	Enzyme-linked immunoassay
FA	Formic acid
FcεRI	High affinity IgE receptor
FcεRI	Low affinity IgE receptor
FET	Field effect transistors
FSCV	Fast scan cyclic voltammetry
fMLP	*N*-Formylmethionyl-leucyl-phenylalanin
HEPES	N-2-hydroxyethylpiperazine-N'2-ethanesulfonic acid
HPLC	High performance liquid chromatography
IPA	Isopropyl alcohol
KO	Opioid receptor knockout mouse model
L-PS	Phosphatidyl-L-serine
LT	Leukotriene
LTB$_4$	Leukotriene-B$_4$
LTC$_4$	Leukotriene-C$_4$
LTD$_4$	Leukotriene-D$_4$
LTE$_4$	Leukotriene-E$_4$
MeOH	Methanol
MAF	Maximum autocorrelation factor analysis

MβCD	Methyl-β-cyclodextrin
MALDI	Matrix assisted laser desorption
MD-SIMS	Multi-dimensional secondary ion mass spectrometry
MetA-SIMS	Metal-assisted secondary ion mass spectrometry
MPMC	Mouse peritoneal mast cell
MS	Mass spectrometry
MSI	Mass spectrometry imaging
NKR	Neurokinin family of receptors
NTE	Non-traditional events
OCS	Open canalicular system
PAF	Platelet activating factor
PBS	Phosphate-buffered saline
PC	Phosphatidylcholine
PCA	Principle component analysis
PDMS	Polydimethylsiloxane
PE	Phosphatidylethanolamine
PF4	Platelet factor 4
PG	Prostaglandin
PGD_2	Prostoglandin-D_2
PGE_2	Prostaglandin-E_2
PRP	Platelet rich plasma
PS	Phosphatidylserine
RBL	Rat basophilic leukocytes
RSD	Relative standard deviation
SD	Standard Deviation
SEM	Standard error of the mean
SERT	5-HT specific reuptake transporter
SIMS	Secondary ion mass spectrometry
SM	Sphingomyelin
SP	Substance P
SRM	Selective reaction monitoring
TBS	Tris buffered saline
TBS/T	Tris buffered saline with Tween-20
TEM	Transmission electron microscopy
TG	Tris/glycine
TGS	Tris/glycine/SDS
TNP-Ova	2,4,6-trinitrophenol-ovalbumin
TOF	Time-of-flight
TQD	Triple quadrupole mass spectrometry detector
UPLC	Ultra-performance liquid chromatoraphy
UPLC-MS/MS	Ultra-performance liquid chromatography-tandam mass spectrometry

Chapter 1: Single Cell Analytical Techniques

This work was completed with the assistance of Xiaojie Wu who wrote parts of the introduction and conclusion and Christy Haynes. Editing was assisted by Solaire Finkenstaedt-Quinn and Joseph Buchman

1.1 Overview

Analysis of the fundamental mechanisms underlying cellular behavior and function is one of the top priorities in cell biology and medicine. Conventional measurements based on pooled cell populations obscure detailed information about the biological events taking place inside single cells as well as important outlier cell subpopulations in a homogenous cell culture. Recent progress in single cell analysis techniques allows for the quantification of intracellular biological molecules as well as the characterization of dynamic cellular processes with spatiotemporal resolution. These techniques reveal nuances in cellular function and enable the detection of unknown cell subpopulations that are highly correlated to functional variations in tissues or organs caused by disease pathogenesis. This chapter covers single cell electrochemical and mass spectrometry methods, limitations of these methods, recent research to overcome these limitations, and the recent advances in cellular biology made using these techniques. Single cell microscopy and spectroscopy will not be discussed.

1.2 Introduction

With the rapid development of new analytical techniques, the focus of biophysical and analytical chemistry has gradually shifted from investigating cellular behavior of bulk cell contents to performing analysis at the single cell level. The motivation for this shift is attributable to two major factors. First, single cell analysis is one of the best ways to dig deeply into the features of a particular cell type, often revealing real-time behavior or quantitative information. Second, even within a largely homogeneous cell population, subtle microenvironments or inherent stochastic factors in a small sub-population of cells may reveal cell cycle malfunction or disease state transition.[1, 2] Exploration of these heterogeneities using single cell analysis not only reveals mechanistic insights into the cellular behavior, but also elucidates the relationship between cell-specific changes and biological phenomena pertaining to disease-related dysfunction. In recent years, state-of-the-art single cell techniques have been used to characterize intracellular events pertaining to genes, proteins, metabolites, and organelle function, as well as subcellular dynamics, cell communication, and pharmaceutical effects.

This chapter provides an overview of several single cell techniques with particular focus on the techniques used throughout this thesis, including limitations, and recent advances. The electrochemical techniques covered include cyclic voltammetry, amperometry, field effect transistors, and patch clamp recording, with an emphasis on monitoring cellular communication and a discussion on micro- and nanoelectrodes. The mass spectrometry section will focus on both the imaging based approaches, matrix assisted laser desorption ionization and secondary ion mass spectrometry for the analysis of cell structure and drug metabolism and uptake, and mass cytometry for the quantification of proteins on individual cells. This review concentrates largely on advances in detection techniques rather than single cell sampling approaches (e.g. microfluidic platforms). However, several relevant cell sampling approaches for each technique are mentioned and detailed information on microfluidics in single cell analysis can be found in other reviews.[3-5]

1.3 Electrochemistry

Single cell electrochemistry is a powerful method to monitor cellular communication proceeding either through exocytosis, a process wherein a chemical messenger-filled granule fuses to the cell membrane, or ion channel release. Single cell electrochemical methods have also been employed to monitor various intracellular processes including oxidative stress and oxygen consumption.[6, 7] With the use of microelectrodes and nanoelectrodes, real-time monitoring of extracellular communication and intracellular contents can occur with minimal cell damage, even after puncturing the cell wall.[8, 9] In addition, the small electrode surface area reduces the current needed to maintain the potential causing a reduction in noise compared to larger electrodes. An increased temporal resolution is also available due to a corresponding decrease in the electrical double layer (a layer of counter ions followed by a diffuse layer, consisting mostly of counter ions which surround the electrode surface and hinder the ability for an electroactive molecule to come into contact with the electrode).

The use of microelectrodes dates back over half a century. By 1958, the use of carbon rods had already been established; however, they were difficult to manufacture. To overcome this difficulty, Ralph Adams developed a carbon paste which allowed electrodes to be produced in five minutes while still maintaining the accuracy of the electrode for several runs.[10] In addition to carbon, microelectrodes are primarily made from boron-doped diamond material or encasing metals such as platinum and gold in an insulating layer.[11,12] However, due to carbon's high sensitivity, large potential range, stability, and biocompatibility with cells, many microelectrodes used to study cells are carbon based.[13, 14] In particular, carbon-fibers have been the primary choice for microelectrodes since they were first developed in 1979. They were further optimized for use in studying single cell exocytosis, in the Wightman group, due to their capacity to support fast scan rates, their low cost, and ease of manufacture.[13-16] To increase specificity and enable the detection of non-electroactive compounds, various groups functionalize the carbon surface.

Recent papers include modifications with platinum or enzymes for monitoring O_2, H_2O_2, glucose, and other non-electroactive enzyme substrates.[8,17] More in-depth information on both recent electrode modifications and the effects of electrode geometry can be found in the following reviews. [11,18,19]

1.3.1 Fast Scan Cyclic Voltammetry

Common electrochemical techniques, including cyclic voltammetry and amperometry, have been used to monitor exocytosis in a variety of cells including PC12 cells, mast cells, chromaffin cells, and platelets.[20-23] Fast scan cyclic voltammetry (FSCV), which capitalizes on the relatively broad range of reactivity of carbon, is used to confirm the molecular identity of cell-secreted species by comparison to known voltammograms. In FSCV, the current is varied at a scan rate ranging from 300 to several thousand volts/second, with a repetition rate of 10 scans per second for brain studies to several hundred scans per second (Hz) in cells with one electroactive compound.[24-27] The quickly changing voltage causes surface-associated and capacitive currents. To correct for this interference, a background voltammogram is recorded prior to stimulation and subtracted from the subsequent sweeps.[28] The collected voltammograms are combined to form a false color voltammogram revealing temporal data and achieving chemical species confirmation and quantitation, all of which are useful when studying complex environments such as the brain. Many recent advances in FSCV have looked at overcoming limitations including balancing the amount of data collected with the high time resolution, eliminating interference from electroactive molecules that obscure the molecules of interest, and calibration of electrodes for *in vivo* experiments.[27, 29-31]

Comparable techniques have scan rates less than 10 Hz, meaning that cyclic voltammetry starts off with better temporal resolution. However, to capture most real-time cell-cell communication, a higher scan rate is often needed, thus increasing the amount of data needing storage, hindering the ability to quickly transfer the data wirelessly, and increasing the energy consumption limiting the lifetime of the device. The balance between data storage and the scan rates needed for meaningful biological measurements has been considered by several groups. Kile et al. studied FSCV repetition rates in brain cells of live rat models and highlighted the difference in results between the standard 10 Hz collection data vs. 60 Hz. The increased collection rate at 60 Hz showed increased sensitivity without decreasing detection levels when accounting for collection time compared to 10 Hz. The 60 Hz collection rate also allowed for faster detection of dopamine release, and the re-uptake time was shown to be 18% quicker than that determined when using the 10 Hz repetition rate. However, no difference was noted between the 10 and 60 Hz collection rates when they studied cells that had slower re-uptake and release times.[29] Amos et al. compared 10 Hz to 1 Hz collection rates for both *in vivo* and *in vitro* studies. Their data indicated that at 1 Hz, the electrode was stable for 8 hours without a change in the limit of detection, and the data gathered was comparable to the 10 Hz experiment.[27] Therefore, to gather the most relevant information, it is important to understand your data capacity but also the analyte adsorption/desorption kinetics when performing FSCV experiments.

In addition to changing the collection rate, the waveform (a pattern that determines what potential will be held on the electrode at each time point) can be modified to enhance the detection of the molecules of interest. Recently, Schmidt et al. created a modified sawhorse waveform to quantify small tyrosine-containing peptides, which typically oxidize at higher potentials than catecholamines, to better understand the role of opioid peptides. The waveform increased at 100 V/s from -0.02 V until 0.6 V and then increased to 400 V/s from 0.6-1.2 Volts where it remained stable for 3 ms and then decreased voltage at 100 V/s. With the traditional waveform, the oxidation of catecholamines masks the detection of peptides. With the modified waveform, the initial slow increase in voltage within the catecholamine's oxidation potential range helps decrease the current produced due to catecholamine oxidation and causes the oxidation of dopamine to occur at 400 mV, minimizing interference. Fouling is also decreased by holding the potential constant for 3 ms.[30]

Homemade electrodes used for FSCV have high variability in their performance, requiring calibration for quantification of the molecule of interest. Post calibration is often difficult or impossible. To counteract this difficulty, Roberts et al. developed a method to calibrate the electrode using the background charging current. This approach was validated by comparison to traditional post calibration methods. Another advantage of this method is that it can be done at any point during the experiment, which is ideal for experiments that span hours or several days, where the electrode may decrease or increase sensitivity over time.[31]

1.3.2 Carbon-Fiber Microelectrode Amperometry

Carbon-fiber microelectrode amperometry (CFMA) is known for its high temporal resolution which facilitates in-depth studies of exocytotic biophysical variations due to drugs, environment, or membrane components. CFMA is capable of sub-microsecond time resolution detection of redox-active species at a fixed potential and has been used with a variety of cell types, including mast cells, chromaffin cells, platelets, PC12 cells, and more recently BON cells (cells derived from a human carcinoid tumor) and Weibel-Palade bodies from endothelial cells.[22, 32-35] In this technique, an electrode is placed near the surface of a cell, and the change in current is measured over time. As the redox-active species is oxidized or reduced, the current change will be recorded as a spike. Close inspection of the spike enables kinetic measurements of each granule's fusion pore opening time (T_{rise}, time from 10% to 90% of the current spike height), the slope of the rise time ($T_{slope,}$ how fast the electroactive molecules initially come out of the fusion pore), the fusion event duration ($T_{1/2}$, full width at half max), and decay time (the time it takes for the spike's decay). By measuring the area (Q) underneath the spikes in the typical time vs current amperometric trace, the total moles of electroactive molecules secreted can be calculated using Faraday's Law. Finally, the stability of the fusion pore opening and closing can be measured by looking at the features that deviate from the standard current spike, termed a foot (Fig. 1.1A).[13, 36]

Typical limitations of CFMA include the inability to identify the oxidized or reduced molecule. To minimize this limitation, initial experiments on uncharacterized cell lines utilize CV to determine the molecules being secreted before conducting amperometry experiments. However, this method does not allow you to quantify the amount of each molecule being secreted if two or more molecules are secreted that oxidize at the potential being measured. One way to remove this problem is modifying your electrode surface to be selective for the molecule of interest or lowering the potential so that only one of the molecules will be oxidized. Finally because of these limitations, CFMA measurements are often limited to *in vitro* studies.

Research using CFMA has focused on the fundamental aspects of cell communication, including how membrane components such as proteins and lipids impact exocytosis and how cell communication changes in response to various diseases and drugs. One area of recent interest has been focused on understanding what cell membrane components affect the fusion pore opening and closing kinetics in granule secretion events.[37-40] In addition to looking at kinetics, the stability of the fusion pore can be studied by analyzing pre, post, and non-traditional secretion events. Fig. 1.1A demonstrates an example of a traditional secretion event with both pre- and post-spike feet, which can indicate that the current fusion pore state may not be efficient in opening or closing, respectively. In a recent paper by Finkenstaedt-Quinn et al., the different types of these events were classified and compared to previous literature.[36] In PC12 cells, and more recently, platelets, it was discovered that pre-spike foot events can be characterized as a ramp, plateau, or combination of both. In PC12 cells a correlation between flux in the pre-foot and the flux in the spike was noted.[36, 41]

Recent advances on the role of lipids in exocytosis have also been studied using CFMA. The role of cholesterol on fusion pore stability has been demonstrated by Finkenstaedt-Quinn et al. who analyzed the changes in foot features and non-traditional events. These data show that the percent of platelets with foot features increased as cholesterol levels increased (Fig. 1.1B). This was primarily due to a greater number of platelet granules undergoing non-traditional secretion (Fig. 1.1C).[36] The roles of phospholipids including phosphatidylethanolamine (PE) and phosphatidylserine (PS) on fusion pore kinetics and secretion have been studied in PC12 cells and platelets. Results show that PE incubation causes changes in PC12 cell granule secretion time, and PS incubation caused changes in both platelet and PC12 cell secretion. In platelets, PS induced longer $T_{1/2}$ time and had a greater number of pre-spike features. In PC12 cells, the number of granules secretion events changed.[20,42] These differences suggest that the role phospholipids play in the exocytosis process changes depending on the cell type.

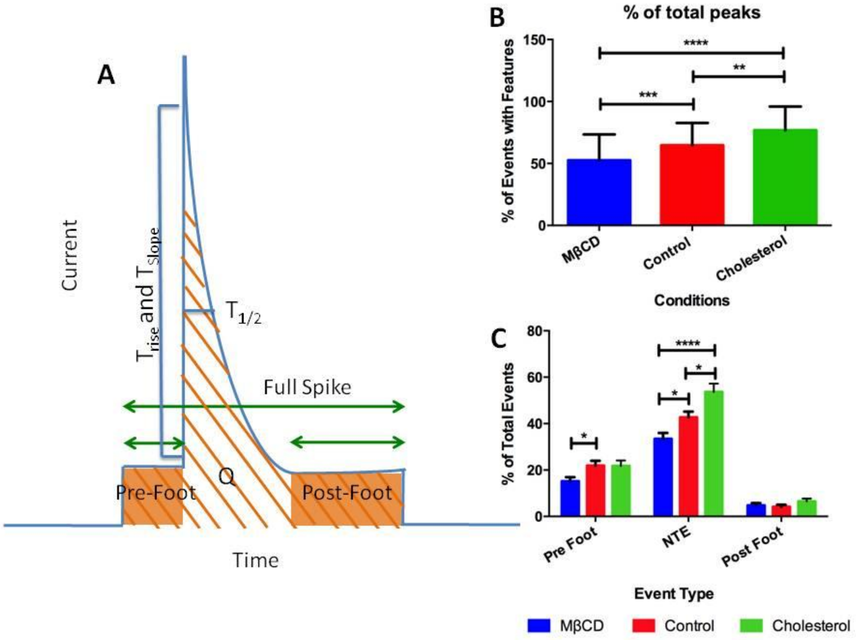

Figure 1.1 Pre and post foot schematic and variations in spike features due to cholesterol. (A) Diagram indicating the parameters used to categorize and quantify various spikes. (B) The frequency of events with features upon the different cholesterol treatments. (C) Relative frequency of classes of spikes with the different cholesterol treatments. ($*p \leq 0.05$, $**p \leq 0.01$, $***p \leq 0.001$, $****p \leq 0.0001$) This figure was adapted with permission from Finkenstaedt-quinn et al.[36] Copyright 2016 Elsevier

CFMA has also been used to study the effects of various diseases-associated stimulants on exocytosis. Mast cells, a type of immune cell involved in asthma, exhibit secretion of serotonin when exposed to the common chemoattractants, CXCL10 and CCL5. This secretion was marked by decreased serotonin secretion and elongated T_{rise} and $T_{1/2}$ when compared to the allergic reaction pathway exocytotic events.[43] Single cell CFMA can also be used to understand how diseases impact cell communication by comparing cells in a disease model to control cells. Manning et al. studied the effects of sickle cell disease on mast cells. Mast cells, associated with sickle cell disease, had impaired serotonin secretion and variations in their biophysical kinetics. However, mast cells from sickle cell mice treated with morphine did not show a difference relative to control mice.[44]

1.3.3 Field-Effect Transistors

Field effect transistors (FET) can be used for the detection of electroactive or non-electroactive compounds with the use of antibodies for target molecules. FETs consist of a source, a gate, and a drain. A voltage is applied to the gate, which can be functionalized with antibodies specific to a non-electroactive molecule or protein of interest, changing the conductivity between the source and gate. Upon detection of the molecule or protein of interest, the conductivity change causes a measurable change in current between the source and drain. One type of FET used for single cell exocytosis analysis is a single-walled carbon nanotube FET modified with anti-chromogranin A (CgA). CgA has several important biofunctions including neuron inflammation mediation, assisting in the secretion of biomoleucles after Ca^{2+} chelation, and is hypothesized to be a marker for neurodegenerative diseases. The use of FETs for measuring the secretion of CgA has been shown to be highly biocompatible, sensitive to low secretion concentrations, and displays a correlation between conductivity and concentration in both neurons and single chromaffin cells.[45, 46]

Two recent expansions on FET platforms were demonstrated for studying cellular processes, other than exocytosis. The researchers were interested in understanding the adhesion, apoptosis, and detachment of single cancer cells in response to nanoparticles and anti-cancer drugs. To monitor this, they used impedance spectroscopy with an ion-sensitive field-effect transistor.[47-49] Zhang et al. created a nanometric FET by coating a dual electrode for the source and drain, with polypyrrole to form the transistor channel with a final diameter of 200 nm (Fig. 1.2). The pH sensor detects changes of ~0.1 pH units with a linear response between pH 5.0-7.5. The probe was used for the detection of pH in breast cancer tissue, a cluster of melanoma cells, and on a single cancer cell (Fig. 1.2 G-I). Typically melanoma cells have higher acidic environments. Researchers found that the probe is able to measure an increase in acidity in both the tissue and cluster of melanoma cells as it approached the cells. However, no decrease in pH was noted on a single cell level, which was likely due to the rapid diffusion of the proton not obstructed by other cells.[50] With the addition of hexokinase (an enzyme that cleaves ATP and releases protons) to the tip of the nanometric-FET, the researchers also showed the applicability of this probe to detect the release of ATP at concentrations as low as 10 nM.[50]

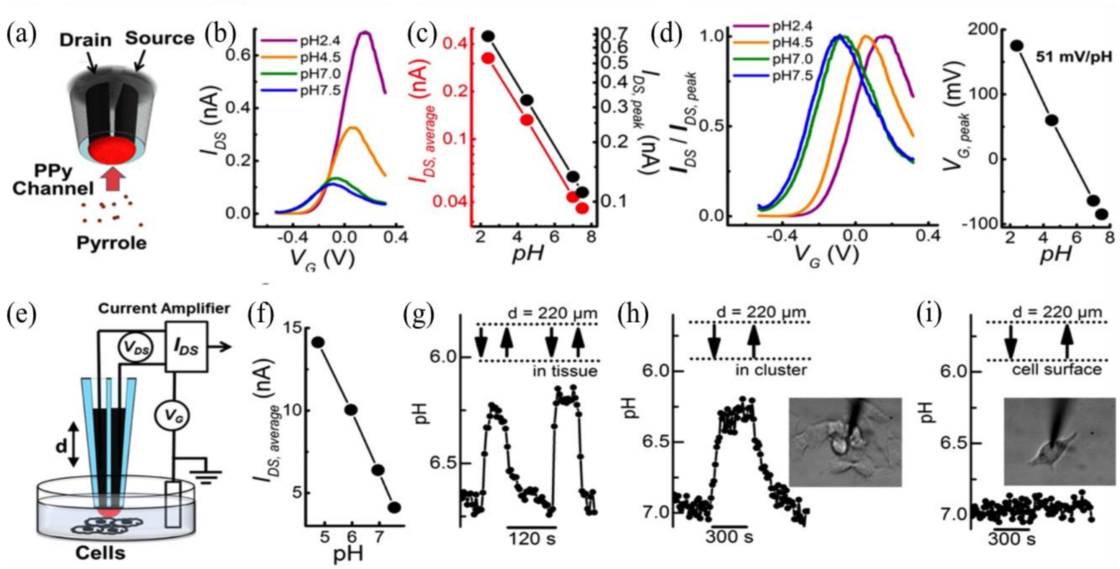

Figure 1.2 Nano-FET pH Biosensor. (a) A spearhead nano-FET made by deposition of polypyrrole (PPy) to comprise the channel. From I−V_G curves (b), changes in pH value can be measured as change of average drain-source current or drain-source spike currents (c) as well as shift in gate voltage (d). (e) The pH-sensitive PPy nano-FET is applied to measure the local pH in the microenvironment of cell samples. (f) Prior to cell measurements the PPy nano-FET is calibrated with physiological pH variations from 5.0 – 7.5. Local pH measurements by alternating vertical approach and withdrawal of the PPy nano-FET probe to breast cancer tissue (g), a cluster of melanoma cells (h), and a single melanoma cell (i).Adapted with permission from Zhang, et al. Copyright 2016 American Chemical Society[50]

1.3.4 Patch Clamp

Unlike the previously discussed methods, patch clamp measures cell capacitance, which is proportional to the membrane area. In patch clamp, a gigaseal is formed between the cell and an electrolyte-filled pipette; this serves to reduce the noise and prevents interference from ions in the extracellular solution. There are two major patch clamp methods. The first is cell-attached, where the capacitance is measured on a small area of the cell. This technique has lower noise and greater sensitivity to small changes.[51,52] The other methods is a whole-cell method, which allows measurements of the entire cell's capacitance and can measure larger changes in area. This method is completed by puncturing the cell membrane with the pipette. To obtain more in-depth information on exocytosis, patch clamp can be utilized in parallel with amperometry to obtain both fusion pore size and molecular secretion information.[51, 53]

Finally, patch clamp can be used for measuring the release of ions from ion channels located throughout the plasma membrane. Upon stimulation, the ion channels open, selectively allowing ions to pass through based on charge and size, creating an electrical signal. In these studies, the gigaseal is formed over the ion channel(s) of interest, and the potential is held constant in the pipette. As ions pass through, the change in current from the potentiostat is measured. [54]

One of the largest problems with patch clamp is the scale-up of single cell measurements *in vivo* on a large scale, particularly in the brain to study the effects of drugs and disease on brain signaling because of the human hours needed for electrode placement. Training personnel to operate the patch clamp can also be time consuming. To start overcoming these limitations, Kodandaramaiah et al. developed an automated whole cell patch clamp system. In 3-7 minutes, the robot is able to fully patch clamp neurons with a success rate of 32.9%, which is higher than the success rate for trained personnel at 28.8%. The resulting data was found to have a similar quality relative to manual patch clamp.[55]

1.4 Mass Spectrometry

Mass spectrometry (MS) is a technique used to analyze the molecular species present in a cellular sample via the ionization and subsequent detection of fragment ions. Due to the detection method, MS often does not require labeling of the species of interest, allowing for both the detection of known and unknown ions, without theoretically limiting the number of different ions detected (accounting for the range of masses and resolution of the instrument). Mass spectrometers can be directly coupled with microfluidic devices, liquid chromatography, capillary electrophoresis, cell pressure probes, and nanoelectrospray tips.[2,56-58] Recently, Aerts and colleagues made whole cell patch clamp measurements, then collected the intracellular contents for later analysis by MS.[59] One lab that is particularly focused on direct measurements of live cells is the Masujima lab at the Riken research institution in Japan. They have developed and optimized live single cell MS where specific organelles, the nucleus, or cytoplasm can be removed after a cellular event and routed directly into the MS to analyze metabolites.[60]

1.4.1 Mass Spectrometry Imaging

To directly measure single cells within tissue samples, many researchers use MS imaging (MSI). MSI consists of a secondary ion MS (SIMS) and matrix assisted laser desorption ionization (MALDI) setup.[61,62] These techniques allow for the detection of molecules, proteins, and unique lipid compositions that could be obscured in bulk analyses.

In static SIMS and dynamic SIMS, the species on the top layer of the cell or several layers in the cell, respectively can be identified. Dynamic SIMS is advantageous in that it gives a 3D picture of the cellular components. The bombardment of the surface with high energy particles (typically Cs^+ or O^-) or clusters (Bi_3^+ and C_{60}^+), allow for the desorption of atoms, molecules, and clusters. The secondary ions produced from this process are then analyzed.[63,64] The layer thickness is typically several nanometers with a lateral resolution of ≤100 nm and attomolar detection limits. This high spatial resolution allows the concentration of various membrane components, including lipids and polysaccharides, to be analyzed on a single cell level. Medically, this can be used to understand the impacts of disease on cellular membrane components or reveal disease biomarkers. It can also be used to understand drug distribution.

Park et al. modified the traditional time-of-flight (TOF)-SIMs method to better differentiate ovarian cancer cells from control cells by using multi-dimensional SIMS (MD-SIMS).[65] In this method, samples first undergo TOF-SIMS then have gold deposited on them before a second SIMS analysis (metal-assisted-SIMS (MetA-SIMS)). The data showed that TOF-SIMS and MetA-SIMS identified 206 and 533 unique compounds, respectively and 426 compounds were found in both methods with 250 signals enhanced using MetA-SIMS compared to TOF-SIMS. When comparing the results between cancerous and non-cancerous tissue using partial least square discriminate analysis, MD-SIMS enhanced the number of cancer cells discriminated from non-cancer cells from 68.4% with TOF-SIMS to 82.6%. (Fig. 1.3). [65]

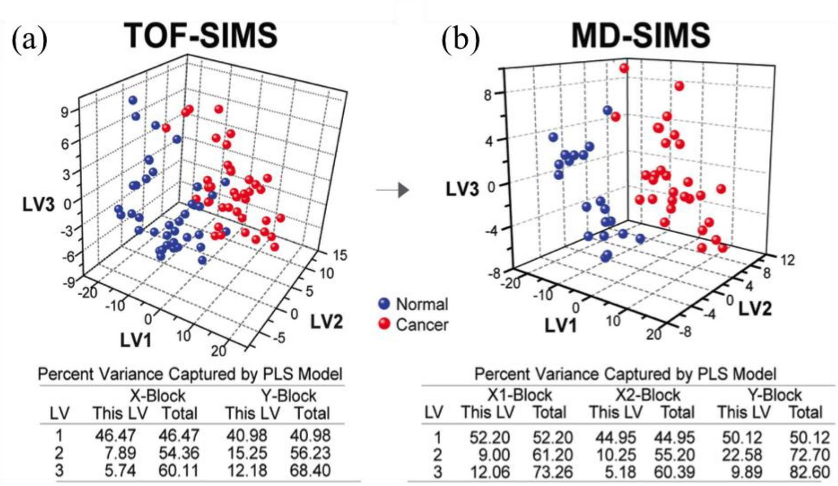

Percent Variance Captured by PLS Model

	X-Block		Y-Block	
LV	This LV	Total	This LV	Total
1	46.47	46.47	40.98	40.98
2	7.89	54.36	15.25	56.23
3	5.74	60.11	12.18	68.40

Percent Variance Captured by PLS Model

	X1-Block		X2-Block		Y-Block	
LV	This LV	Total	This LV	Total	This LV	Total
1	52.20	52.20	44.95	44.95	50.12	50.12
2	9.00	61.20	10.25	55.20	22.58	72.70
3	12.06	73.26	5.18	60.39	9.89	82.60

Figure 1.3 Integrated analysis of TOF- and MetA-SIMS datasets. 3-D partial least square-discriminate analysis score plots for TOF-SIMS (a) and MD-SIMS (b). The tables show that MD-SIMS enhanced the power of discrimination of ovarian cancer samples (red) from normal samples (blue), compared to TOFSIMS. This figure was adapted from Park, et al. Copyright 2015 Nature Publishing Group [65]

Variations in the way data was analyzed was compared to distinguish which method is better able to detect variations between injured or diseased and control cells. Hanrieder et al. imaged human spinal cord in positive and negative mode.[66] The data was subjected to either principal components analysis (PCA) or maximum autocorrelation factor analysis (MAF) to perform unsupervised multivariate statistical image analysis. Both PCA and MAF separated and correctly characterized gray and white matter in the spinal cord. However, MAF was able to better distinguish sub-regions and regions with slight heterogeneities due to cell damage. One disadvantage to MAF is the length of time for computation making it better suited for smaller scale images. [66]

Being able to detect the drug distribution and metabolism inside a cell is important to drug efficacy. To locate and distinguish organelles of interest within a cell, Bloom et al. established a new technique using dye-enhanced imaging. This technique uses a molecular tag that is detectable by SIMs, but does not interfere with the mass spectra of other common cellular components. Using a nuclear stain, it was verified that the stain was successfully chemically imaged. Utilizing this method, further studies can probe various biological pathways and drug uptake, while being able to detect organelles of interest. Future work on other organelle stains still need to be verified.[67] Bloom et al. have used cluster SIMS for detecting the uptake and location of nanoparticles and subsequent delivery and degradation of the delivered drug within the cell. [68]

One limitation of SIMS is that it does not give information on the roughness of the material, such as the presence of protrusions, or differentiate between patchy and continuous signals. To enhance image quality and overcome these limitations, Tarolli et al. paired SIMs data with scanning electron microscopy. By using a pan-sharpening algorithm, their results provide both topographical information and chemical information. This approach was used to understand how the environment impacts the adhesion of *B. braunii* algal cells, known for their role in biofuels. The data collected helped clearly define cellular boundaries in the biological matrix. [69]

Another limitation is that not every cellular component and molecule can be detected by TOF-SIMS. There are a variety of reasons leading to this limitation, but a major cause is extensive fragmentation of the target molecules. To combat this, Carlred et al. developed a method to detect peptides that undergo extensive fragmentation which utilizes antibody-coupled liposomes.[70] They paired this method with TOF-SIMS to understand where amyloid-β, a peptide associated with Alzheimer's disease (AD), is located in the brain with respect to various lipids. Unlike traditional immunohistochemistry fluorescence imaging methods, this allowed for the detection of small structures located on the surface, which may be hidden in traditional methods due to fluorescence within the tissue, and resulted in a greater number of biological structures being measured. Their findings indicate that in AD mouse models, there are large buildups of amyloid-β in the hippocampus region (Fig. 1.4) with decreased levels of phosphatidylcholine signal.[70]

Unlike SIMS, MALDI samples need to be prepared in a matrix that is ionized using a near UV laser (337-355 nm). The analyte molecules absorb the energy from the matrix, resulting in an ion plume which enters the mass spectrometer for analysis. This technique is often used when analyzing tissue rather than single cells due to its poor large lateral resolution of 20-30 µm. However, techniques to enhance the resolution have included using a scanning microprobe MALDI mass spectrometer and transmission geometry MALDI mass spectrometer, both of which have lateral resolutions around 1 µm.[71,72] Despite these improvements in the resolution limit, many of the recent advances in MALDI single cell analysis involve the use of cell separation before performing MALDI mass spectrometry. Xie et al. created a microwell array microfluidic device for automatic and high throughput phospholipid detection in individual A549 lung cancer

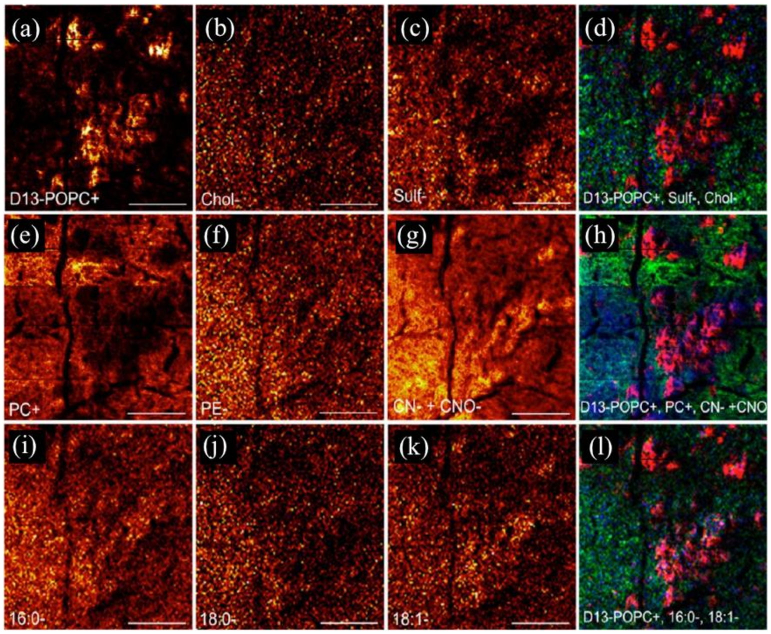

Figure 1.4 High resolution TOF-SIMS images of liposomes bound to 6E10-labeled amyloid-β deposits and selected lipids in transgenic Alzheimer's disease mouse brain tissue. (a) deuterated POPC (1-palmitoyl-2-oleoyl-sn-glycerol-3-phosphocholine-1,1,2,2-d4-N,N,N-trimethyl-d9) liposomes, (b) cholesterol (Chol−), (c) sulfatides (Sulf), (d) overlay showing liposomes (red), sulfatides (green) and cholesterol (blue), (e) phosphatidylcholine (PC), (f) phosphatidyletanolamine (PE), (g) CN− and CNO− ions, (h) overlay showing liposomes (red), PC (green) and CN− + CNO− (blue), (i) palmitic acid (16:0), (j) stearic acid (18:0), (k) oleic acid (18:1), (l) overlay showing liposomes (red), palmitic acid (green) and oleic acid (blue). Purple color in the overlays indicate colocalization of red and blue in the image, and cyan color represents colocalization of green and blue. (scale bar: 50 μm) Adapted from Carlred, et al.[70] Copyright 2014 American Chemical Society

cells.[73] This setup flows cells into the device where they attach in individual wells. The matrix is injected into the device, encasing the cells for MALDI. In a different approach, Phelps et al. utilized microextraction to remove individual organelles from adipocytes differentiated from 3T3 L1 murine fibroblasts and placed them on a glass coverslide before being put into the MALDI.[74] This eliminated the need for extraction from multiple cells for each sample, reduced purification, and eliminated digestion compared to previous organelle extraction protocols.

1.4.2 Mass Cytometry

The last MS technique discussed is mass cytometry, which is often used when studying cancer and the immune system.[75, 76] Mass cytometry was developed to overcome the spectral overlap limitations found in flow cytometry. Unlike the previous label-free imaging techniques, mass cytometry uses antibodies attached to nonradioactive rare earth metal isotopes that bind to a protein of interest. After the cells are tagged with up to 45 different antibodies, the cells are individually introduced into the inductively coupled plasma by nebulization. Only the heavy ions are allowed to pass through the quadrupole before seperating by TOF. Finally, the number and identity of the rare earth metal are recorded for each individual cell.[76]

Recent pushes in mass cytometry research have focused on implementing the instrument into clinical settings for patient diagnosis. The severity of surgical trauma is often related to immune response, and Gaudilliere et al. demonstrated the use of mass cytometry to correlate immune signatures with recovery time, pain, and functional impairment. Using serial whole-blood samples, three signaling responses in CD14$^+$ monocyte subsets correlated with surgical trauma. In addition, this paper demonstrated the ability to use mass cytometry to survey immune cells in a clinical setting. [77] Mass cytometry also has been exploited to identify bacteria based on their cell surface and ability to bind lectins. Leipold et al. incubated *E. coli* with lanthanide-tagged nonspecific membrane stains and were able to distinguish three different strains of *E. coli* in one sample using lectins labeled with lanthanide metals.[78] The use of mass cytometry in clinical applications is still a new and budding field, with ongoing work to clarify old methodologies and develop new methodologies. To illustrate methodological issues, Gaudilliere et al. set up a study looking at immune signatures of women with a history of term birth vs. preterm birth and gave a list of considerations needed when considering doing experiments in a clinical setting. [77]

A major limitation of mass cytometry is that most methods require the sample to be in suspension before injection, therefore losing all spatial resolution. A recent innovation by Giesen and colleagues created a technique to gain spatial resolution by utilizing immunohistochemical and immunocytochemical methods with high-resolution laser ablation and mass cytometry to increase spatial resolution. In this method, the tissue of interest is extracted and fixed before staining with the metal-labeled antibodies. Using a UV laser, the sample is ablated and sent into the mass cytometer. The images are processed, giving single cell spatial resolution.[79]

1.5 Conclusion

Electrochemistry and mass spectrometry of single cells give us chemical insight into both cellular communication and cell structural components. Medically, these techniques can be used to understand how disease affects cells, distinguish cells that may be damaged or diseased, characterize drug metabolism in cells, and distinguish among bacterial strains. There are still major limitations to single cell analysis. However, new progress in the various techniques have been made, including increasing specificity of electrodes, combining techniques together such as amperometry and patch clamp or SIMS and SEM to give more in-depth information, and creating new sample preparation and ionization methods. Together all of these techniques will bring us closer to understanding how cells works together and by themselves to impact disease and cellular function.

Chapter 2: Variations in Fusion Pore Formation in Cholesterol-Treated Platelets

Reprinted in part from: Solaire A. Finkenstaedt-Quinn[ǂ], Sarah M. Gruba[ǂ], and Christy L. Haynes. Variations in Fusion Pore Formation in Cholesterol-Treated Platelets. *Biophys. J.*, 110(4), 922-929. Copyright 2016, with permission from Elsevier
[ǂ]Authors contributed equally

This manuscript was also included in Solaire Finkenstaedt-Quinn's Thesis

2.1 Overview

Exocytosis is a highly regulated intercellular communication process involving various membrane proteins, lipids, and cytoskeleton restructuring. These components help control granule fusion with the cell membrane, creating a pore through which granular contents are secreted into the extracellular environment. Platelets are an ideal model system for studying exocytosis due to their lack of a nucleus, resulting in decreased membrane regulation in response to cellular changes. In addition, platelets contain fewer granules than most other exocytosing cells, allowing straightforward measurement of individual granule secretion with carbon-fiber microelectrode amperometry. This technique monitors the concentration of serotonin, an electroactive molecule found in the δ-granules of platelets, secreted as a function of time, with 50 μs time resolution, revealing biophysical characteristics of the fundamental exocytotic process. Variations in fusion pore formation and closure cause deviations from the classic current versus time spike profile and may influence diffusion of serotonin molecules from the site of granule fusion. Physiologically, the delivery of smaller packets of chemical messengers or the prolonged delivery of chemical messengers may represent how cells/organisms tune biological response. The goals of this work are two-fold: (1) to categorize secretion features that deviate from the traditional mode of secretion and (2) to examine how changing the cholesterol composition of the platelet membrane results in changes in the pore formation process. Results herein indicate that the expected traditional mode of secretion is actually in the minority of granule content secretion events. In addition, results indicate that as the cholesterol content of the plasma membrane is increased, pore opening is less continuous.

2.2 Introduction

To maintain proper physiological function, cell-cell communication occurs through the highly regulated exocytotic process wherein granules dock on the cell membrane, utilizing SNARE proteins to assist in regulating attachment. These proteins are localized to cholesterol-rich microdomains throughout the cell membrane.[1] The amount of cholesterol in these domains not only plays a role in the proper clustering of SNARE proteins, but also helps stabilize the negative curvature needed for formation and stabilization of the fusion pore between the docked and primed granule and the cell membrane. Cholesterol levels and membrane viscosity are directly correlated, and increasing viscosity is known to result in delayed movement of lipids between the leaflets, which has been hypothesized to increase fusion pore formation and closing times.[2,3] Chemical messenger molecules can be secreted through this dynamic fusion pore structure into the extracellular space. Literature precedent has shown that cholesterol has a role in controlling exocytosis, but the extent to which it dictates the opening and closing of the fusion pore structure requires more exploration, ideally with a method that can quantitatively assess this dynamic structure.[2,3]

In recent years, it has become clear that the process of granule fusion is more intricate than originally thought. Traditionally, exocytosis was considered to be an all-or-nothing process, but in the last decade the definition has changed to include kiss-and-run events where a granule temporarily fuses with the cell membrane before detaching. More recently, it has become apparent that most granule secretion events are in fact extended kiss-and-run events which do not result in full chemical messenger content secretion.[4-7] Schematic portrayals of these various exocytosis events can be seen in Fig. 2.1A-C. Further countering the traditional view of exocytosis, individual granules have also been observed combining with one another, either before or during secretion, resulting in a process termed compound exocytosis.[8,9] However, in platelets, our chosen exocytosis model due to its lack of nucleus and therefore decreased ability to up- or down-regulate proteins, granules can also fuse to the open canalicular system (OCS). The OCS is a tubular system located throughout the platelet, which is hypothesized to assist in the secretion of granular content into the extracellular environment.[10] At the OCS-cytosol interface, it is possible for two granules to attach near one another and release their contents into the OCS, where the contents can combine and secrete simultaneously into the extracellular environment. This phenomenon could lead to chemical messenger secretion measurements characteristic of compound exocytosis. Unfortunately, current measurement technology does not allow us to distinguish between these two forms. Therefore we will describe all events with large amounts of serotonin secretion, typically larger than the average amount secreted in two separate granules (>960 fC) and a 10/90 slope of 6 or greater as bulk fusion (Fig. 2.1D).

Even with this limitation, carbon-fiber microelectrode amperometry (CFMA) is an ideal technique for studying the dynamic variations in granule secretion events. In platelets, the only electroactive compound at 700 mV vs. Ag/AgCl is serotonin, which has been confirmed by cyclic voltametry.[11,12] Statistical analysis has demonstrated that, due to the size of the cell relative to the electrode and the distance between the electrode and platelet, nearly 100% of all serotonin is detected.[11] Electrical fouling is also checked by monitoring the I_{RMS} and replacing the electrode if I_{RMS} increases or the signal goes down. Therefore monitoring the oxidation of serotonin, found in the δ-granules, gives us a means to study changes in the pore dynamics when microelectrodes are placed in immediate contact with individual platelets. As each granule fusion pore opens, an increase in current is detected as secreted serotonin is oxidized, resulting in a

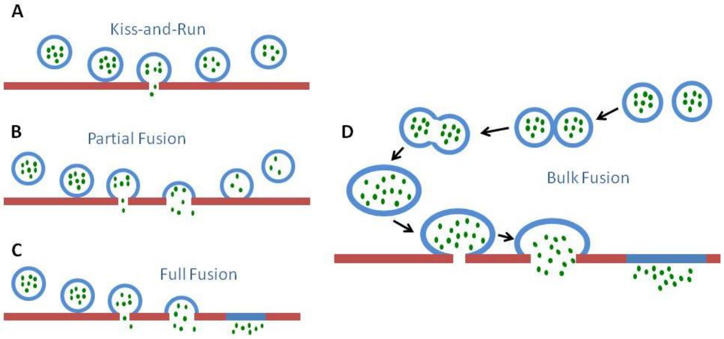

Figure 2.1 Various proposed modes of exocytosis, from least to most chemical messenger release. A) Kiss-and-Run: In kiss-and-run events, the granule fuses briefly with the plasma membrane, releasing only a small portion of its contents without significant dilation of the fusion pore. B) Partial Fusion: In partial fusion events the granule initially fuses with the plasma membrane, releases some of its contents, and then closes and returns to the platelet cytoplasm. C) Full Fusion: In full fusion events, the granule fully fuses with the plasma membrane and releases all of its contents. D) Bulk Fusion: In bulk fusion, multiple granules are hypothesized to fuse with one another prior to fusing with the plasma membrane, this is commonly referred to as compound fusion. However, platelet granules can adhere to the OCS and release their contents into the extracellular environment together; which is indistinguishable from compound fusion using CFMA. Therefore, we termed all of these events as bulk fusion.

current spike. In some cases, an individual current spike will be flanked either before or after the current maximum by a smaller current feature known as a “foot” event; these foot events correspond to the relatively small number of serotonin molecules secreted when a fusion pore is not fully dilated. Due to the small number of granules in platelets and length of time between granule secretion events, it is possible to distinguish the start and end of each granule event, including feet events, without overlap from other granule secretion events. This event resolution allows analysis of the variations in each spike profile, revealing mechanistic biophysical information about pore fusion behavior for each granular secretion event. Since cells do not typically secrete their entire content and there is a limited quantity of δ-granules, it is possible that several of the recorded spikes in each cell amperometric trace are from the same granule.

This work examines the modes of pore formation and closure and how membrane cholesterol levels impact these modes. Results indicate that as the cholesterol membrane content increases there is a corresponding increase in the number of secretion events with distinguishing characteristics. In particular, an increase in the number of non-traditional events (NTEs) was observed. It was also noted that at greater levels of cholesterol the NTEs have a slower fusion pore opening, increased secretion of serotonin molecules during each secretion event, and a longer duration in which the fusion pore remained open.

2.3 Experimental Approach

2.2.1 Materials and Methods

Amperometric traces from individual rabbit platelets were recorded previously by Shencheng Ge using CFMA.[2] Briefly, platelet cholesterol levels were manipulated by exposing platelets either to methyl-β-cyclodextrin (MβCD) (Sigma-Aldrich St. Louis, MO) to achieve cholesterol depletion or MβCD complexed with cholesterol (Sigma-Aldrich St. Louis, MO) to achieve cholesterol enrichment. Platelets with varying levels of cholesterol were stimulated using 10 μM ionomycin and 2 mM Ca^{2+} in Tyrode's buffer. The secreted serotonin was oxidized by an in-house fabricated carbon-fiber microelectrode at 700 mV vs. a Ag/AgCl reference electrode held by an Axopatch 200B potentiostat (Molecular Devices Sunnyvale, CA), and the resulting current was measured as a function of time. Each collected current vs. time trace was filtered at 5 KHz by a four-pole Bessel filter ahead of further analysis.

Each amperometric trace (N= 75, 72, and 50 for MβCD, control, and cholesterol-loaded platelets, respectively) was then digitally filtered at 1000 Hz and analyzed using Mini Analysis software (Snyptosoft Inc. Fort Lee, NJ) for pre- and post-spike feet. The spikes were analyzed visually by using a gain of 15 and a block of 20 unless the current spike was too large for the frame, in which case the gain was decreased so that the entire spike was visible within the frame. After examining each trace, the various features were divided into categories based on the general shape of the secretion event, (Fig. 2.2A) resulting in pre- and post-feet (Fig. 2.3, Fig. 2.4). Each spike was analyzed manually using the “group analysis and curve fitting” option to determine the duration and area of both the foot alone and the spike and foot features combined. In addition to foot features, there are also current spikes that do not display the typical quick current rise due to serotonin secretion followed by a gradual current decay as serotonin diffuses away which were titled NTEs (Fig. 2.5). The NTEs were subdivided into six different categories

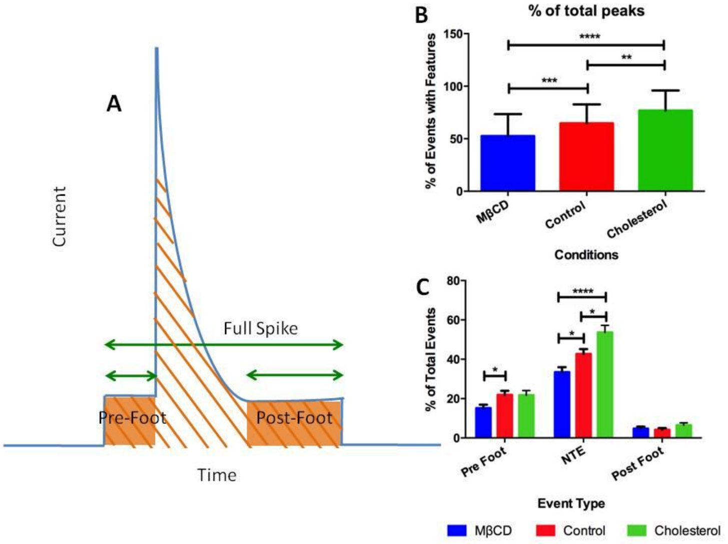

Figure 2.2 Schematic of spikes varriations and spike feature changes with cholesterol. A) Diagram indicating the parameters used to categorize and quantify various spikes. B) The frequency of events with features upon the different cholesterol treatments. C) Relative frequency of classes of spikes with the different cholesterol treatments. *p≤ 0.05, **p≤0.01, ***p≤0.001, ****p≤0.0001

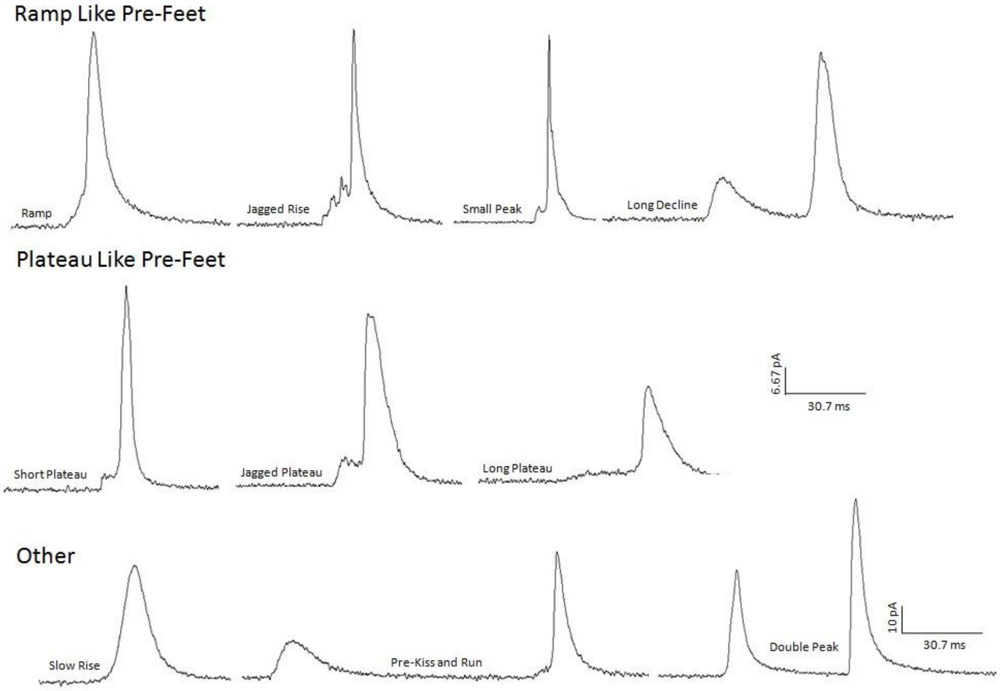

Figure 2.3 Representations of the various pre-spike feet types. The representative traces are all on the same current and time scale excluding the double spike.

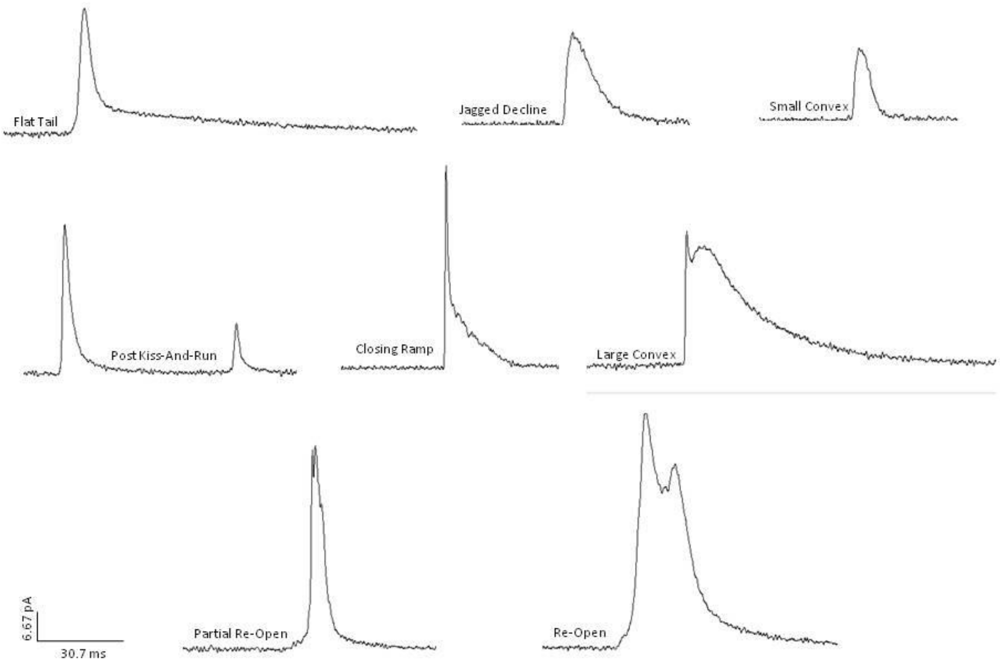

Figure 2.4 Representations of the various post-spike feet types. The representative traces are all on the same current and time scale.

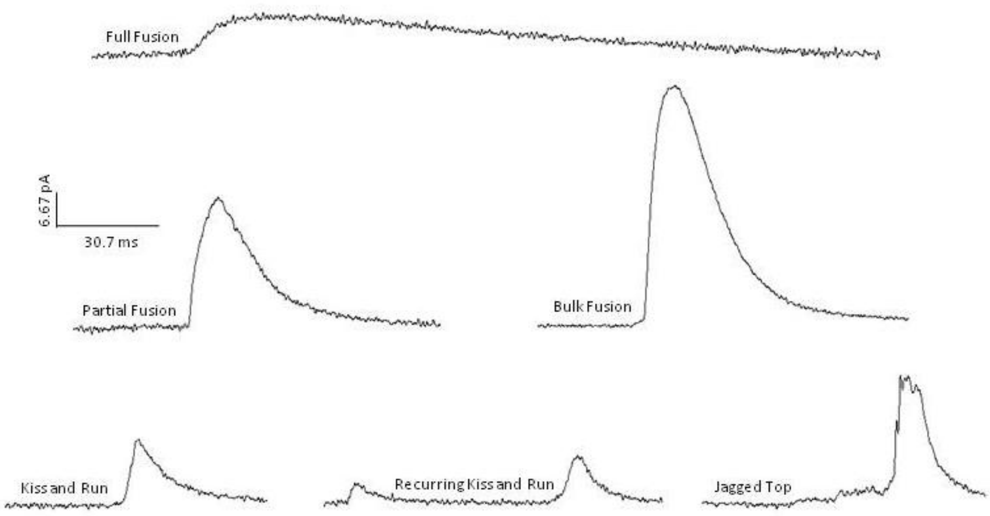

Figure 2.5 Representations of the various non-traditional events. The representative traces are all on the same current and time scale.

(full fusion, partial fusion, bulk fusion, kiss-and-run, recurring kiss-and-run, and jagged top) based on the area (charge, Q) under each spike, which is proportional, through Faraday's Law, to the amount of serotonin secreted, and how quickly the fusion pore opened relative to its maximum secretion (slope$_{10/90}$, the slope between 10% and 90% of maximal current intensity) (Table 2. 1). Jagged top features were distinguished by continuous up and down fluctuations of serotonin secretion at maximum opening, and recurring kiss-and-run displayed several kiss-and-run events within a second of each other.

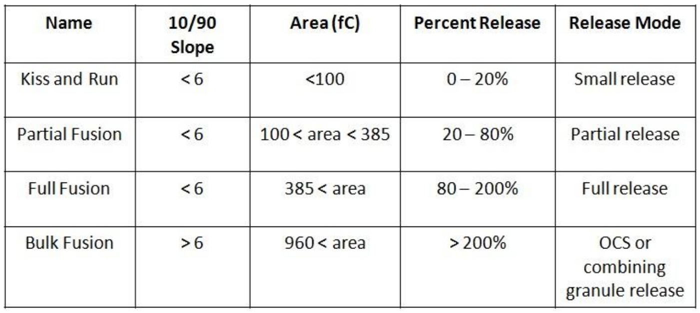

Name	10/90 Slope	Area (fC)	Percent Release	Release Mode
Kiss and Run	< 6	<100	0 – 20%	Small release
Partial Fusion	< 6	100 < area < 385	20 – 80%	Partial release
Full Fusion	< 6	385 < area	80 – 200%	Full release
Bulk Fusion	> 6	960 < area	> 200%	OCS or combining granule release

Table 2.1 Non-Traditional Events Characterizations. NTEs were characterized by their 10/90 slope and area. As NTEs are often characterized by slower pore opening, the 10/90 slope was determined to be a good indicator of NTEs. To distinguish between the different types of NTEs, the extent of release, or area under the current spike, was used. Commonly, events releasing twice the amount of serotonin or greater than the predicted concentration, had steep 10/90 slopes that were most likely due to more serotonin occupying the larger free space outside the dense-body core. Therefore, bulk fusion events had a 10/90 slope >6. All slopes and areas were calculated using the Mini Analysis software.

The cut-off criteria categorizing events with a 10/90 slope under 6 pA/ms was chosen empirically based on the manual analysis of many spikes that represented traditional and non-traditional secretion events. Non-traditional secretion events were further categorized based upon the amount of serotonin secreted. To set an upper limit on the secretion that could be attributed to kiss-and-run, we averaged the spikes in the control platelets considered to be kiss-and-run and found the highest value within one standard deviation of the mean, then made this our maximum secretion value. Previous data obtained by HPLC indicated that a five minute ionomycin stimulation on rabbit platelets resulted in the average secretion of 52% of the total serotonin content.[13] The average area (250 fC per granule in control platelets) was thus assumed to be 52%

content secretion. Full fusion was set as a minimum of 80% content secretion, or 385 fC/event. Secretion events where granule fusion resulted in at least 200% content release, or greater than 970 fC, and contained a 10/90 slope of 6 pA/ms or greater were categorized as bulk fusion events. For NTEs, the event area and event duration of the entire spike was analyzed manually using the “group analysis and curve fitting” option in mini analysis.

The percent frequency of each feature (pre-foot, post-foot, or NTE) was determined by dividing the total number of events with that feature by the total number of secretion events in each trace (Fig. 2.2). Within each feature type, the percent frequency was accounted for with respect to the total number of events with that feature (for example, within each trace, a pre-foot type was compared to the total number of granule secretion events with pre-foot features) (Table 2.2, 2.3, 2.4). Significance was determined between conditions by one-way ANOVA with all error given as the standard error of the mean.

Ramp Like Pre-Feet

	RAMP	Jagged Rise	Small Spike	Long Decline
MβCD	35.7 ± 5.3 %	7.0 ± 3.1 %	6.8 ± 2.8 %	8.7 ± 3.2 %
Control	34.6 ± 4.7 %	11.4 ± 3.2 %	7.0 ± 2.2 %	9.0 ± 2.3 %
Cholesterol	23.0 ± 4.3 %	16.4 ± 4.9 %	7.5 ± 2.4 %	3.9 ± 2.1 %

Plateau Like Pre-Feet

	Short Plateau	Jagged Plateau	Long Plateau
MβCD	11.5 ± 3.5 %	5.1 ± 2.3 %	0.9 ± 0.9 %
Control	10.6 ± 2.7 %	3.7 ± 1.9 %	4.6 ± 1.7 %
Cholesterol	14.0 ± 4.5 %	10.1 ± 3.2 %	10.4 ± 3.2 %

Other

	Slow Rise	Pre K&R	Double Spike
MβCD	12.2 ± 3.5 %	3.2 ± 1.9 %	8.7 ± 3.2 %
Control	8.1 ± 2.4 %	0.3 ± 0.3 %	10.8 ± 3.2 %
Cholesterol	9.1 ± 3.3 %	0.3 ± 0.3 %	5.1 ± 1.9 %

Table 2.2 Percent frequency of each pre-spike foot feature with SEM: Only long plateau was significantly ($p \leq 0.01$) different between MβCD to cholesterol.

	Flat Tail	Jagged Decline	Small Convex	Post Kiss and Run	Closing Ramp	Large Convex	Partial Re-Open	Re-Open
MβCD	6.7 ± 4.3 %	17.3 ± 7.3 %	3.8 ± 3.8 %	21.2 ± 7.9 %	0.0 ± 0.0 %	0.0 ± 0.0 %	27.9 ± 8.6 %	23.1 ± 8.0 %
Control	9.0 ± 4.3 %	18.5 ± 7.6 %	15.4 ± 6.3 %	29.0 ± 8.1 %	0.0 ± 0.0 %	8.6 ± 5.2 %	8.3 ± 4.8 %	11.1 ± 6.2 %
Cholesterol	2.1 ± 1.5 %	26.7 ± 8.4 %	6.6 ± 2.9 %	5.9 ± 4.3 %	4.5 ± 2.6 %	0.0 ± 0.0 %	46.5 ± 9.4 %	7.6 ± 4.5 %

Table 2.3 Percent frequency of each post-spike foot feature with SEM. Only partial re-open was significantly ($p \leq 0.01$) different between MβCD to cholesterol.

	Full Fusion	Partial Fusion	Bulk Fusion	Kiss-And-Run	Recurring Kiss & Run	Jagged Top
MβCD	6.4 ± 1.6 %	36.5 ± 3.9 %	17.8 ± 3.6 %	33.2 ± 4.1 %	2.1 ± 0.8 %	4.0 ± 1.7 %
Control	12.0 ± 2.2 %	35.5 ± 3.4 %	21.0 ± 3.9 %	22.9 ± 3.1 %	2.6 ± 0.8 %	6.0 ± 1.9 %
Cholesterol	11.8 ± 2.5 %	32.6 ± 4.3 %	18.1 ± 3.5 %	27.3 ± 4.6 %	4.3 ± 1.3 %	5.9 ± 1.7 %

Table 2.4 Percent frequency of each NTE with SEM.

2.4 Results and Discussion

2.4.1 Overall Trends

Based upon previously established methods of secretion, exocytosis events have been categorized herein into four types 1) kiss-and-run, 2) partial fusion for both normal pore opening rates (10/90 slope > 6 pA/ms) and extended pore opening rates (10/90 slope < 6 pA/ms) (when discussing partial fusion for the remainder of the paper, we are referring to the extended pore opening rates and not the traditional spike formation), 3) full fusion, and 4) bulk fusion (including both granule-granule fusion and bulk OCS fusion). The different models are illustrated schematically in Fig. 2.1.[4-9]

After platelets were enriched in cholesterol or depleted of cholesterol by platelet exposure to MβCD (132% and 68%, respectively, compared to control platelet cholesterol levels),[2] the total percentage of events with either a foot or NTE secretion profile increased with increasing concentrations of cholesterol (52.6 ± 2.4%, 64.7 ± 2.2%, and 76.8 ± 2.8% for depleted, normal, and cholesterol-enriched platelets, respectively, Fig. 2.2B). Normal levels of foot events reported with CFMA are traditionally around 10-30%,[2,13,14] which is nominally lower than what we have reported; this discrepancy is likely due to our inclusion of non-traditional type events and post-foot containing events when determining the percentage of events with features-of-interest. When only events with pre-foot characteristics are taken into account, the percentage of events falls to previously described ranges with 15.2 ± 1.8%, 21.9 ± 2.0% and 21.8 ± 2.3% for increasing cholesterol concentrations, respectively (Fig. 2.2C). Post-foot events, which have been known to only occur ~2% of the time in PC-12 cells,[6] occur relatively infrequently (4.8 ± 1.0%, 4.2 ± 0.8%, and 6.5 ± 1.2% for increasing cholesterol concentrations) in platelets and do not change significantly as the cholesterol content is changed. Changes in platelet membrane cholesterol have the largest impact on secretion via NTEs, with statistically significant ($p \leq 0.05$ for comparisons to control platelets and $p \leq 0.0001$ from MβCD to cholesterol) increases from 33.5 ± 2.5% for cholesterol-depleted platelets to 53.6 ± 3.6% of the events for cholesterol-enriched platelets, with a value of 42.7 ± 2.5% in control platelets. This suggests that cholesterol has a large impact on the whole fusion event rather than just the initial opening or closing of the pore. This difference is not attributable to a change in the number of granules undergoing exocytosis as the membrane cholesterol levels change. By counting the number of spikes in each trace, on average, each platelet secreted 12.7 ± 0.7, 12.6 ± 0.9, and 13.1 ± 0.9 granules per cholesterol-depleted, control, and cholesterol-enriched platelet, respectively.

2.4.2 Pre-Spike Feet Events

The occurrence of pre-spike foot events only changes significantly as seen in a decrease for cholesterol-depleted platelets ($p \leq 0.05$). When the pre-foot events are broken down into sub-types, the majority of the pre-feet were present in two forms: those where the initial secretion took some sort of ramp (an initial slow opening) or those where the initial secretion took the form of a plateau (an initial opening which is held steady over an extended period of time) (Fig. 2.3).

These two general characteristics have been reported before in several papers.[6,14,15] The most commonly reported and most discussed pre-spike foot type is the ramp. Amatore and colleagues reported that in chromaffin cells, of their pre-spike feet events, 70% were ramps, 20% were ramps with plateaus, and 10% were unclassified. They then found a positive correlation between the ramps' maximum current and the maximum current given by the spike.[14] Our data (Fig. 2.6A) show that the ramp-type pre-spike foot was the most frequently occurring of the pre-spike foot types, at 35.7 ± 5.3%, 34.6 ± 4.7%, and 23.0 ± 3.8% for cholesterol depleted-, control-, and cholesterol-enriched platelets, respectively. For the depleted and control conditions, the percent occurrence of the ramp was significantly enhanced ($p \leq 0.0001$) compared to the other pre-spike foot types. The ramp frequency in cholesterol-enriched platelets was only significantly different from four out of the nine other pre-spike feet types (p ranging from 0.05 to 0.0001). This, along with previous work in other groups, leads us to believe that this ramp characteristic is representative of the traditional entryway for granular fusion. The ramp-like variants, such as jagged rise, could potentially correspond to the opening and closing of the fusion pore during formation, suggesting that the cell is not able to easily transition to the type of curvature needed in the membrane as the fusion pore opens. This inability to rapidly change the membrane curvature paired with increased membrane stiffness is also implicated in the significant increase in the occurrence of long plateau foot events between the cholesterol-depleted and enriched conditions ($p \leq 0.01$)(Fig. 2.6B). In addition, the increase in the duration of the short plateau foot

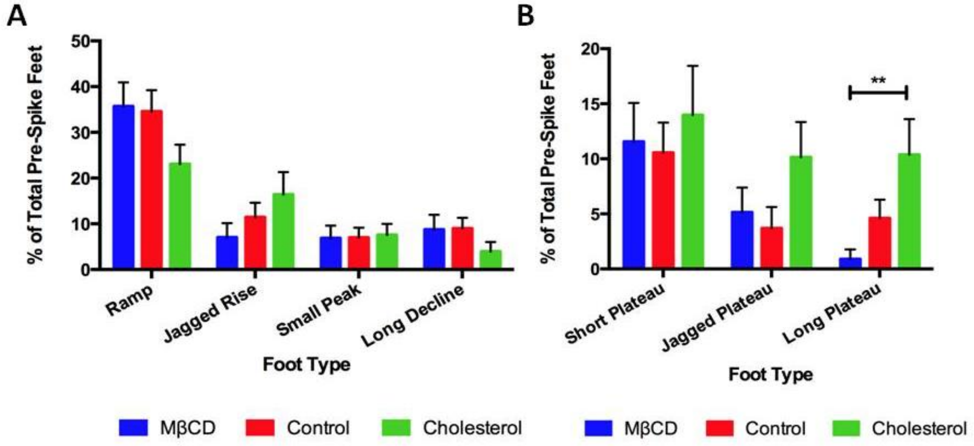

Figure 2.6 Pre-spike % relative frequencies for feet with ramp-like characteristics (A) and plateau-like characteristics (B) with the different cholesterol treatments. **P≤0.01 for indicated conditions

relative to the whole event as cholesterol content increases suggests that increasing membrane rigidity results in a barrier to the pore opening to the proper form (Fig. 2.7).

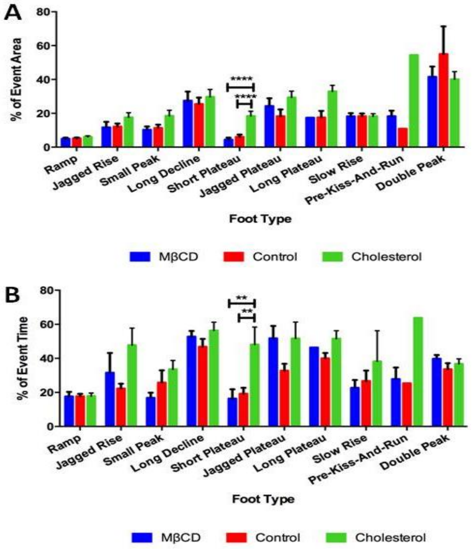

Figure 2.7 Percent of event area (A) and percent of time the foot feature occurred relative to the time of the whole event (B) for pre-spike feet. **p≤0.01, ****p≤0.0001

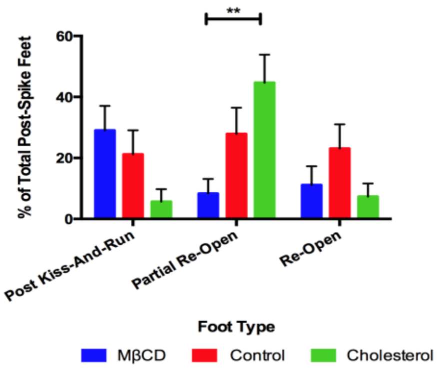

Figure 2.8 Relative frequency for post-spike foot types with varying cholesterol treatments. **p≤0.01

2.4.3 Post-Spike Feet Events

As the post-spike feet were not prevalent, it was difficult to identify variation in their forms. In total, eight different types of post-spike feet were identified, three of which were categorized as different forms of re-opening (Fig. 2.4 and Fig. 2.8). Of the re-opening type post-spike feet, the partial re-opening type foot showed a significant difference in frequency between the cholesterol-depleted and cholesterol-enriched conditions, with the foot occurring 8.3 ± 4.8% and 46.5 ± 9.4% of the time, respectively. Since the significant increase is only seen in the partial re-open post foot event, where the pore begins to reopen directly after beginning to close, it indicates that the pore initially has difficulty closing, but after closure has been initiated, the cholesterol levels do not impact the process to the extent they do for pre-foot events.

2.4.4 Non-Traditional Events

The most interesting results arising from categorization of the spikes observed upon platelet activation was the prevalence of spikes that were not in the form of traditional secretion events, meaning that they lacked the typical fast rising current due to pore opening followed by a slow current decrease as serotonin diffuses out of the closing pore. These secretion events were sorted into six categories by examining a combination of the following characteristics: 10/90 slope, the lack of a foot character, and the area (Fig. 2.5 and Fig. 2.9). Table 2.1 gives the 10/90 slope and area characteristics for four out of the six types of NTEs observed. While the NTEs as a category showed significant increases in percent frequency of total events as the cholesterol increases (Fig. 2.2C), when the NTEs are broken down into the various exhibited types, no significant changes are observed where one specific category is affected by the amount of cholesterol (Fig. 2.9). However, there are significant changes in the area and duration for the various features as the membrane-cholesterol levels are changed (Fig. 2.10). Most surprisingly, these changes in duration and area are seen in events that have set upper and lower limits for the amount of serotonin secreted, including partial fusion and kiss-and-run events. When comparing the average amount of serotonin secreted per ms during kiss-and-run events, there is no significant difference between cholesterol conditions (Fig. 2.11 A). This suggests that the cholesterol helps the pore stay open longer, but does not change the size of the pore, assuming that the serotonin diffusion characteristics are unchanged. Therefore, with the small standard deviation associated with each event type's duration and amount of serotonin secreted and the fact that there is no difference in the rate of serotonin secretion between conditions, this suggests that all granules going through kiss-and-run will follow a similar pattern of secretion. In comparison, for partial fusion, there were no significant differences in rate of secretion, but a downward trend was noted as membrane cholesterol content increased (Fig. 2.11 B). This suggests that once the pore opens past the kiss-and-run stage, it may not open as wide at higher cholesterol levels. However, due to the longer length of time it stays open, more serotonin is secreted which serves to make up for this decreased rate of secretion. Finally, there is an apparent upward trend in percent occurrence for full fusion events and a corresponding apparent downward trend for partial fusion events as the conditions contribute to higher membrane cholesterol levels (Fig. 2.9). These trends can all be explained by the increased membrane rigidity due to the additional cholesterol. As previously hypothesized, an

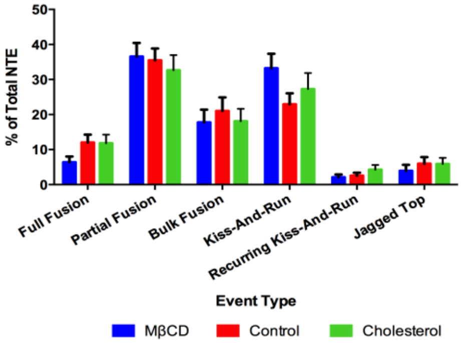

Figure 2.9 Relative frequency of each type of NTE with various cholesterol treatments.

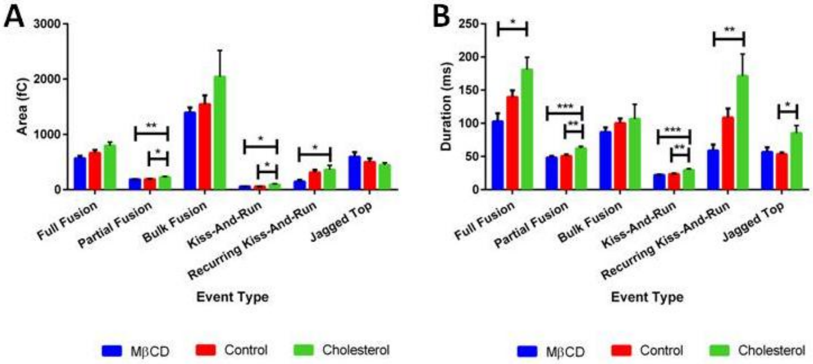

Figure 2.10 Area and duration of non-traditional events. A) Average area of each NTE type under the different cholesterol treatments. B) Average duration of each NTE type under the different cholesterol treatments. *p≤ 0.05, **p≤0.01, ***p≤0.001

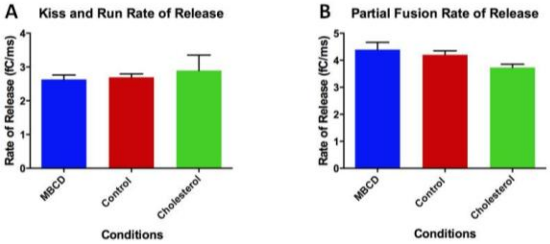

Figure 2.11 Rate of release for kiss and run events (A) and partial fusion events (B).

increase in cholesterol would lead to longer inversion times for the phospholipids needing to change the curvature along the fusion pore, biasing towards full secretion events.

2.5 Conclusion

Close examination of the pre-foot and post-foot spike features from individual platelets with manipulated outer membrane cholesterol levels indicated a few styles of pore opening and closing. Pre-foot features tended to fall into two sub-categories: ramp-like and plateau-like, with the ramp occurring most frequently. There was a slight decrease in the occurrence of pre-foot features in cholesterol-depleted platelets, indicating that the pore opens more quickly at low cholesterol levels, bypassing the slower foot-inducing features. The post-foot features occurred fairly infrequently and had primarily re-opening characteristics. The most prevalent category of non-traditional secretion events showed an increase in frequency as the cholesterol content of the membrane increased. These events are characterized by an increase in the amount of serotonin secreted, increased duration of the pore opening, and a slowing in the opening of the pore. From these analyses, we conclude that as the cholesterol concentration in platelets is increased, the membrane-granule fusion curvature transitions are slowed due to increased rigidity, leading to a slower pore opening and closing.

Even though the fusion pore dynamics of human platelets have not been studied directly with CFMA, it has been shown that platelets from other species (Chapter 4), in particular cow which has comparatively increased levels of cholesterol, demonstrate similar fusion pore dynamics as the rabbit platelets incubated with cholesterol. These included increased T_{rise} and $T_{1/2}$ times compared to rabbit platelets without cholesterol modification which are often associated with NTEs.[2,13] In addition, since platelets are anucleate, the up- and down- regulation of proteins and receptors is limited, suggesting that the only difference between the conditions was the concentration of cholesterol. Therefore we believe these results, though they are measured in an animal system, can be generalized to human platelets and other cell types that undergo exocytosis.

Human platelets have been shown to undergo changes in cholesterol membrane content due to various diseases, drugs, or pre-dispositions.[16,17] In addition, platelets are known to increase cholesterol uptake in vitro when suspended in cholesterol-rich environments.[18] Previous literature indicates that cholesterol plays a role in human platelet sensitivity, microtubule ring formation, and aggregate size due to cholesterol levels.[18,19] Thus, it is likely that the results presented herein can inform understanding of human platelets and the diseases affecting them.

Chapter: 3 Stereochemistry- and Concentration-Dependent Effects of Phosphatidylserine Enrichment on Platelet Function

This work was completed with the assistance of Audrey F. Meyer, Donghyuk Kim, Ben M. Meyer, Secil Koseoglu, Joseph J. Dalluge, and Christy L. Haynes

This co-written draft was also included in Audrey F. Meyer's Thesis

3.1 Overview

Platelets use several forms of communication including exocytosis of three distinct granule populations, formation of bioactive lipid mediators, and shape change (allowing for adhesion). Typically known for their role in hemostasis, they can provide an excellent platform for studying the role of membrane components in cellular communication due to their ease of isolation, and anucleate nature, allowing limited up and downregulation of membrane components. In this chapter, the role of stereochemistry and concentration of phosphatidylserine (PS) on cell exocytosis will be studied. PS, most commonly found in the phosphatidyl-L-serine (L-PS) form, is exposed on the outer leaflet of the cell membrane, after the cell is activated, to communicate apoptosis to clearance cells. Knowledge about their impact is limited on other cell communication (particularly concentration and stereochemistry effects). This study found that platelets incubated in L-PS or phosphatidyl-D-serine (D-PS) are enriched to the same extent with their respective incubated PS. All levels of L-PS enrichment had an increase in platelet cholesterol, but only the 50 μM D-PS incubation had an increase in cholesterol. The uptake of D-PS induced the secretion of granules and manufactured platelet activating factor (PAF) in otherwise unstimulated platelets. The uptake of L-PS had a greater impact on platelet stimulation by decreasing both the amount of δ-granule secretion and the amount of platelet activating factor (PAF) that is manufactured.

3.2 Introduction

Platelets are small (1-2 µm in diameter), circulating anuclear cell fragments that promote hemostasis by mediating the processes of clotting and angiogenesis. Although most widely known for their involvement in blood clot formation, they also play roles in inflammation and cancer malignancy. All of these actions are mediated by platelet secretion and adhesion, both of which are influenced by the platelet membrane composition.[1] In addition to the importance of platelets in various physiological processes, the anuclear nature of platelets makes them an interesting platform for studying the role of membrane phospholipids in cell secretion and adhesion functions.

Phosphatidylserine (PS) is a particularly important component of cellular membranes due to its critical role in the cell signaling cascades, in particular, those that lead to clearance of apoptotic cells. In most cells, phospholipids with an L-serine headgroup (L-PS) compose 2-10% of the total phospholipid content, and until recently, it was thought that all naturally occurring PS phospholipids were L-PS.[2] Recently, however, PS containing a D-serine headgroup (D-PS) have been detected at quantities of 0.05 – 0.9% of the total PS content in rat tissues including cerebrum, heart, spleen, lung, testis, liver, and kidney,[2] and it is not clear if the biological roles of L-PS and D-PS are identical. When cells are unactivated, L-PS is localized to the inner leaflet of the membrane while the localization of D-PS is unknown. Upon activation, aminotranslocase, which maintains L-PS in the inner leaflet, is down-regulated, inducing activation of lipid scramblase. This activation, in conjunction with the rapid influx of Ca^{2+}, disrupts the phospholipid asymmetry, resulting in the exposure of L-PS to the outer leaflet of the membrane.[3-5] The reorientation of L-PS to the outer leaflet of the platelet is important as L-PS exposure to the extracellular environment signals apoptosis to surrounding phagocytes.[6-12] Several studies have also shown that the stereochemistry of the PS headgroup influences both the binding of cell signaling proteins and the clearance of apoptotic cells by phagocytes including macrophages, which only recognize L-PS.[13]

These findings indicate that L-PS plays a larger role than D-PS on the stimulation of platelets decreasing the amount of serotonin secreted from δ-granules and the manufacturing of the lipid mediator PAF. D-PS, however, induces stimulation of the alpha, δ, and lysosome granules as well as the secretion of PAF in unactivated platelets. Finally, incubation with L-PS led to a greater increase in platelet cholesterol than incubation with D-PS.

3.3 Experimental Approach

3.3.1 Reagents

Unless otherwise specified, all analytical grade reagents were purchased from Sigma-Aldrich. The α-D-(+)-glucose was purchased from Acros Organics (Fair Lawn, NJ), PAF and PAF-d4 standards were purchased from Cayman Chemical (Ann Arbor, MI), and the L-α-phosphatidylserine (product #840032C) and 1,2-dioleoyl-sn-Glycero-3-Phospho-D-serine (product #79098) were purchased from Avanti Polar Lipids (Alabaster, AL). For UPLC-MS/MS, LC/MS-grade H_2O and acetonitrile (ACN) were purchased from J.T. Baker (Center Valley, PA). LC/MS-grade isopropyl alcohol (IPA), Na_2CO_3, and citric acid were purchased from Fisher Scientific

3.3.2 Platelet Isolation

Male C57BL/6J mice were purchased at 9 weeks old from The Jackson Laboratory, euthanized via CO_2 asphyxiation (according to IACUC-approved protocol #0806A37663), and blood was drawn via cardiac puncture using syringes pre-filled with 200 μL ACD. For all experiments, platelets were isolated by centrifuging whole blood for 10 min at 130 RCF with no brake, transferring the plasma layer to fresh tubes, diluting the plasma layers 6:1 with ACD, and pelleting the platelets at 524 RCF.

3.3.3 Phospholipid Incubation

Following isolation, platelets were incubated for 2 hrs with 10, 50, or 100 μM L-PS (Fig. 3.1A) or D-PS (Fig. 3.1B) prepared in Tyrode's buffer. To avoid solubility inconsistencies, 200 μM solutions of L-PS or D-PS stock solutions were prepared as described previously[15] and diluted as needed for incubations with different L-PS or D-PS concentrations. Briefly, solutions were prepared by evaporating the chloroform from appropriate volumes of the phospholipid solutions with a gentle stream of nitrogen, stirring overnight in Tyrode's buffer, then filtering with 0.2 μm filters.

All assessments of L-PS and D-PS enrichment, cholesterol content, and platelet secretory function were normalized to pelleted platelet protein content, which was quantified using a Pierce bicinchoninic acid (BCA) assay kit from Thermo Scientific (Rockford, IL). Where possible, measured values of secreted mediators were normalized to the pelleted protein content of individual replicates; when this was not possible, pelleted protein values represent the average of four biological replicates.

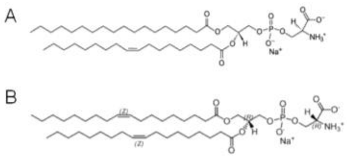

Figure 3.1 Structure of L-PS (A) and D-PS (B). Structures provided by Avanti Polar Lipids

3.3.4 UPLC-MS/MS Assessment of Relative L-PS and D-PS Enrichment

Enrichment of L-PS and D-PS in platelet membranes was assessed using a Waters Acquity UPLC system in tandem with a Waters triple quadrupole mass spectrometer using a previously reported method[15] modified to include transitions for D-PS. Details of the UPLC method can be found in Koseoglu, et al. Briefly, aqueous mobile phase A was 20 mM ammonium acetate at pH 5, organic mobile phase B was 90/10 ACN/IPA with 0.1% acetic acid, and a Waters BEH C8 2.1 x 100 mm column at 60°C was used. Multiple reaction monitoring was used for mass spectrometric detection of the phospholipids: transitions monitored for L-PS, and D-PS can be found in Table 3.1. PAF-d_4, with a transition from $524.4 > 184.1$, was used as an internal standard. L-PS and D-PS were isolated from PRP after platelets incubated with the phospholipids were washed three times via centrifugation at 1000 RCF and resuspended in 4:1 Tyrode's buffer:ACD. After the final centrifugation step, platelets suspended in 100 µL Tyrode's buffer were sonicated with 400 µL chloroform and 200 µL methanol for 20 min, then sonicated for 10 more min following the addition of 100 µL 0.1% acetic acid in 0.1 M NaCl. Samples were centrifuged for 5 min at 1500 RCF, the upper aqueous layers were discarded, and the lower organic layers were dried under vacuum. Samples were resuspended by sonication in 40/60 A/B and analyzed by UPLC-MS/MS. Using a calibration curve prepared exactly as the platelet samples, relative L-PS and D-PS concentrations were acquired for each sample. To account for differences in platelet pelleting that could arise from increased phosphatidylserine content, L-PS and D-PS values were normalized to pelleted protein content for each platelet incubation condition. Statistical differences between experimental conditions were assessed using one-way ANOVA.

3.3.5 Cholesterol Content of Platelets Enriched With L-PS and D-PS

The cholesterol content of platelets was assessed using an Amplex® Red cholesterol assay kit from Life Technologies (Grand Island, NY) as directed. Statistical differences between experimental conditions were assessed using one-way ANOVA

3.3.6 Ensemble Measurements of Platelet Granule Secretary Function

After incubation with either L-PS or D-PS, platelets were washed and incubated with either PBS buffer (control) or PBS containing 1.25 U/mL thrombin (activated). After 5 min of incubation, ACD was added for a final volume of 1:4 ACD: PBS and centrifuged at 1,000 RCF for 10 min to pellet the platelets. Supernatants were collected and analyzed for the presence of granule-specific secreted species and de novo manufactured bioactive lipids. Secretion of δ-granules in a bulk suspension of platelets was assessed using an Agilent HPLC coupled to a Waters electrochemical detector as described previously.[15,16] Supernatants analyzed for serotonin were collected both after the wash step, to assess whether incubation with L-PS or D-PS induced platelet activation, and after stimulation with either PBS or thrombin, to assess the effects of L-PS and D-PS on δ-granule secretion. Dopamine served as an internal standard for serotonin detection. For all ensemble measurements, statistical differences between experimental conditions were assessed using one-way ANOVA.

Lysosome secretion from platelets was assessed using an absorbance assay for β-hexosaminidase (β-Hex), a lysosome-stored enzyme as described previously.[14,15,17] Absorbances from L-PS- and D-PS-treated platelets were normalized to the absorbance of control platelets. Secretion of α-granules was assessed using an enzyme-linked immunoassay kit for platelet factor 4 (PF4) purchased from R&D Systems (Minneapolis, MN) and used as directed.

Platelet secretion of PAF, a de novo manufactured bioactive lipid, was assessed using a modified version of a previously described UPLC-MS/MS method.[14,15] Although previous studies have focused on the detection of PAF-C16, this work focuses on the detection of PAF-C14. Due to the lack of available internal standards for PAF-C14, PAF-C16-d_4 was used as an internal standard.

3.3.7 Microfluidic Assessment of Platelet Adhesion Behavior

The microfluidic device used in this study is fabricated using standard soft lithography techniques, and the detailed procedure can be found in a previously published paper.[18] Briefly, a simple straight channel design was printed onto a transparent film (Cad/Art Service Inc.) and transferred onto a 5” x 5” blank chrome mask plate (Nanofilm). For the master copy, a silicon wafer was spin-coated with SU-8 photoresist (Microchem), and the device design was transferred onto the baked SU-8 silicon wafer with the previously completed mask. Once developed, a mixture of 10:1 PDMS monomer:curing agent (Ellsworth Adhesives, Germantown, WI) was cast onto the SU-8 master and cured overnight at 75 ℃. The cured PDMS layer is peeled, cut, and punched for the inlet and outlet holes, and then bound to a clean glass substrate via oxygen plasma treatment. Once completed, the device was brought into a biosafety hood and the channels were washed three times with 70 % ethanol solution in sterilized MilliQ water (Millipore) for device sterilization. Washed devices were dried and kept in the biosafety hood until use. The channel dimensions were 450μm (width) x 100μm (height) x 2500μm (length).

A human endothelial cell line (Hy926, ATCC) was used to establish a confluent layer of endothelial cells in the microfluidic channels. The endothelial cells were cultured in Dulbecco’s

Modified Eagle Medium (DMEM) with high glucose media (4mM L-glutamine, 4.5g/L L-glucose, and 1.5g/L sodium pyruvate (Gibco®)) supplemented with 10% fetal bovine serum and 1% penicillin and streptomycin (Sigma Aldrich). Conventional T-flask culture at 5% CO_2 and 37℃ was maintained with an every other day feeding schedule and a once a week splitting schedule. Herein, endothelial cells were only used between the fifth and eighth passages.

A 250 μg/mL human fibronectin solution was introduced into microfluidic channels for 30 minutes ahead of endothelial cells to facilitate endothelial cell adhesion onto the microfluidic channel surface. In parallel, endothelial cells in a T-flask were trypsinized, washed, and re-suspended into the same culture media at a cell density of $\sim 10^7$ cells/mL. After exchanging the media in the microfluidic channel with endothelial cell culture media, 20 μL of the cell suspension was injected through the channel, kept in an incubator for an hour, and washed with the endothelial cell culture media. Finally, 20 μL of the cell suspension was injected through the channel, incubated for another hour, and washed with the culture media again. The devices were kept in an incubator until use with a 12 hour feeding schedule. After 1-2 days, a confluent monolayer of endothelial cells was established; devices that did not establish uniform layers of endothelial cells were discarded after visual inspection.

After platelets had been incubated with L-PS, D-PS, or Tyrode's buffer, they were labeled with 5-chloromethylfluorescein diacetate (CMFDA) dye to facilitate their visualization (2 μM, 20 minutes). The labeled platelets were split into two populations - one of these populations was treated with 5μM ADP to activate them and the other was the same volume of Tyrode's buffer as an unactivated control. As ADP activation may cause significant platelet aggregation before introduction onto the microfluidic device, incubation was avoided and preparation of endothelial cell-coated microfluidic devices (washing channels with Tyrode's buffer) was done in parallel. Both platelet suspensions, activated by ADP or unactivated, were then introduced into the microfluidic channels at the flow rate of 30 μL/hour, where minimal shear-induced platelet and endothelial cell activation is expected, for 20 minutes. After exposure of platelet suspension to the endothelial cell layer, the microfluidic channels were washed with Tyrode's buffer and devices were brought to the microscope stage for fluorescence imaging (Nikon microscope with QuantEM Photometrics CCD camera) Metamorph Ver. 7.7.5 was used as the imaging and analysis software. Statistical differences between experimental conditions were assessed using student's t-test.

3.4 Results and Discussion

3.4.1 L-PS and D-PS Platelet Enrichment

Enrichment of L-PS and D-PS in platelet membranes was evaluated using UPLC-MS/MS following incubation of platelets with 10, 50, or 100 µM solutions of each phospholipid, and results of the enrichment are shown in Fig. 3.2 A and B and detailed in Table 3.1. Using UPLC-MS/MS to determine relative enrichment offers several advantages to the analytical challenge of phospholipid detection. Selective reaction monitoring (SRM) enables the detection of specific mass transitions, which were set to the primary components of each L-PS and D-PS standard rather than blanket detection all of the phosphatidylserine compounds in the membrane. A D-PS standard was selected that differed from the primary component of the L-PS standard by 2 mass units, or one unit of unsaturation, which enabled chromatographic separation of the two compounds, as shown in Fig. 3.2D. To evaluate platelet uptake of L-PS and D-PS, the concentration of L-PS in control platelets (not exposed to L-PS or D-PS) was normalized to 100%, and concentrations of L-PS and D-PS were calculated as the percent enrichment of the L-PS in control platelets. Comparing both phosphatidylserine species to the same levels of L-PS in control platelets enables a comparison of the abilities of the platelets to take up each of the phosphatidylserine species.

Platelets demonstrated significant uptake of both L-PS and D-PS at all incubation concentrations examined, and the uptake of D-PS and L-PS at each incubation concentration were not statistically different from one another ($p > 0.05$ using one-way ANOVA), i.e. incubation with 10 µM L-PS produced the same percent enrichment of total PS as the 10 µM D-PS. This indicates that platelets were enriched to a similar degree with either L-PS or D-PS, and if any differences are observed between the L-PS and D-PS at the same incubation concentration (10, 50, or 100 µM), are likely due to the stereochemistry of the head group.

3.4.2 Effects of L-PS and D-PS Enrichment on Platelet Cholesterol Content

Previous studies regarding the interaction between cholesterol and phosphatidylserine have generally been made using model membrane systems. The work of Wachtel and colleagues demonstrated that the solubility of cholesterol in membranes containing phosphatidylserine decreases as the molar ratio of phosphatidylserine increases. As such, it was hypothesized that increasing the phosphatidylserine content of the platelet membrane would expel cholesterol, thus decreasing the cholesterol content of the pelleted platelets and increasing the cholesterol content of the supernatants, as compared to control platelets. This change in membrane cholesterol level may also have significant impact on critical cell functions such as exocytotic delivery of chemical messengers.

Incubation Condition	L-PS	D-PS
Transition used for relative quantitation	812.5 > 208	810.5 > 208
Instrumental Precision (RSD)	6.97	7.74
Biological Precision (RSD)	13.7	15.7
Average Percent increase ± SD[a] upon 10 μM incubation for 2 hours	345 ± 106	279 ± 91
Average Percent increase ± SD[a] 50 μM incubation for 2 hours	575 ± 68	638 ± 98
Average Percent increase ± SD[a] 100 μM incubation for 2 hours	730 ± 76	749 ± 94

Table 3.1 Relative enrichment of L-PS and D-PS in platelet membranes. [a]Percent increase is reported as the percent increase over the nmol PS/μg pelleted protein, as the amount of D-PS present in control platelets was much lower than the D-PS detected in platelets incubated with D-PS. The enrichment of D-PS as a percentage of D-PS content of control platelets was 2350 ± 767 for platelets incubated with 10 μM D-PS, 5370 ± 822 for platelets incubated with 50 μM D-PS, and 6300 ± 625 for platelets incubated with 100 μM D-PS.

Cholesterol is integral to cell membrane function, and the interaction between cholesterol and phosphatidylserine, examined in a variety of model membranes and monolayers, is clearly important in regulating the structure, fluidity, and function of the cellular membrane.[19] To determine whether L-PS or D-PS enrichment induces the expulsion of cholesterol from the platelet membrane, the cholesterol content of the both the pelleted platelets and the supernatants following incubation with L-PS and D-PS were evaluated. Incubation with either D-PS or L-PS induced an increase in platelet cholesterol content (Fig. 3.2C), but the cholesterol levels in the supernatant were not significantly different from the cholesterol per protein content of the incubation supernatants of control platelets. As Fig. 3.2C shows, the increase in platelet cholesterol content is higher following enrichment with 50 µM L-PS than 10 µM L-PS ($p = 0.004$) and with 50 µM D-PS than with 10 µM D-PS ($p = 0.0001$). Additionally,

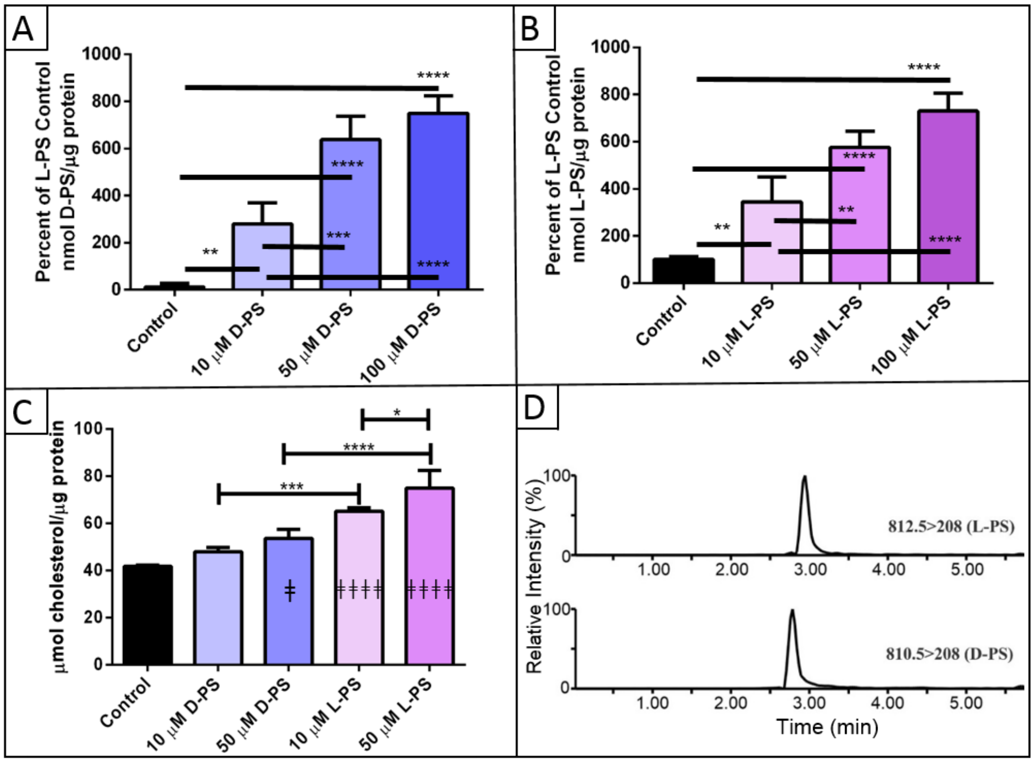

Figure 3.2 Determination of D-PS, L-PS, and cholesterol oncentration. Percent enrichment of A. D-PS and B. L-PS. The cholesterol content of platelets, C, after incubation with either D-PS or L-PS. D. Chromatograms of L-PS (top) and D-PS (bottom). $^{*}p \leq 0.05$, $^{**}p < 0.01$, $^{***}p < 0.001$, $^{****}p < 0.0001$ vs. indicated condition using one-way ANOVA. ǂ $p \leq 0.05$, ǂ ǂ ǂ ǂ $p < 0.0001$ vs. cholesterol control using one-way ANOVA. Error bars represent mean ± standard deviation.

the increase in cholesterol content following phospholipid incubation was higher with L-PS than with D-PS ($p = 0.0003$ for 10 µM incubations and $p < 0.0001$ for 50 µM incubations).

The results of this study have demonstrated the opposite of the expected effect, indicating that either complexity of the platelet membrane affects the solubility of cholesterol in phosphatidylserine-containing membranes or cholesterol is expelled from the membrane but remains membrane-associated. Additionally, platelets were enriched to the same degree with either L-PS or D-PS, but the different forms of phosphatidylserine resulted in different levels of cholesterol content. There are several possible explanations for this effect. Within a phospholipid membrane, it has been shown that cholesterol, like phospholipids, is asymmetrically distributed in the membrane. Previous studies of cholesterol in phospholipid membranes support the theory that cholesterol exists within the membrane in two forms, both dissolved and crystalline. As cholesterol has been shown to have decreased solubility in phosphatidylserine, due to the increased hydrogen bonding around the negatively charged headgroup, it is possible that enriching platelets with phosphatidylserine results in the conversion of dissolved cholesterol to crystalline cholesterol. Another possibility is that the rigidity of phosphatidylserine decreases the solubility of cholesterol, which results in the conversion of cholesterol to its crystalline form.[19] When this occurs, the platelet would experience a shift in the equilibrium concentration of cholesterol and increase cholesterol production to compensate for the potentially decreased membrane stability induced by additional phosphatidylserine. The formation of cholesterol to a lesser degree in platelets incubated with D-PS may be a result of the extra unit of unsaturation; when in the membrane, a completely saturated tail will be relatively straight, allowing for tighter packing and interaction with the other tails, leading to extra rigidity. The extra unit of unsaturation in D-PS may cause the tail to deform, decreasing the extent to which the lipid tails can interact and pack, and, thus, increasing membrane fluidity. As shown in the work done by Wachtel and coworkers, this greater fluidity causes the solubility of lipid cholesterol to be increased, resulting in less crystallite formation and a smaller equilibrium shift in unactivated platelet cholesterol content.

3.4.3 L-PS vs. D-PS Effects on Ensemble Secretion of Chemical Species

To evaluate the effect of phosphatidylserine enrichment on platelet secretion, several ensemble measurements were used, including measurement of both stored and newly manufactured chemical messenger species. These measurements include *de novo* synthesis of PAF-C14, serotonin secretion from δ-granules, β-Hex secretion from lysosomes, and PF4 secretion from α-granules.

Effects of exposure to exogenous L-PS and D-PS on the secretion of the manufactured lipid, PAF-C14, from platelets are shown in Fig. 3. 3. Exposure of control platelets to 1.25 U/mL thrombin for 30 min induced increased secretion of PAF-C14 ($p = 0.04$ vs. control unactivated platelets), while thrombin activation did not induce a significant increase in PAF-C14 secretion from platelets enriched with either D-PS or L-PS at 10 or 50 μM, when compared to their unactivated counterparts. For enrichment at 10 μM D-PS, this is almost certainly due to the significant increase in PAF-C14 secretion of unactivated platelets ($p = 0.003$ vs. control unactivated platelets). For platelets incubated with 50 μM D-PS and 10 μM L-PS, small but non-significant increases in the PAF-C14 secretion of unactivated platelets and small but non-significant decreases in the PAF-C14 secretion of thrombin-activated platelets likely contribute to the observation of no significant increases in PAF-C14 generation in response to thrombin. For platelets incubated with 50 μM L-PS, thrombin-activated secretion of PAF-C14 is completely attenuated ($p = 0.04$ vs. thrombin activated control platelets). This attenuation of PAF secretion is consistent with previous results for 100 μM L-PS incubation.

Serotonin, one species stored in δ-granules, was used as a marker of platelet δ-granule secretion. The effects of D-PS and L-PS enrichment on platelet δ-granule secretion are shown in Fig. 3.4. At all enrichment levels of D-PS and L-PS, thrombin increased δ-granule secretion compared to their unactivated counterpart ($p \leq 0.05$ for each thrombin-activated condition vs. unactivated platelets of the same enrichment condition). Unactivated platelets enriched with 10 or 50 μM D-PS or with 50 μM L-PS demonstrated increased δ-granule secretion vs. control unactivated platelets ($p < 0.05$). Meanwhile, thrombin-activated platelets enriched with 50 μM D-PS or 10 or 50 μM L-PS demonstrated decreased δ-granule secretion compared to thrombin activation of control platelets ($p \leq 0.05$). The suppression of thrombin-stimulated δ-granule secretion was more pronounced with L-PS than with D-PS and more pronounced at 50 μM enrichment than 10 μM enrichment for both phosphatidylserine species. This effect is in contrast to the effects of D-PS and L-PS on δ-granule secretion of unactivated platelets, where both 10 and 50 μM D-PS enrichment induced δ-granule secretion, but only 50 μM L-PS did. Furthermore, 50 μM D-PS enrichment induced a greater degree of δ-granule secretion from unactivated platelets than enrichment with 50 μM L-PS ($p = 0.04$). Lysosome secretion was assessed using an absorbance assay for β-Hex, one lysosome-secreted species, and the effects of L-PS and D-PS enrichment can be found in Fig. 3.5. When exposed to thrombin, control platelets and platelets enriched with 10 μM D-PS induced increased secretion of β-Hex. Unactivated platelets enriched with 50 μM D-PS increased lysosome secretion, but exposure to thrombin did not further increase the secretion of lysosomes from platelets.

The effects of L-PS and D-PS enrichment on thrombin-stimulated platelet secretion of α-granules are shown in Fig. 3.6. PF4 was not detected in unactivated platelet samples. In thrombin-activated platelets, enrichment with 50 μM D-PS induced a decrease in the secretion of α-granules ($p = 0.03$ vs. thrombin-activated control), but enrichment with L-PS or with 10 μM D-PS did not affect thrombin-stimulated platelet secretion of α-granules.

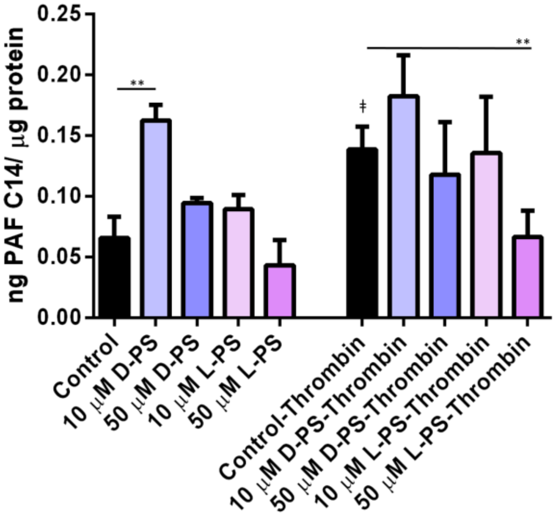

Figure 3.3 Secretion of PAF-C14 from platelets enriched with L-PS and D-PS. **p ≤ 0.01 using one-way ANOVA. ǂp≤ 0.05 vs. control platelets.

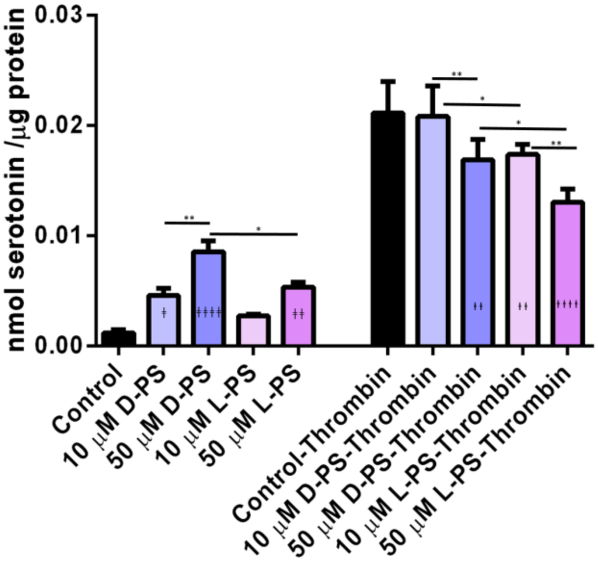

Figure 3.4 Effects of L-PS and D-PS enrichment on platelet δ-granule secretion. *p ≤ 0.05, **p < 0.01 vs. condition as indicated using one-way ANOVA. ǂp ≤ 0.05, ǂǂp< 0.01, ǂǂǂǂp< 0.0001 vs. Control (resting platelets) using one-way ANOVA. ƚƚp < 0.01, ƚƚƚƚp < 0.0001 vs. Control-Thrombin using one-way ANOVA.

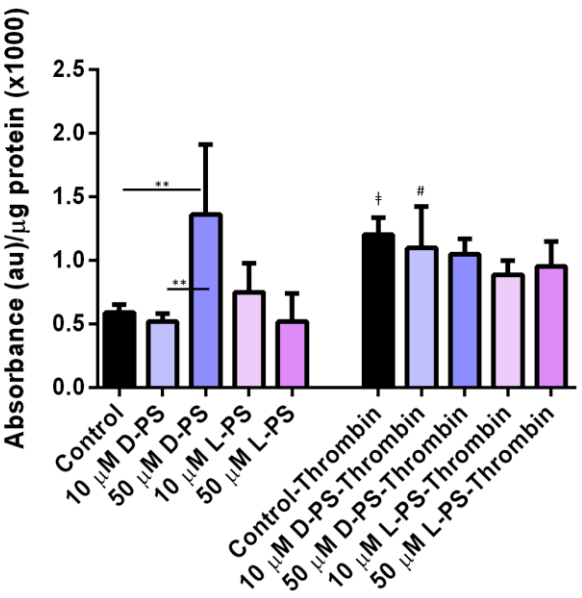

Figure 3.5 Lysosome secretion of platelets enriched with D-PS or L-PS. **p < 0.01 vs. condition indicated; ǂp = 0.02 vs. Control resting platelets; #p = 0.04 vs. 10 μM D-PS enriched resting platelets using one-way ANOVA.

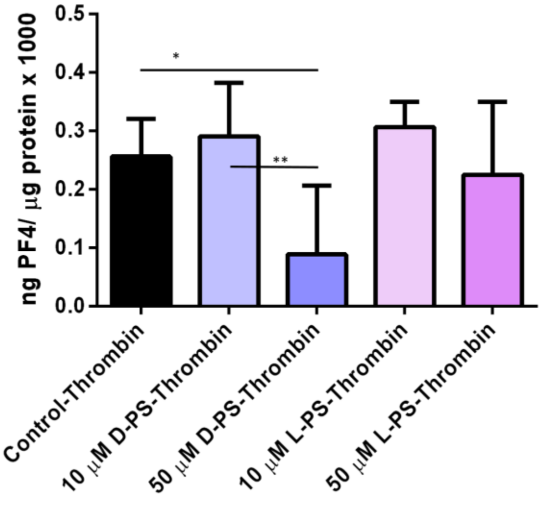

Figure 3.6 Thrombin-stimulated α-granule secretion of platelets enriched with D-PS or L-PS. *p = 0.03; **p = 0.002, using one-way ANOVA. PF4 was not detected in resting platelet samples.

In general, enriching platelets with L-PS or D-PS suppresses the thrombin-stimulated secretion functions of platelets, while inducing granule secretion by unactivated platelets. In particular, in unactivated platelets, incubation with 10 μM D-PS induces the secretion of PAF-C14 and δ-granules, and incubation with 50 μM D-PS induces the secretion of δ-granules and lysosomes. Incubation with 10 μM L-PS did not affect the secretory behavior of unactivated platelets, and incubation with 50 μM L-PS induced the secretion of δ-granules, albeit to a smaller extent than with 50 μM D-PS. These results indicate that the incorporation of D-PS into the platelet membrane activates the protein machinery responsible for exocytosis, while L-PS incorporation into the platelet membrane does not. L-PS enrichment, unlike D-PS enrichment, had a greater effect on thrombin- activated secretion of PAF-C14 and δ-granules secretion. While several studies have detected very small amounts of D-PS in brain and other tissues, clearly the effects of D-PS on platelets differ than from those of L-PS.

When considering the effects of L-PS or D-PS on platelet secretion function, it is important to also consider the increase in cholesterol with both L-PS and D-PS enrichment. The data in Fig. 3.2C indicate that the cholesterol remains associated with the platelets, although it is not known whether the membrane cholesterol is localized to the interior or exterior of the membrane.[19] One potential reason for the increased effect of L-PS on thrombin activation of platelets could be that excess cholesterol can impact the number of thrombin receptors and affinity[20]. Previous research by Tandon et al., correlated the responsiveness of platelets to thrombin with varying level of cholesterol while monitoring the change in thrombin affinity and receptor expression. Their research indicates that the cholesterol levels correlate positively with the number of receptors, but negatively with the affinity of the receptor towards thrombin. However, as the cholesterol level increased, platelet response (aggregation and secretion of serotonin) became more sensitive to lower concentrations of thrombin.[20] The concentration of thrombin (1.25 U/mL) used in this study is relatively high, compared to concentrations used to stimulate platelets naturally, therefore the response from platelets in each experimental condition should be similar at 1.25 U/mL. This suggests that the impact of cholesterol on thrombin receptors is not solely responsible for the decreased amount of secretion caused by thrombin stimulation of platelets incubated with L-PS. Another factor to keep in mind is cholesterol solubility in phosphatidylserine. The solubility depends on the saturation of the lipid tail as well as the charge of the headgroup, the differences between the effects of L-PS and D-PS on platelet secretory function could arise from the solubility of cholesterol in L-PS vs. D-PS.

3.4.4 Microfluidic Assessment of Adhesion

In addition to the secretion behavior, anotherr critical function of platelets exposed to L-PS or D-PS was explored – adhesion. The platelet adhesion ability, following incubation with L-PS or D-PS, was evaluated on a layer of endothelial cells using a microfluidic platform. Few studies are available regarding the relationship between membrane phospholipid content and platelet adhesion. However, in a recent study,[15] Koseoglu , et al. found that L-PS enrichment in platelet plasma membranes resulted in reduced adhesion of platelets to endothelial cells, and this work expands on the effects of PS on platelet adhesion through exploring the relative effects of L-PS and D-PS. Experimental conditions herein are unactivated and ADP-activated platelets, and each has five sub-conditions of control (no pre-exposure to either L-PS or D-PS), pre-incubated with L-PS (10 μM or 50 μM), and pre-incubated with D-PS (10 μM or 50 μM). Platelet adhesion to the confluent endothelial cell layer in the microfluidic device was assessed simply by counting the number of fluorescent platelets present following introduction and rinsing.

As shown in Fig. 3.7A, unactivated platelets showed decreased adhesion to the layer of endothelial cells when they were pre-incubated with either phosphatidylserine species. Interestingly, while L-PS did not show concentration dependence, unactivated platelets pre-incubated with D-PS showed concentration-dependent adhesion; in fact, unactivated platelets pre-incubated with 50 μM D-PS showed higher adhesion than any other phosphatidylserine-pre-incubated platelets. In contrast, ADP activation of platelets incubated with 50 μM L-PS or 50 μM D-PS demonstrated that D-PS has less impact on activated platelet adhesion behavior. This concurs with the ensemble measurements made of thrombin-stimulated platelet chemical messenger secretion. Again, all PS-enriched platelets showed lower adhesion to endothelial cells than control platelets. These impacts of L-PS and D-PS on platelet adhesion could result from changes in the membrane curvature due to the added phosphatidylserine content in the platelet membrane. However, the results herein also suggests the possibility that decreased adhesion is due to the increased PS membrane content reducing platelet secretion of chemical messengers. This possibility will be of significant interest for future study.

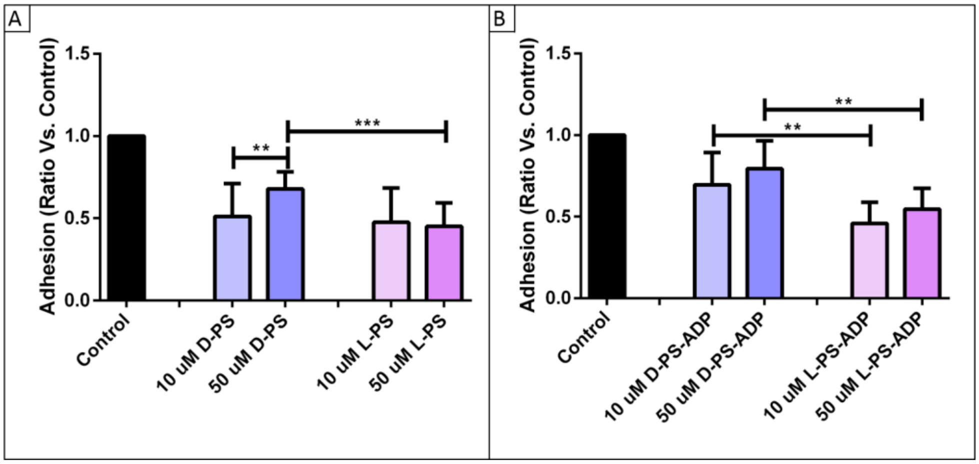

Figure 3.7 Microfluidic assessment of A. resting and B. ADP-activated platelet adhesion in platelets enriched with D-PS or L-PS. **$p < 0.01$; ***$p < 0.001$ using and unpaired t-test. In both A and B, all L-PS and D-PS enriched conditions are significantly different from the control platelet adhesion ($p < 0.0001$ using an unpaired t-test).

3.5 Conclusion

This work explored the effects of phosphatidylserine on platelet function by evaluating the effects of enriching platelets with either L-PS or D-PS. It was determined that incubation with either D-PS or L-PS results in the same degree of phosphatidylserine enrichment, and that the two stereochemical forms of phosphatidylserine have different effects on platelet secretory and adhesion function. Surprisingly, enrichment of both L-PS and D-PS increased the cholesterol content of the platelets, although the localization of the cholesterol in or around the platelet membrane is unknown. In general, platelet exposure to D-PS induces platelet activation in unactivated platelets while both L-PS and D-PS suppress thrombin-induced platelet secretory function, with a greater effect with L-PS than D-PS enrichment. Phosphatidylserine stereochemistry has implications in a broad range of biochemical processes including signaling apoptosis and binding of cell signaling proteins. This study demonstrates its effects on cellular function: while platelets take up L-PS and D-PS to the same degree, there are clear differences between the effects of L-PS and D-PS on secretion and adhesion behavior of both unactivated and activated platelets.

Chapter 4: Platelet Membrane Variations and Their Effects on δ-granule Secretion Kinetics and Aggregation Spreading Among Different Species

Reprinted in part from: Sarah M. Gruba[ǂ], Secil Koseoglu[ǂ], Audrey F. Meyer, Ben M. Meyer, Melissa A. Maurer-Jones, and Christy L. Haynes. Platelet Membrane Variations and Their Effects on δ-granule Secretion Kinetics and Aggregation Spreading Among Different Species. *BBA Biomembranes,* 1848, 1609-1618. Copyright 2015, with permission from Elsevier

[ǂ]Authors contributed equally

A version of this manuscript was also included in Secil Koseoglu's thesis

4.1 Overview

Platelet exocytosis is highly regulated in part by the granular/cellular membrane lipids and proteins. In addition some platelets contain a membrane-bound tube, called an open canalicular system (OCS), which assists in granular secretion events and increases the membrane surface area for greater spreading. In addition, variations in membrane composition can cause changes in platelet secretion. Since platelet studies use various animal models, it is important to understand how platelets differ in both their composition and granular secretion, in order to understand whether conclusions drawn from one model system can be combined with or will translate to another model system. Relative phospholipid composition of the platelets, with (mouse, rabbit) or without (cow) an OCS, was quantified using UPLC-MS/MS. Cholesterol and protein composition in the platelets was measured using Amplex Red and BCA Assays, respectively. TEM and dark field imaging were used to characterize platelet morphology. Finally, quantitative and dynamic granular secretion was monitored with single cell carbon-fiber microelectrode amperometry. The results show that cow platelets contain greater amounts of cholesterol and sphingomyelin then rabbit and mouse platelets. In addition, they yield greater serotonin secretion, longer δ-granule secretion times, and greater fusion pore stability. This increased stability could be due to extra sphingomyelin and cholesterol, the primary components of lipid rafts. Finally, they showed greater spreading area with a greater range of spread than OCS containing platelets. Platelets from different species that contain an OCS had similarities in their membrane composition and secretion kinetics, both distinct from cow platelets.

4.2 Introduction

Platelets are a crucial component in maintaining hemostasis through the secretion of three distinct secretory granule populations: α-granules, δ-granules, and lysosomes. Due to the unique anucleate nature of platelets, the exocytosis of these granules is regulated primarily by proteins, cholesterol, and phospholipids in both the overall platelet and granule membranes. Variations in the chemical composition of the membrane or granules have been linked to disorders including Wiskott-Aldrich syndrome, Scott syndrome, and giant platelet syndrome.[1-3] As researchers have delved into these differences, a variety of platelets from different species have been used to study both the fundamental molecular mechanisms of platelet function as well as the role of platelets in the aforementioned diseases. Platelets isolated from different species often share common features; however, there are both structural and functional differences that must be explored to fully understand whether conclusions drawn from one model system can be combined with or will translate to another.[4,5]

Comparison of the structural differences among platelets from different species will help illuminate the roles of these cellular structures. Additionally, comparative studies of platelet function across species can yield information on various ways in which platelets from different species adjust to the presence or absence of a particular feature. One such cellular structure of interest is the open canalicular system (OCS), a tubular membrane-bound system whose role in platelet function is not fully understood. The OCS is rare in nucleated cells, and in platelets it is only found in select species including humans, mice, and rabbits while platelets from cows, camels, and horses lack an OCS. This structure has been shown to help localize granules within the cell for easier export of their contents and is involved in the activation-initiated change in platelet morphology widely known as spreading.[6-9]

Due to the uniqueness of the OCS, several studies have examined species-dependent variations in OCS-related protein and receptor expression in platelets.[6,10] However, there is still limited information on how non-OCS platelets maintain hemostasis comparable to platelets with an OCS, thus making it harder to pinpoint the function of the OCS. This study focuses on how the membrane of the platelets with (mouse and rabbit) and without (cow) an OCS changes to enable normal platelet function, including measurement of phospholipid and cholesterol content while accounting for platelet sizes before and after activation. Insight into the spreading size and cholesterol content is important in this context because it will help test the hypotheses that (1) granules are involved in the spreading of platelets without a readily available OCS and (2) changes in membrane phospholipid content facilitates secretion of granule contents.

To follow platelet secretion dynamics, this work uses carbon-fiber microelectrode amperometry (CFMA) to elucidate the δ-granule involvement and changes in granule secretion. Traditional studies of platelet secretion have used ensemble cell assays, which measure secretion from thousands to millions of platelets at a time. While useful, ensemble measurements of cellular function obscure subtleties that can be observed on a single cell level using CFMA with sub-ms time resolution. This enables detailed evaluation of the kinetics of the secretory process and allows distinction within a heterogeneous set of platelets. For these studies two stimulants, ionomycin (a calcium ionophore) and thrombin (a natural platelet stimulant in the body) were chosen to determine OCS-dependent differences in activation. Stimulation with ionomycin bypasses several relevant physiological steps in platelet activation that are present following thrombin stimulation. Therefore, exploring differences between the two stimulants may reveal differences in secretion induced by changes in activation mechanisms rather than how the platelet interacts with the membrane or OCS during exocytosis.

Ultimately, using complementary analytical techniques including CFMA, biological assays, imaging, and mass spectrometry, we were able to determine the importance of platelet cell structure, including the OCS and lipid concentration, on cell activation secretion kinetics and spreading.

4.3 Experimental Approach

4.3.1 Platelet Isolation

Blood was collected according to protocols approved by the University of Minnesota IACUC (protocol numbers 0211712011 and 1105A99774). A mid-ear artery was used for rabbit blood draw to ethylenediamine tetraacetic acid (EDTA)-containing tubes. Mouse blood was collected via cardiac puncture following CO_2 asphyxiation into syringes pre-filled with ACD. Cow blood was drawn from the tail into EDTA-coated tubes. In all cases, blood was diluted by addition of Tyrode's buffer (NaCl, 137 mM; KCl, 2.6 mM; $MgCl_2$, 1.0 mM; D-glucose, 5.6 mM; N-2-hydroxyethylpiperazine- N'-2-ethanesulfonic acid (HEPES) 5.0 mM; and $NaHCO_3$, 12.1 mM with pH adjusted to 7.3) and centrifuged for 10 min at 500xg for rabbit and cow or 130xg for mouse platelets. The PRP (platelet rich plasma) layer was separated, and washed platelets were obtained following a second 10 min centrifugation step (750xg for rabbit and cow, 500xg for mouse platelets). Pelleted platelets were resuspended in Tyrode's buffer to a final concentration of 1 x 10^7 platelets/mL.

3.3.2 CFMA Measurements

Carbon-fiber microelectrodes were fabricated as previously described.[11-14] Amperometry experiments were performed with an Axopatch 200B potentiostat (Molecular Devices, Inc., Sunnyvale, CA) using low-pass Bessel filtering (5 kHz), a sampling rate 20 kHz, and gain amplification of 20 mV/pA, all controlled by locally written LabVIEW software and National Instruments data acquisition boards. Platelets were visually monitored during experiments with an inverted microscope equipped with phase contrast optics (40X magnification) (Nikon Instruments, Melville, NY). A drop of platelet suspension was added to the poly-L-lysine-coated glass coverslips containing Tyrode's buffer. As the platelets sedimented onto the coverslip, a carbon-fiber microelectrode was placed on an individual platelet for measurement (Fig. 4.1A). A

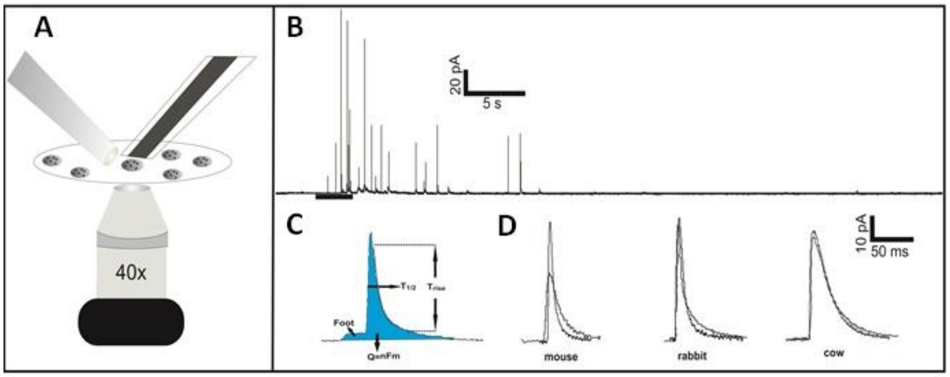

Figure 4.1 CFMA experimental setup and representative spikes. (A) Representative setup for CFMA measurements. The CFM (on the right) is placed on a single platelet. The stimulation pipette (on the left) is placed close to the platelet. (B) Typical amperometric trace obtained from single platelet secretion. Each spike corresponds to a single δ-granule release event. The bar under the trace shows time and the duration of the stimulation. (C) The parameters that are analyzed for single secretion events. (D) Representative spikes from mouse, rabbit and cow platelet exocytosis upon ionomycin (black) and thrombin (gray) stimulations

stimulant-filled fire-polished capillary with an average tapered diameter of 10 µm was also placed close to the platelet of interest. Upon delivery of a 3 s bolus of either 10 U/mL thrombin solution in Tyrode's buffer or 10 µM ionomycin in Tyrode's buffer supplemented with 2 mM Ca^{2+}, the platelet under the microelectrode was activated. Serotonin secreted from platelet δ-granules was oxidized at the carbon-fiber microelectrode at a potential of 700 mV vs. Ag/AgCl reference electrode, and data were recorded for 90s. Each amperometric trace obtained from single platelet secretion was filtered at 500 Hz, and spike by spike analysis was performed using Mini Analysis software. The sub-millisecond temporal resolution of the CFMA technique enables real-time analysis of serotonin secretion from individual platelet granules, each appearing as an individual current spike in the amperometric trace (Fig. 4.1C). The amount of serotonin secreted from a single granule is determined based on the area under the spike (Q= mFn; where Q is the charge, m is number of moles of serotonin, F is Faraday's constant, and n is the number of electrons (2) transferred during serotonin oxidation). The kinetics of secretion are revealed based on the T_{rise} and $T_{1/2}$ values for each current spike, indicating the kinetics of transition from fusion pore to full fusion and kinetics of the total secretion event, respectively. Finally, the percentages of spikes with feet (a small amount of secretion before the spike) were counted as well. The percentage of spikes with foot features indicates the stability of the fusion pore opening. The number of platelets that were monitored per condition was 23 and 32 for mouse, 35 and 34 for rabbit, and 39 and 22 for cow for ionomycin and thrombin stimulation, respectively.

4.3.3 Bulk HPLC Analysis

A similar bulk cell HPLC procedure was used as previously described.[15] Briefly, platelets in the PRP were diluted to $5x10^7$ cells/mL in Tyrode's buffer. 125 µL of the diluted PRP was plated into a Millipore 96 well Multi Screen HTS filter plate with a 0.45 µm pore and mixed with 125 µL of either Tyrode's buffer or Tyrode's buffer containing stimulant to reach a final concentration of 10 µM ionomycin with 2 mM Ca^{2+} or 10 U/mL thrombin. After a five minute stimulation, the supernatant was spun down at 3000xg for five minutes, and 180 µL of the supernatant was pipetted into a vial with 20 µL of 5 µM dopamine internal standard in 0.5 M perchloric acid. HPLC analysis was performed on an Agilent 1200 HPLC with an auto sampler containing a 5µm, 4.6 x 150mm C18 column (Eclipse XDB-C18) attached to a Waters 2465 electrochemical detector with a glassy carbon-based electrode. The working potential was set at 700 mV vs. an in situ Ag/AgCl reference electrode with a current range up to 50 nA. The samples were separated on the HPLC column at a flow rate of 2 mL/min in an aqueous mobile phase mixture consisting of 11.6 mg/L of the surfactant sodium octyl sulfate, 170µL/L dibutylamine, 55.8 mg/L Na_2EDTA, 10% methanol, 203 mg/L anhydrous sodium acetate, 0.1 M citric acid, and 120 mg/L sodium chloride. The ratio of serotonin to dopamine internal standard concentrations were then measured against a 5 point calibration curve made in advance using standard solutions of serotonin diluted in 0.5 M perchloric acid (ranging from 28 to 1000 nM serotonin). The standard solutions were supplemented with 0.5 µM dopamine internal standard.

4.3.4 TEM Measurements

TEM samples of cow and mouse platelets were prepared by two step fixation of the platelets first with 0.1% gluteraldehyde (15 min) followed by centrifugation to pellet and then with 3% gluteraldehyde (30 min) in White's saline as has been previously described.[16] After fixation, the cell pellet was exposed to 1% osmic acid at 4ºC for 1h. The platelet pellets were dehydrated slowly in a graded series of alcohol and embedded in Epon resin. Thin sections were obtained with a diamond knife. Uranyl acetate was used for contrast enhancement. TEM images captured on a JEOL 1200EX at an accelerating voltage of 60 keV were analyzed using ImageJ software.

4.3.5 CytoViva Scope Measurements

Darkfield scattering images were captured using an Olympus microscope from CytoViva (Auburn, Al) with an UplanFLM 100 x oil immersion objective and Dage XL camera. To prepare the slides, 4 μL of PRP were placed in the center of a cover slide. Gently, a coverslip was placed on top and sealed with clear nail polish. The un-activated platelets were imaged within 5-10 min of being placed on the cover slip. The activated platelets were given 1.5 hours to activate on the coverslip before being imaged. The perimeter of the platelets was analyzed using ImageJ software.

4.3.6 Platelet Cholesterol and BCA Assay

Platelet concentration was calculated with a hemocytometer to ensure similar platelet counts between species. 250 μL aliquots were put into a 1.7 mL microcentrifuge tube and spun down at 1000 xg to pellet the platelets; the supernatant was removed, and the pellets were then used to measure cholesterol and total protein content.

Cholesterol levels were determined with an Amplex Red Assay from Life Technologies (Carlsbad, Ca) as directed. Briefly, the pellet was mechanically homogenized to expose the cholesterol to cholesterol oxidase. Hydrogen peroxide was produced in situ and exposed to Amplex Red to form resorufin. The resorufin absorbance at 571 nm was detected using a BioTek Synergy 2 96 well plate reader, and a calibration curve was used to convert absorption intensity into concentration.

The protein content was quantified using a Pierce BCA Protein Assay kit from Thermo Scientific (Rockford IL) as directed. Briefly, a working reagent was prepared by mixing 50 parts of BCA Reagent A and 1 part BCA Reagent B. The PRP pellet was resuspended into 25 μL of mammalian protein extraction reagent, and 200 μL of working reagent was added to solution. After 30 min of incubation, the absorbance was measured at 562 nm on a BioTek Synergy 2 96 well plate reader and converted to a concentration using a calibration curve.

4.3.7 Plasma Cholesterol Assay

750 µL of whole blood from each species and 500 µL of Tyrodes buffer was alliquoted into 1.7 mL ependorf tubes. The blood was centrifuged down at 200 xg for 10 min with minimal

braking. The plasma layer was removed and re-centrifuged at 1200 xg to remove remaining cells. 200 μL of plasma and 50 μL of the 1x reaction buffer included in the Amplex Red Assay kit (described above) were alliquoted into ependorf tubes. 50 μL was then placed into a 96 well plate for a total of 5 replicates per specie. Finally, 50 μL of working solution was added to each well and the reaction was left to proceed for 30 min, at which time fluorescence was measured.

4.3.8 Aggregation Assay

Aggregation experiments were performed on a Chrono-Log Whole Blood Lumi aggregometer interfaced with Aggro/Link software. The platelets were concentrated at 4×10^7 platelets mL^{-1}. 500 μL of platelet suspension was alliqoted into glass vials with a magnetic stir bar and placed in the aggregometer with a Tyrodes buffer blank. Once the recorded absorbance was stable at 100%, 20 μL of thrombin was added for a final concentration of 9.7 units mL^{-1} Thrombin. The aggregation was monitored until the absorbance levels stabilized. Three biological replicates were performed. The data was plotted and statistically analyzed in Graph Pad Prism.

4.3.9 Relative Quantitation of Selected Phospholipids using UPLC-MS/MS

The relative concentrations of selected platelet phospholipids were determined through a previously published ultra-performance liquid chromatography-tandem mass spectrometric (UPLC-MS/MS) method. Briefly, platelet concentrations were determined using a hemocytometer, and samples were diluted to ensure approximately the same platelet concentration for each species. PRP was aliquoted into glass tubes, and a modified Bligh & Dyer extraction was performed to obtain phospholipids. PRP samples were suspended in Tyrode's buffer and mixed with 400 μL chloroform/200 μL methanol. As an internal standard, 10 μL of 19.1 μM deuterated platelet activating factor (PAF)-d_4 (Cayman Chemical, Ann Arbor, MI) was added to the extraction mixtures, and PRP samples were sonicated for 20 min. Following sonication, 100 μL of 0.1% acetic acid in 0.1 M NaCl was added to the samples, and they were sonicated again for 10 min and centrifuged for 5 min at 1500 xg for separation of the organic and water layer. The organic layer was retained and dried under vacuum. Finally, the sample was resuspended in 40/60 A/B with 0.1% acetic acid mobile phase where A was 20 mM ammonium acetate (pH 5) and B is 90/10 acetonitrile/acetone.

For UPLC-MS/MS relative quantitation of the selected phospholipid species, a calibration curve was prepared from solutions composed of phosphatidyl-L-serine (PS), sphingomyelin (SM), phosphatidylethanolamine (PE), and phosphatidylcholine (PC) from Avanti Polar Lipids

(Alabaster Al) and PAF-d_4 internal standard. Calibration solutions were prepared without platelets and subjected to the same extraction procedure as PRP.[17] The samples and calibration curve were run on a Waters Acquity UPLC-MS/MS system in tandem with a Waters triple quadrupole mass spectrometer as previously described.[17] A modified version of chromatography suggested by Rainville and Plumb was used with a Waters BEH C8 2.1x100 mm column, and chromatography conditions as well as electrospray ionization mass spectrometry parameters can be found in Koseoglu, 2014.[17,18]

4.4 Results and Discussion

4.4.1 Comparison of Lipid and Protein Content

Phospholipid	Rabbit (%)	Mouse (%)	Cow (%)	Instrumental Precision (RSD)
Percent of PC compared to mouse PC (RSD)	14.2 ± 7.1 **	100.0 ± 12.3	344.6 ± 13.3 ***	8.6
Percent of PS compared to mouse PS (RSD)	101.3 ± 27.8	100.0 ± 4.7	181.8 ± 8.1 ****	20.5
Percent of PE compared to mouse PE (RSD)	84.2 ± 24.7	100.0 ± 20.7	104.2 ± 17.8	12.3
Percent of SM compared to mouse SM (RSD)	109.1 ± 7.7	100.0 ± 11.6	1065.6 ± 15.6 ****	4.1

Table 4.1 Relative concentration of phospholipids compared to mouse.[+]

[+] Platelet concentrations for each of the three species were counted with a hemocytomer and diluted to the same concentration to ensure a similar number of platelets in each sample. All the data collected was then normalized to the mouse data. ** $p<0.01$ vs. the respective mouse phospholipid, **** $p<0.0001$ vs. the respective mouse phospholipid using one way ANOVA. Rabbit is also significantly ($p<0.0001$) different from cow for PC, PS, and SM. There is no difference between the three species for PE.

Phospholipids, the primary component in cell membranes and granules, are important for maintenance of both the structure and function of cells. Upon exocytosis, lipids assist in localizing and activating the proteins needed to fuse granules and help change the rigidity of the fusion pore.[19] Even without proteins, manufactured lipid cells have been shown to mimic regular fusion.[20] In addition, significant variation in kinetics and secretion among different cell types with varying phospholipid concentrations suggest that the phospholipids facilitate and enhance fusion and exocytosis.[19,20] Due to their impact on exocytosis, the concentration of the four most common cell phospholipids, PC, PS, PE, and SM, were quantified then compared to the percent of each specific phospholipid in mouse platelets in Table 4.1. All phospholipid data are compared to mouse platelets, both because mice are the typical model organism and because the phospholipid standards contained a mixture of a primary phospholipid component as well as the presence of other tail lengths. In addition, the instrumental precision was calculated for each phospholipid. Comparison across the different species show a significant increase in phospholipid concentration for cows compared to an approximately equal number of mouse platelets for PS, PC, and SM. In particular, the PC and SM concentrations, two phospholipids known to be mainly located in the outer leaflet of the platelet membrane, have increased concentrations, approximately 3 to 10 fold more than mouse. By contrast, PS and PE, primarily inner leaflet phospholipids in unactivated platelets, show much smaller differences. The differences between mouse and rabbit (both which contain OCS) can only be seen in the concentration of PC, which is significantly smaller for rabbit.

Cholesterol is another ubiquitous lipid species in cell membranes, with critical importance in membrane fluidity and curvature. Cholesterol regulates the spatial distribution of not only membrane phospholipids but the SNARE proteins involved in secretory events.[14,20,21] Platelets incubated in or depleted of cholesterol have shown significant variations in secretion kinetics,

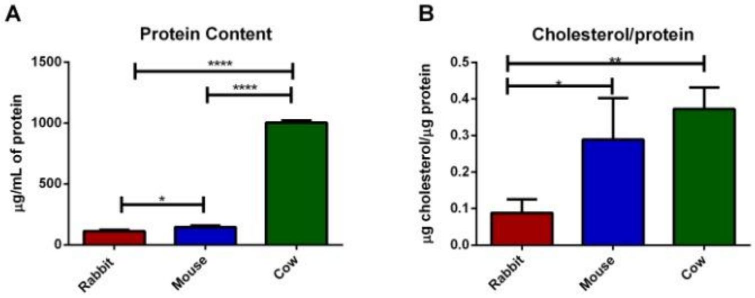

Figure 4.2 Platelet protein and cholesterol content. (A) Total % protein content for the same number of platelets compared to the total protein content of mouse platelets. (B) % ratio of the amount of cholesterol to the total protein content of platelets from each species compared to the mouse cholesterol ratio. Error bars are SD. For significance testing, one way ANOVA was used * for $p<0.05$, ** for $p<0.015$, **** for $p<0.0001$

with platelets containing more cholesterol showing greater secretion times and more foot events.[14] Due to the role cholesterol plays in fusion pore stability, determining the cholesterol concentration may help explain some of the kinetic differences among species' granule secretion. In addition to cholesterol content, it is important to understand the total protein to cholesterol content ratio because in studies where the ratios of lipids to proteins were varied, differences in lipid mixing during fusion were noted. In particular, SNARE proteins were studied and were shown to cause leakage and greater cell lysis as the ratio of proteins to lipids rose.[20,22] The total protein content and cholesterol to protein ratio in each species is shown in Fig. 4.2A and Fig. 4.2B, respectively. Relative to mouse protein content, rabbit only contained 77.7 ± 9.0% and cow contained 690.4 ± 1.8% total protein. However, when comparing the cholesterol to protein ratio, the amount of cholesterol located in cow platelets is balanced out by the high concentration of protein compared to mouse giving 129.0 ± 15.7% µg cholesterol/µg protein cow to the 100.0 ± 39.2 % µg cholesterol/ µg protein mouse. The rabbit cholesterol level was much lower than the protein level ratio only giving 30.7 ± 41.9 % µg cholesterol/µg protein compared to mouse. The concentration of cholesterol in platelets is not related to the amount found in the plasma of each species. Compared to mouse plasma, rabbit and cow plasma only contained 83 ± 4 % and 82 ± 6% of the total amount of cholesterol, respectively (Fig. 4.3).

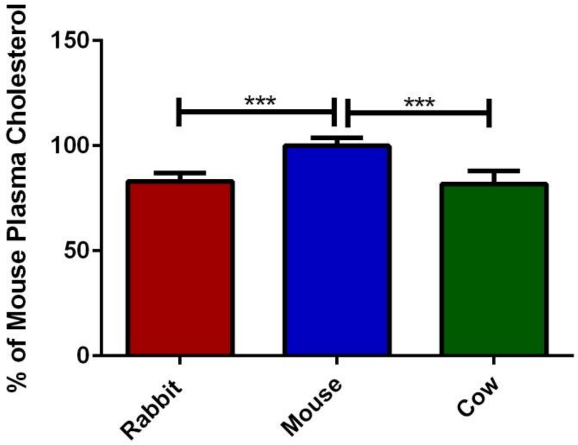

Figure 4.3 Concentration of cholesterol in the plasma of each animal compared to mouse plasma. Error bars given in SD and significance was determined using one way ANOVA. *** $p<0.001$

4.4.2 Platelet Perimeter

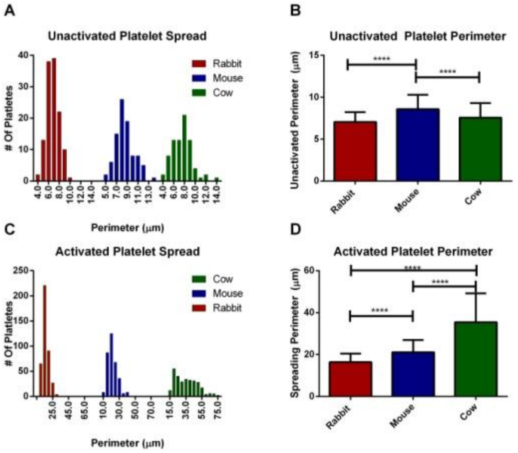

Figure 4.4 Activated and Unactivated platelet perimeter. Comparison of the platelet perimeter measured with Image J using TEM images for the unactivated platelets and darkfield microscopy images for activated platelets. Histogram of the perimeter of the unactivated platelets (A) and activated platelets (C) from each species showing the distribution of perimeters. The average perimeter is also shown for unactivated platelets (B) and activated platelets (D). Cow platelets show very little difference in their spread of perimeters and are approximately the same size as rabbit platelets when resting. However, upon activation, cow platelets have a wide spread and are significantly bigger than both mouse and rabbit. Significance was determined using one way ANOVA **** for $p<0.0001$. Error bars shown are SD.

Due to the variance of phospholipids, cholesterol, and protein in each of the species' platelets, it is important to determine if these differences are correlated to platelet size. In addition, the OCS has been hypothesized to be involved in platelet spreading, thus the spreading perimeter will allow us to understand how having an OCS may change the size of activated platelets. The size of the platelets was measured on both unactivated (TEM) (Fig. 4.4 A and B) and activated (CytoViva scope) platelets (Fig. 4.4 C and D) by measuring the perimeter of platelets from each species. The distribution of the unactivated perimeter size for each of the three species has a span of approximately 5.5 to 10 μm with average perimeters and standard deviation of 7.06 ± 1.17 μm for rabbit, 8.58 ± 1.71 μm for mouse, and 7.57 ± 1.74 μm for cow (n=125, 91, and 79, respectively).

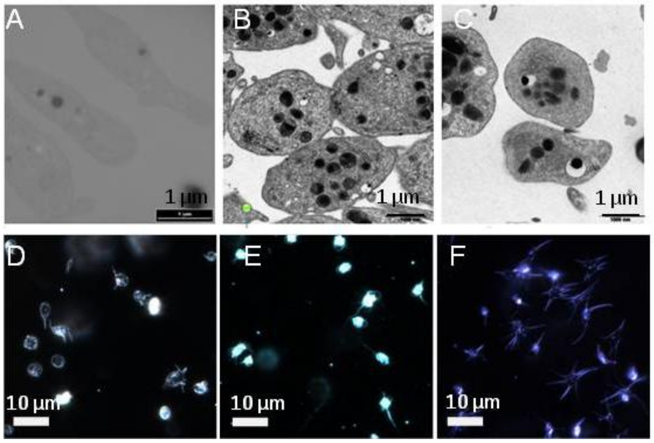

Figure 4.5 Platelet images. (A,D) rabbit, (B,E) mouse, and (C,F) cow images taken using TEM (A,B,C) and dark field microscopy (D,E,F). Rabbit TEM image taken by Emily Woo

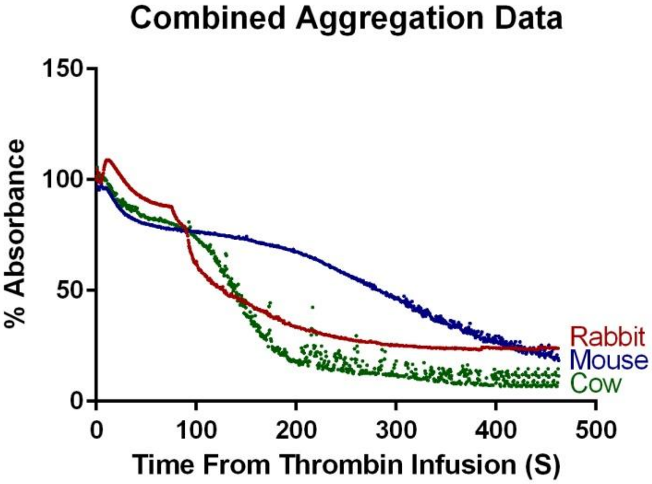

Figure 4.6 Normalized aggregation data for each species from time of thrombin infusion. Each plot contains three aggregation trials. The slope for the line of best fit for each data set was determined from the time of infusion until the absorbance value stabilized. These slopes were determined using Graphpad Prism software with the value of the combined slopes being -0.3222 for rabbit, -0.1610 for mouse, and -0.3731 for cow. The three slope values are statistically different from one another ($p \leq 0.0001$ using linear regression analysis in Graph Pad Prism)

Upon activation, the distance between the range of the total perimeter size increased. The majority of rabbit and mouse platelets had a range difference of 29.9 and 30.5µm respectively, while the majority of cow platelets had a span of 60.6 µm from the shortest to the longest perimeter of the platelets measured (Fig. 4.4C).The average spreading perimeter and standard deviation (Fig. 4.4D) for rabbit, mouse, and cow were 16.39 ± 4.07, 21.14 ± 5.81, 35.49± 13.72 µm, respectively. The activated shape of the platelets also varied between OCS and non-OCS species, with cow platelets creating a larger spread out square center with longer lamellipodia than either rabbit or mouse platelets. The rabbit platelets had shorter lamellipodia than either cow or mouse, but still maintained a similar center ellipse shape. Representative images of each of the species' unactivated and activated platelet structures can be seen in Fig. 4.5 A-C and D-F, respectively. In addition to spreading on a coverslip, the aggregation of platelets in suspension upon activation with 9.7 U/mL thrombin was monitored using an aggrogometer (Fig. 4.6). Each species aggregated various amounts with a 74 ± 8 %, 82 ± 4 %, and 90 ± 4 % change in absorption for rabbit, mouse, and cow, respectively.

4.4.3 CFMA General Spike Shape Analysis

δ-granule secretion upon exposure to two different agonists was evaluated by CFMA to determine effects caused by stimulation method vs. membrane structure. Fig 4.1D shows representative spikes corresponding to single secretion events upon thrombin (10 U/mL) or ionomycin (10 µM) stimulation of platelets isolated from different species. Although a numerical analysis of amperometric data is always needed, sometimes the shape of the representative spikes can reveal a lot about the amount and the kinetics of the secretion events. Except the mouse platelet, the spikes resulting from ionomycin and thrombin stimulation looked almost identical within the same species. Compared to the ionomycin stimulation spike, the representative spike for the thrombin-induced mouse platelet secretion is wider and shorter, indicating different secretion behavior that will be discussed later in detail. The representative spikes for cow platelets are both wider and larger than that of mouse and rabbit spikes. This indicates a slower but larger amount of serotonin secretion that will also be discussed below in detail.

4.4.4 Comparison of the Quantal Secretion Among Different Species

Regardless of the stimulation type, cow platelets secreted significantly more serotonin per secretion event (Fig. 4.7A and D) than either mouse or rabbit platelets (Q= 275.7±25.1, Q= 331.2±25.9, and Q=498.5±40.9 fC for rabbit, mouse and cow platelet secretion, respectively upon ionomycin stimulation; Q=271.5±21.7, Q=313.9±29.5, and Q=654.9±116.4 fC for rabbit, mouse, and cow platelets secretion upon thrombin stimulation, respectively). Compared to cow platelets, both rabbit and mouse platelets secreted a significantly higher number of discrete δ-granules per exocytotic event (N= 9.6±1.3, 8.1±1.1, and 4.2±0.3 granules for rabbit, mouse and cow platelets, respectively, for ionomycin stimulation. For thrombin stimulation, N=17.2±2.1, N=6.9±0.6, N=3.0±0.3 for rabbit, mouse, and cow) (Fig. 4.7B and E). Using Faraday's Law, N and Q gives the average moles of serotonin secreted from each platelet; the number of moles of serotonin calculated from N*Q values by using Faraday's Law are 17.5×10^{-18}, 13.8×10^{-18}, $9.6\times10^{-}$ (Fig. 4.7C and F) assuming that all secreted serotonin is measured.

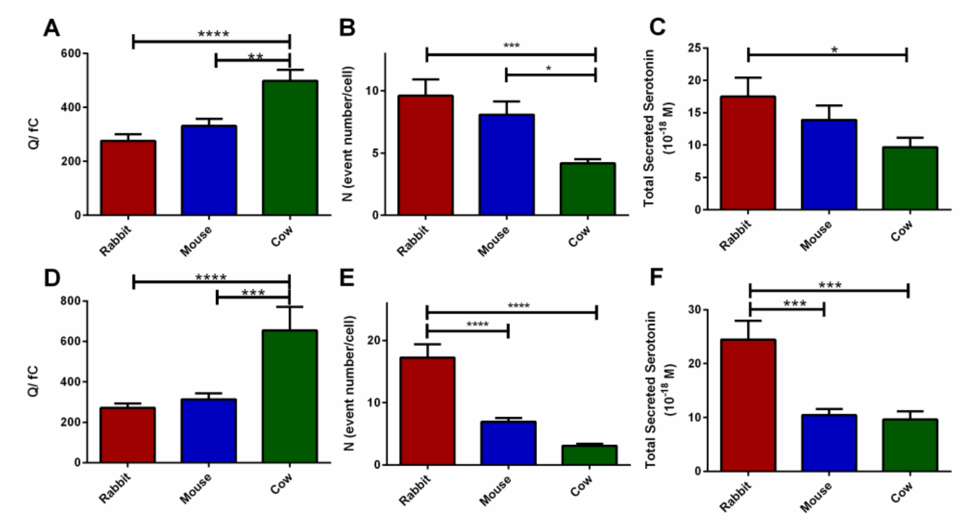

Figure 4.7 Comparison of the quantal release between the species upon ionomycin (A-C) (N = 23, 35, 39 for rabbit, mouse, and cow) and thrombin (D-F) (N= 32, 34, 22 for rabbit, mouse and cow) stimulations. (A, D) Cow platelets release significantly more serotonin molecules per release event (as denoted by Q, the charge under the amperometric spike). (B, E) The number of granules released per single platelet exocytosis. (C, F) N*Q represents the total amount of serotonin secreted from individual platelets in each condition. Using one way ANOVA * for $p<0.05$, ** for $p<0.01$, and *** for $p< 0.001$. Error bars are SD.

Previous studies on α-granule secretion in cow platelets show that they fuse with each other during exocytosis, prior to fusion with the plasma membrane.[23] A similar phenomenon for δ-granule secretion could explain the higher Q and lower N values for cow platelet secretion compared to the other two species. The frequency distribution of the Q values was analyzed (data not shown), expecting a bimodal distribution to show that a sub-population of δ-granules fuse with each other ahead of plasma membrane fusion. However, frequency analysis did not show such a distribution; a single non-Gaussian distribution similar to the previously reported distribution for rabbit granular secretion was observed instead,[13] making the possibility of fusion of two or more δ-granules unlikely. In addition, TEM images were used to analyze the size of δ-granules in cow and mouse platelets (Fig. 4.8). Results showed that cow platelets not only have larger δ-granules but that the dense core of the δ-granules, where most of the serotonin is stored, is significantly larger in cow platelets (average granule diameter is 230.6±6.1 nm for mouse platelet δ-granules versus 343.0±11.1 nm for cow platelet granule). This larger dense core and granule are the likely reason that more serotonin is secreted during each individual event.

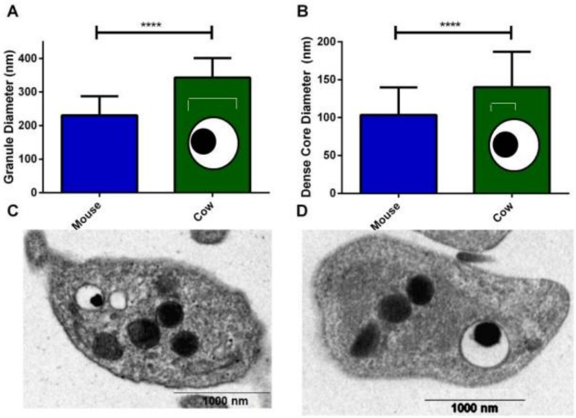

Figure 4.8 TEM analysis of cow (26 granules) and mouse (86 granules) platelet δ-granules. Cow platelets, on average, have larger δ-granules (A) and dense core diameters (B). The cartoon granules show the distance measured for each graph Representative TEM images of a single mouse platelet (C) and cow platelet (D). Significance was determined with a T test **** for P< 0.0001 and error bars are standard deviation.

As described by Ewing and colleagues, it is not necessarily true that the entire content of a granule is released upon stimulation and exocytosis; in fact, PC12 cells, a model exocytotic cell, only release 45% of their vesicular content.[24] Herein, we evaluated the percentage of total δ-granule content release using bulk HPLC measurements by lysing the cells with $HClO_4$ and analyzing the total serotonin content and comparing this amount with the serotonin secreted following exposure to either 10 U/ml thrombin or 10 µM ionomycin. Data presented in Fig. 4.9

show the percent of total serotonin secreted upon stimulation for each species and stimulant. From the data, it is clear that more serotonin is secreted in OCS-containing species upon thrombin activation as compared to ionomycin activation. In both rabbit and mouse platelets, the granules secrete more than 50% of the total serotonin content; however, only 27.5 and 41.1% of the serotonin was secreted from cow platelets with ionomycin and thrombin stimulation, respectively ($p<0.001$). Application of human thrombin to stimulate non-human platelets cannot be the reason for this behavior since it has been shown previously that human thrombin was 89% homologous to cow thrombin, and cow platelets are known to respond similarly to human and cow thrombin.[6] This may indicate that the reduced cow platelet secretion, compared to that by rabbit and mouse platelets, may not be due to the effectiveness of the stimulant but efficiency of the response to the stimulant, perhaps related to the use of the OCS.

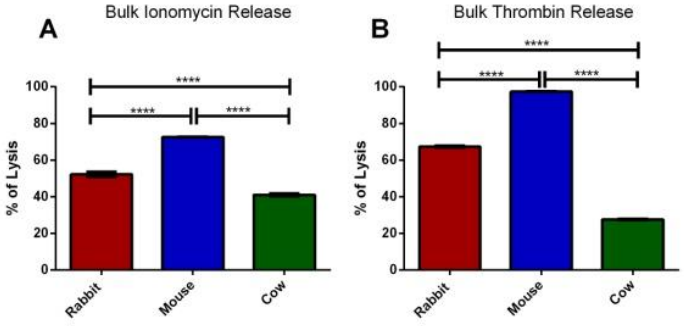

Figure 4.9 Bulk serotonin analysis using HPLC with electrochemical detection. % of the total serotonin secreted with (A) ionomycin stimulation or (B) thrombin stimulation. Using one way ANOVA **** for $P<0.0001$

4.4.5 Comparison of the Secretion Kinetics among Different Species

In amperometric traces, T_{rise} values measure the time required for transition from 10% to 90% of the spike amplitude maximum, revealing the chemical messengers secreted as the granule transitions from the initial pore opening to full fusion. During this time, the soluble (non-polyphosphate-associated) serotonin present in the granules is secreted.[25] In contrast, $T_{1/2}$ is a measure of the total time of a serotonin secretion event which can be influenced by the opening of the fusion pore, the size of the expanded pore, dissolution of the matrix-bound serotonin, and diffusion of that serotonin into the extracellular space. When stimulated with ionomycin, cow platelets showed slower secretion kinetics than either rabbit or mouse platelets (larger T_{rise} and

$T_{1/2}$ values) (Fig. 4.10). Mouse and rabbit platelets showed comparable secretion kinetics upon ionomycin stimulation ($T_{1/2}$= 13.9±1.1 and 14.7±1.1 ms for mouse and rabbit, respectively). Thrombin, however, induced distinct secretion behavior for each species. Although mouse and rabbit platelets secrete similar amounts of serotonin from δ-granules, mouse platelet secretion was much slower than that from rabbit platelets ($T_{1/2}$= 20.3±1.2 and 15.4±1.2 ms for mouse and rabbit, respectively). Cow platelet secretion kinetics were slower in thrombin-induced stimulation with a $T_{1/2}$ value of 26.8± 2.1 ms compared to 29.2±.1.7 ms with ionomycin.

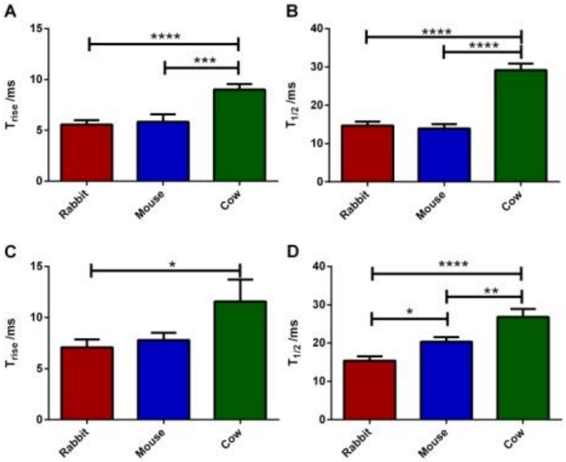

Figure 4.10 Comparison of the secretion kinetics from individual granules with either (A, B) ionomycin or (C, D) thrombin stimulation (A, C). Larger T_{rise} values from cow platelet secretion indicate slower transition to maximal release. (B, D) Duration of the total secretion was longest in cow platelets regardless of the stimulant. Although the $T_{1/2}$ values from rabbit and mouse platelets were similar in the ionomycin condition, thrombin stimulation resulted in higher $T_{1/2}$ values, and thus, slower release from mouse platelets compared to rabbit platelets. Using one way ANOVA * for $p<0.05$, ** for $p<0.015$, *** for $p<0.001$, **** for $p<0.0001$ N values for Ionomycin stimulation are 23, 35, 39 for rabbit, mouse and cow respectively and 32, 34, 22 for thrombin stimulation. Error bars are representative of the standard deviation.

4.4.6 Comparison of Fusion Events between Species

During platelet granular secretion, fusion of the granular membrane with plasma membrane gives rise to a fusion pore of limited stability. Fusion pore formation and stability influences both the quantal secretion and kinetics of secretion.[26,27] In amperometric traces, the fusion pore can be identified as a subtle increase in the current due to the diffusion of soluble serotonin as the fusion pore opens (Fig. 4.1C); this current feature is commonly known as a "foot." [25]

The analysis of the foot events among amperometric spikes shows that the stability of the fusion pore is highly dependent on the species and mechanism of the activation (Fig. 4.11). Mouse platelets showed the highest, though not significant, percent of fusion pore events when they were activated with ionomycin (18.1±3.6% of the mouse secretion events showed a foot feature as opposed to 9.5±2.0 and 13.5±2.5% fusion pore events in rabbit and cow exocytosis, respectively). Stimulation of mouse platelets with thrombin caused a drastic decrease in secretion events initiated through a stable fusion pore (9.3±2.3% events with foot). On the other hand, thrombin stimulation caused a significant increase in the stability of the fusion pore during rabbit and cow platelet dense granule secretion (%Foot= 15.0±2.1 and 23.7±5.1 for rabbit and cow platelets, respectively). This indicates that fusion pore stability based on the variations in formation of foot for rabbit, mouse and cow, is both species and stimulant dependent, and there is no correlation between the presence of OCS and fusion pore occurrence.

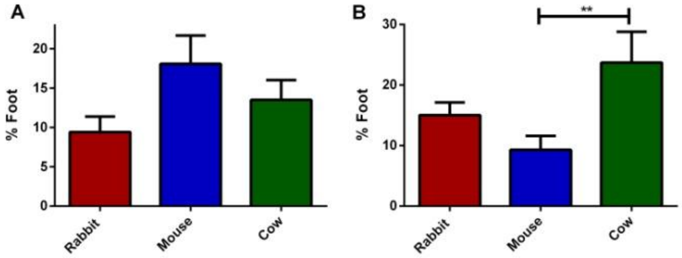

Figure 4.11 Platelet fusion pore analysis. (A) Ionomycin stimulation (B) Thrombin stimulation. Thrombin resulted in the most stable fusion pores in cow platelets, higher than those measured from mouse or rabbit platelets. Using one way ANOVA ** for p<0.01. Error bars are reported with standard deviation

4.4.7 Discussion

Revealing the differences among platelets of different species will help clarify the role of each component of platelet secretion and determine how a cell may compensate for a missing component. One of the major structural differences between platelets from different species is the presence of a system of tunneling invaginations from the plasma membrane known as the OCS.[4,6,28] Work done by various groups has demonstrated that the OCS influences platelet morphology during activation and that the presence of the OCS helps platelets interact with surfaces better by facilitating platelet spreading and pseudopodia formation.[23,29] Moreover, it was shown that the OCS membrane contains SNARE proteins, including syntaxin 2, SNAP 23 and VAMP 3 and is involved in platelet granular secretion by serving as intermediate fusion sites for the granules before plasma membrane fusion.[28] However, the very active hemostatic function of camel platelets (lacking an OCS) raises the question of the actual need and use of these tubular structures in platelets.[4] In 2010, the Whiteheart group showed that the proteins that regulate the actin cytoskeleton are expressed at higher levels in OCS-containing platelets.[6] This work inspired the hypothesis that the OCS is critically involved in granule trafficking and docking ahead of chemical messenger secretion.

During granule docking with the platelet plasma membrane, granules are thought to dock preferentially in cholesterol-rich microdomains which have been shown to contain almost twice as much SM and 4 times the amount of cholesterol compared to the regular membrane.[30] These sphingolipid/cholesterol rich microdomains are known to play a significant role in exocytosis due to their ability to stabilize the fusion pore and also concentrate certain soluble NSF attachment protein receptor (SNARE) proteins while excluding regulating SNARE proteins.[14,21] This work shows that cow platelets contain a significantly greater concentration of SM, with over a 10 fold increase and a 600% increase in cholesterol compared to mouse and rabbit platelets, respectively even while accounting for unactivated platelet size. This excess cholesterol and SM could be an indication of the platelet being able to form a larger number of lipid rafts to facilitate granule docking since these platelets do not have an OCS which is easily accessible throughout the platelet. In addition, the cow δ-granules have shown greater stability than those from mouse or rabbit as seen by their longer t_{rise}, $T_{1/2}$ times and also their ability to form more foot features (Fig. 4.11). These trends of increased stability with increasing cholesterol have been seen in a previous work from our group. In this prior study, rabbit platelets were depleted of 32% of their cholesterol using methyl-β-cyclodextrin or incubated in cholesterol, increasing the concentration to 132% of the original cholesterol content. As cholesterol increased, T_{rise}, and foot features increased.[14] If a similar cause is the source of cow platelet behavior, this suggests that cow platelets, which do not contain an OCS, may have a membrane richer in lipids that are beneficial to stability during secretion.

Measurement of total serotonin content vs. total secreted serotonin with HPLC facilitates evaluation of the efficacy of the secretion among the OCS- and non-OCS containing platelets. Cow platelets secrete a drastically smaller percentage of total serotonin than either mouse or rabbit platelets. Furthermore, the parameter that was used to determine the kinetics of the secretion event ($T_{1/2}$) was significantly larger for cow platelets. Although the higher $T_{1/2}$ value may be due to the higher amount of serotonin secreted, it is possible that the absence of the tubular structure retarded secretion kinetics. All these observations indicate that the OCS may not be necessary for chemical messenger secretion, but it indeed influences the efficacy of the secretion.

Previous research has shown differences in “spreading” between platelets with and without an OCS. According to Grouse et al., “bovine platelets do not spread, they unfold” since only OCS platelets are able to fill in the spaces between pseudopods. One hypothesis for this difference in spreading behavior is that the OCS provides extra surface area upon activation and slight variations in the cytoskeletal organization.[29] However, even without the extra membrane space of the OCS, cow platelets are still able to increase their total perimeter to a much greater extent than either mouse or rabbit platelets. This is partially due to the long pseudopods that extend out into the extracellular environment (Fig. 4.5). The range of activated cow platelet perimeters are spread out to a greater extent than either rabbit or mouse. In OCS platelets (mouse and human), it has been shown that alpha granules fuse with the plasma membrane and contribute to platelet spreading.[31] With the excess cholesterol and SM helping stabilize the granule, it would be reasonable for more granules to go through full fusion instead of endocytosing therefore helping spread. Due to the larger size of the δ-granule and slight variations in how many granules are able to reach the membrane, this amount of spreading would be widely variable within a population of platelets.

4.5 Conclusion

In conclusion, by using a variety of complimentary techniques to determine kinetic secretion, lipid composition, and imaging, we have demonstrated the similarities and differences in platelet δ-granule secretion behavior and membrane composition of platelets from different species. In addition, membrane lipid composition indicates that cow platelets may have increased their SM and cholesterol composition to compensate for the lack of OCS. Finally, variations in secretion between stimulants did not show trend changes except for percentage foot values, indicating that secretion is affected to a greater extent by the composition of the platelet than the stimulation used to initiate activation.

Chapter 5: Characterization of the Presence and Function of Platelet Opioid Receptors

This work was completed with the assistance of Danielle H. Francis, Audrey F. Meyer, Ben M. Meyer, Donghyuk Kim, and Christy L. Haynes

5.1 Overview

Opioids are typically used for the treatment of pain related to disease or surgery. In the body, they enter the blood stream and interact with a variety of immune and neurological cells that express the μ-, δ-, and K-opioid receptors. One bloodborne cell-like body that is not well understood in the context of opioid interactions is the platelet. The platelet is a highly sensitive anucleate cell-like fragment that is responsible for maintaining hemostasis through the secretion of chemical messengers and shape change. This research delves into characterizing platelet opioid receptors, how specific receptor agonists impact platelet exocytosis, and the role of the K-and μ-receptors in platelet function. Platelets were found to express opioid receptors, but upon stimulation with their respective agonist, no activation was detected. Furthermore, exposure to the opoid agonists did not impact traditional platelet secretion stimulated by thrombin, a natural platelet activator. In addition, with the use of knockout mice, these data suggest that the agonists may be interacting non-specifically with platelets. Finally, K-knockout platelets showed variations in their ability to adhere and aggregate compared to control platelets.

5.2 Introduction

Opioids, a class of drug molecules including heroin, opium, codeine, morphine, oxycodone, and fentanyl, are used for the treatment of moderate to severe pain caused primarily by cancer, surgery, and arthritic diseases. [1-3] In 2009, over 250 million prescriptions were written in the US, an increase of 82 million prescriptions since 2000. [4] In addition, the abuse of illegal opioid substances has increased over 414% from 1997 to 2007. [5] Upon introduction into the body, opioids bind to at least one of the three G protein-coupled receptors (mu (μ), kappa (K), and/or delta (δ)).[6-9] In addition, opioids are able to cross-interact between the receptors, activating different signaling pathways. One example includes morphine, which binds to the μ- and δ-opioid receptors. However, the affinity of morphine, a common pain reliever, is 50x greater for the μ-receptor than the δ-receptor. [10, 11] In contrast, agonists for the K-receptor have been noted to play a more direct role in the immune system. Several immune cells are known to express opioid receptors, and many, including natural killer cells, mast cells, and neutrophils, have shown a significant evolution in cell response when exposed to opioids over an extended period of time. [6, 8, 12-14]

One immune cell-like body that has been largely overlooked in opioid research is the platelet. Platelets play a crucial role in hemostasis, but are also intimately involved in serious health risks including stroke and myocardial infarction upon unwanted clotting or excessive bleeding. Upon activation, platelets secrete chemical messengers from three distinct granule types, the δ-granule, the alpha granule, and the lysosome. The δ-granule contains small molecules including serotonin, adenosine diphosphate (ADP), adenosine triphosphate, Ca^{2+}, and histamine, all of which play a role in vascular constriction, inflammation, and activation. The alpha granules contain platelet factors (PFs) including PF4, clotting proteins, and adhesion molecules. The lysosomes, which are rare in platelets, contain hydrolases including beta hexosaminidase (β-Hex). [15, 16] Due to the heavy use of intravenously injected opioids during surgery, and 40-60% of the opioid content entering the blood stream, platelets have ample opportunity to interact directly with these drugs. [8]

Current platelet-opioid interaction research has been focused on studying the effects of various opioid anesthetic agents on perioperative bleeding. [17-19] To the best of our knowledge, only one paper has studied platelets directly by observing the binding attachment of naloxone, an opioid antagonist, on human platelets. [20] The purpose herein is to explore the fundaments of how the opioid receptors and receptor agonists impact platelet function by establishing which G protein-coupled opioid receptors are present on platelets, how stimulation of each individual receptor impacts granule secretion, and which roles the receptors play in normal platelet function. For stimulation, to prevent cross-interaction when studying receptors, the agonists [D-Ala^2, NMe-Phe^4, Gly-ol^5]Enkephalin (DAMGO), [D-Pen^{2,5}]Enkephalin, [D-Pen^2,D-Pen^5]Enkephalin (DPDPE), and U-50488 were used to stimulate the µ-, δ-, and K-receptors, respectively. To determine the role of individual receptors, K- (Jackson Laboratory B6.129S2-Oprk1tm1kff/j) and µ- (Jackson Laboratory B6.129S2-OPRM1TM1KFF/J) opioid receptor knockout (KO) mice were purchased. Due to limited availability, δ-KO mouse studies could not be included in this work.

5.3 Experimental Approach

5.3.1 Reagents

All chemicals for the buffers and HPLC mobile phase were purchased from Sigma Aldrich. Western blot stock solutions were purchased from Bio-Rad laboratories unless otherwise indicated.

5.3.2 Platelet Isolation

Control C57BL/6J, µ - KO B6.129S2-Oprm1^{tm1Kff}, and K - KO B6.129S2-OPRK1$^{TM1KFF/j}$ mice were purchased from The Jackson Laboratory. Blood was collected via cardiac puncture following IACUC protocol #1403-31383A. Briefly, mice were euthanized via CO_2 asphyxiation, and then a syringe filled with 200 µL acid citrate dextrose (ACD) was used to draw blood via cardiac puncture. The blood was diluted with Tyrodes buffer (NaCl, 137 mM; KCl, 2.6 mM; $MgCl_2$, 1.0mM; D-glucose, 5.6 mM; N-2-hydroxyethylpiperazine- N'-2-ethanesulfonic acid (HEPES) 5.0 mM; and 12.1 mM $NaHCO_3$, with pH adjusted to 7.3) and centrifuged at 130 x g for 10 min with reduced braking to prevent platelet activation. The top platelet rich plasma layer was collected, and additional ACD and Tyrodes buffer were added. The platelets were pelleted at 524 x g for 10 min with reduced braking. The pellet was re-suspended in fresh Tyrodes buffer and platelets were counted using a hemocytometer. All platelets were diluted to the lowest platelet density for each experiment, which typically ranged between $1x10^7$-$1x10^8$ platelets/ml.

5.3.3 Western Blot

Platelets were re-pelleted at 524 x g and re-suspended in a couple hundred µLs of Tyrodes buffer to increase concentration. For the opioid control, brain cells were extracted from C57BL/6J purchased from The Jackson Laboratory after euthanasia via CO_2 asphyxiation following IACUC protocol #1403-31383A. Platelets used for western blotting were tested both from samples recently collected from mouse donors and samples frozen at -80 °C. The brain collected after CO_2 euthanasia under IACUC protocol #1403-31383A was broken into small chucks and put in Tyrodes buffer. The brain cells were frozen at -80 °C. After thawing, both platelets and brain cells were roughly pipetted and sonicated for 10 minutes. A 5% by volume solution of 2-mercaptoethanol in Laemmli buffer was added to the cell solution in a 1:1 ratio. The sample was vortexed for 30 seconds, put into a heating block, and boiled for 5 minutes.

12.5% Criterion™ Tris-HCl Gel purchased from Bio-Rad laboratories was inserted into a gel electrophoresis housing containing 1x Tris/Glycine/SDS (TGS). Samples and a precision plus protein standard dual color ladder from Bio-Rad were pipetted into their respective wells. The power was set at 110 volts, and the gel was run until the bottom of the ladder was near the end of the gel (around 90 min). A blotting sandwich was set up, keeping the components wet with cold Towbin buffer (1x Tris/Glycine (TG) in 20% methanol). The sandwich was placed in the transfer apparatus and inserted into the transfer cell filled with cold Towbin buffer and a stir bar. The power supply was set at 500 mA or ~100 volts and run for 120 min in a cold room on a stir plate.

The nitrocellulose membrane was incubated with 5% (w/v) powder skim milk in 1x tris buffered saline with 0.1% Tween-20 (TBS/T) buffer for 60 min on a shaker at 300 rpm. The membrane was washed 3x for 5 min in TBS/T buffer at 300 rpm and finally placed into baggies containing the antibody in 4% powdered skim milk in TBS/T buffer. The µ, δ and K antibodies (Millipore anti- µ opioid receptor AB1580-1 rabbit polyclonal, Thermo Fisher Scientific PA5-

26138 OPRM1 antibody, Millipore Ab1560 rabbit anti-δ opioid receptor polyclonal antibody, and Abcam Anti- K opioid receptor antibody ab10566) were diluted 1:1000. The bags were placed in a cold room overnight with gentle rotation. The membrane was removed and washed 3x with TBS/T buffer on a shaker at 300 rpm and finally incubated with Rockland Immunochemical's secondary anti-rabbit HRP-conjugated antibody (1:5000 dilution) in 4% powdered skim milk for 60 min. After incubation, the membranes were washed 3 X with TBS/T buffer in a rotator at 300 rpm for 5 minutes.

While washing the membrane, a mixture of 1:1 luminol solution and stable peroxide solution from the Super Signal West Femto Maximum Sensitivity Substrate kit (Pierce) was mixed. The membranes were laid onto plastic wrap, and the substrate was pipetted dropwise over the proteins/antibodies. After 5 minutes, the membrane was dabbed to remove excess reagent and wrapped into plastic wrap. X-ray film was placed over the membrane and developed using a SRX101A medical film processor (Konica Minolta Medical and Graphic Inc.)

5.3.4 Figure 1 Platelet Stimulation Procedure

125 µL of platelet suspension was put into 1.7 mL Eppendorf tubes. The platelets were then incubated with 125 µL of opioid agonist in Tyrodes buffer at a final concentration of either 10 nM DAMGO, 3 µM DPDPE, 100 nM U-50488, or Tyrodes buffer. The platelets were pelleted at 1200 xg, and the supernatant was collected for serotonin detection. The platelets were re-suspended in 125 µL Tyrodes buffer and incubated for 15 min before 125 µL of 1 U/mL thrombin was added for a final concentration of 0.5 U/mL thrombin. After 20 minutes of thrombin stimulation, the platelets were spun down at 1200 xg, and the supernatant was collected for serotonin detection.

5.3.5 Figure 2 - 4 Platelet Stimulation Procedure

125 µL of platelet suspension was put into 1.7 mL Eppendorf tubes. The platelets were then incubated with 125 µL of stimulant in Tyrodes buffer at a final concentration of 10 nM DAMGO, 3 µM DPDPE, 100 nM U-50488, 0.5 units/mL thrombin, Tyrodes buffer, or 0.25 M $HClO_4$ in water. After 30 min, 100 µL of ACD was added and the platelets were spun down at 500 xg. The supernatant was used for the serotonin, PF4, and β-hex assays. The platelet pellet was used for the BCA assay. The platelets in the Tyrodes buffer were used for cholesterol detection.

5.3.6 Serotonin Detection

200 µL of the supernatant was filtered using a Millipore 96 well Multi-Screen HTS filter plate (Billerica, Ma) with a 0.45 µm pore size. The supernatant was filtered through at 3000 xg for 5 minutes, and 180 µL of it was combined with 20 µL of 5 µM dopamine internal standard in 0.5 M perchloric acid. The serotonin was detected using a previously developed HPLC method using electrochemical detection.[21, 22] Briefly, a Waters 2465 electrochemical detector with a glassy carbon electrode was attached to a Agilent 1200 HPLC with a 5 µm 4.6 x 150 mm C18 column (Eclipse XDB-18). The samples were auto injected into the mobile phase (11.6 mg/L of sodium octyl sulfate, 170 µL/L dibutylamine, 55.8 mg/L Na_2EDTA, 10% methanol, 203 mg/L anhydrous sodium acetate, 0.1 M citric acid, and 120 mg/L sodium chloride) flowing at 2 mL/min. The dopamine (an internal standard) and serotonin spikes were detected using a potential of 700 mV vs. Ag/AgCl and a current range of 50 nA. Concurrently, a calibration curve was run with serotonin concentrations varying from 0-1 µM serotonin and 0.5 µM dopamine internal standard in 0.5 µM perchloric acid.

5.3.7 PF4 ELISA Assay

Alpha granule content secretion was detected as directed using an enzyme linked immunoassay kit for PF4 (R&D Systems). Briefly, supernatants were diluted with Calibrator Diluent RD5-26 (1X). Assay Diluent RD1-40 and the sample were added to each well in the provided plate. The plate was incubated for 2 hours, and the wells were washed. Mouse PF4 Conjugate was added to each well, incubated, and washed. Finally, substrate solution was put in the wells for incubation, and then a quenching solution was added. The optical density was determined with a BioTek Synergy 2 96 well plate reader.

5.3.8 B-Hexosaminidase Assay

An absorbance assay for β-Hex was prepared as previously described.[23] Briefly, a solution of 1 mM p-nitrophenyl acetyl-D-glucosamine in 0.1 M citrate buffer was added to the sample and incubated for an hour. Ice cold 0.1 M carbonate buffer was added to stop the reaction. The absorbance was read at 405 nm with background subtraction at 630 nm.

5.3.9 BCA Protein Assay

Platelet protein content was measured using the Pierce BCA Protein Assay kit (Thermo Scientific) following included directions. Briefly, after collecting the supernatant used in experiments from Fig. 2 and 4, the pellet was homogenized in 25 µL of Tyrodes buffer. 200 µL of working reagent was added to each well and the plate was incubated for 30 min at 37^{o}C. The plate was read at 562 nm on a BioTek Synergy 2 96 well plate reader. Due to small pellets, when the supernatant was removed, a small portion was left inside each vial as to not disturb the pellet. Therefore, upon addition of Tyrodes buffer, there may have been slight variations in the total pellet dilution.

5.3.10 Platelet Cholesterol Assay

The concentration of cholesterol was determined as directed using an Amplex Red Cholesterol Assay Kit (Life Technologies). To ensure similar platelet count between mouse models, the concentration of platelets was determined using a hemocytometer and diluted to the lowest platelet concentration among the three conditions. 125 µL of platelet suspension was pelleted, and the pellet was mechanically homogenized in 1x Reaction Buffer to expose internal cholesterol. The absorbance was measured at 590 nm after exciting at 530nm using a BioTek Synergy 2 96 well plate reader.

5.3.11 Platelet Adhesion

Platelet adhesion studies were performed on a straight channel microfluidic device as previously described.[24,25] Briefly, channels were coated with a confluent monolayer of hy926 human endothelial cells (ATCC). Platelets were labeled with CMFDA (5-chloromethylfluorescein diacetate) dye (2 µM, 20 min) for easier visualization and then stimulated with 5 µM ADP or left un-stimulated in the Tyrodes buffer. ADP was utilized because it can initiate adhesion without secretion, therefore decoupling secretion and adhesion in this assay.[26] The cells were flowed through the device at 30 µL/hr for 20 minutes. The device was washed with Tyrodes buffer, and the number of adherent cells was counted using a Nikon Microscope with a QuantEM Photometrics CCD camera. Metamorph Ver. 7.7.5 was used as the imaging and analysis software.

5.3.12 Platelet Aggregation

500 µL of 2 x 10^{8} platelets were placed in a small glass tube with a stir bar. The tube was placed into a Chrono-Log Whole Blood Lumi aggregometer interfaced with Aggro/Link software. A tube with Tyrodes buffer was placed into the aggregometer for baseline comparisons. After the absorbance stabilized at 100%, 120 µL of 25 U/mL thrombin was added for a final concentration

of 4.8 U/mL thrombin. The % absorbance over time was measured until the absorbance no longer changed. The data was then converted to % transmittance. To calculate the change in transmission, the % transmittance was averaged before stimulation and then the average percent transmittance after the decrease was subtracted. For rate of aggregation calculations, the time was considered from when the thrombin was injected until the % transmittance reached the average final value.

5.3.13 Platelet Dark Field Imaging

4 µL of the platelet suspension was deposited on a glass slide, and a coverslip was gently placed on top before being sealed with clear nail polish. The platelet samples were allowed to settle and activate before imaging. Images were captured on an Olympus microscope from CytoViva with and UplanFLM 100x oil immersion objective and Dage XL camera. The image exposure time was adjusted manually in the Exponent 7 software and had to be increased for both the µ- and K-KO platelet images based on lower overall scattering signals.

5.3.14 Data analysis

GraphPad Prism 6 was used to analyze all statistical data. All significance was determined using one way ANOVA. Figure error bars show standard deviation. Fig. 1 had 5 biological replicates for all conditions except Tyrodes which had 10 biological replicates. Figures 5.2, 5.3, 5.4, and 5.6 had 4 biological replicates except for the PF4 Tyrodes conditions, which only had 3 biological replicates due to limited space. Fig. 5.5 had 5.6 replicates for each condition. For dark field imaging, two slides were prepared for each type of platelet and ~10-15 images were recorded for each slide.

5.4 Results and Discussion

Literature precedent on the effects of opioids and their receptors on platelets have focused on the aftereffects of anesthetic agents on clotting. While this is important to understand for surgical use, it is also important to understand the fundamentals of how the agonists are interacting with the platelets by leveraging analytical and biological chemistry techniques. This knowledge of the role each opioid receptor has on platelet function can then be exploited to predict how certain drugs will interact with platelets and influence platelet function.

5.4.1 Verification of Opioid Receptors on Platelets

Platelets are sensitive to a vast array of molecules that cause activation including thrombin, collagen, and ADP. These compounds induce different coagulation pathways causing varied amounts of aggregation and exocytosis of the alpha, δ, and lysosome granules. Activation also induces upregulation of different fibrinogen binding sites and cytoskeleton rearrangement for better adhesion/interaction.[27] In addition to natural stimulants, many drugs affect normal platelet function, varying from direct platelet activation to prevention of exocytosis. [28] To fully understand the effects of opioids on platelets, it is important to first determine which receptors the platelets express. Previous literature has demonstrated that platelets are impacted by the antagonist naloxone, which primarily binds to the µ receptor, but also has slight affinity for the δ and K receptors. [20]

Western blots using µ-, δ-, and K-antibodies demonstrate the presence of all three receptors on control mouse platelets. In addition, western blots on the µ- and K-KO mice demonstrated that the K- KO mice had a knocked-out K receptor and still contained both the µ- and δ-receptor. However, the same experiments on the µ-KO mouse demonstrated that all three receptors were still present. A different antibody and a new µ-KO mouse were purchased for confirmation with the same outcome. In addition, tail clippings from the original mice were sent to TransnetYX (Cordova, TN) to confirm the µ-gene was knocked out. While the gene knock-out was confirmed, the results indicated all three receptors were still present in the western blot. This suggests either that both µ-antibodies are binding non-specifically or that there may be a µ-like receptor expressed by the platelet.

5.4.2 Platelet Secretion in Response to Opioid Agonists

The role of each receptor in platelet granule secretion was analyzed using receptor-specific agonists. For initial experiments, control platelets were incubated for two hours with the opioid agonists DAMGO, DPDPE, or U-50488 that target the µ-, δ-, and K–receptors, respectively. The supernatant was analyzed for serotonin from δ-granule secretion after the platelets were spun down (Fig. 5.1A). The platelets were re-suspended and then stimulated with thrombin, a natural platelet stimulant, for 20 minutes. The supernatant was collected and analyzed (Fig. 5.1B). Secretion from δ-granules was not apparent in platelets incubated with the agonists, nor did these agonists influence natural platelet stimulation by thrombin.

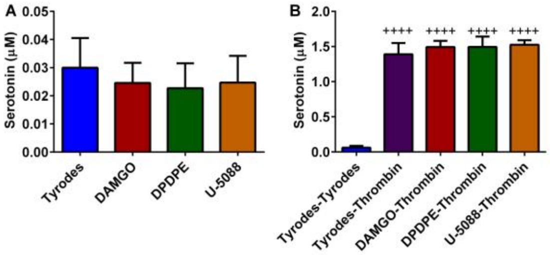

Figure 5.1 Effects of opioid agonists on platelet function. Control platelets were incubated with Tyrodes buffer (negative control), DAMGO (μ opioid receptor agonist), DPDPE (δ opioid receptor agonist), or U-50488 (K opioid receptor agonist) for two hours. The platelets were pelleted, and the supernatant serotonin concentration was analyzed (A). The platelet pellet was re-suspended and stimulated with thrombin or Tyrodes buffer for 20 minutes, and the serotonin release was measured (B). $^{++++}$ P≤0.01 vs. Tyrodes condition

These data are comparable to previously cited data examining post-operative bleeding and clotting, which did not show significant differences when comparing platelets that had and had not come into contact with opioids.[17-19] However, there was a downward change in serotonin secretion in the agonist-activated platelet supernatant compared to our negative control, Tyrodes buffer. These data suggest that the opioids may help stabilize un-stimulated platelets, but upon thrombin stimulation, the total amount of serotonin secreted is not impacted. To further investigate this trend, the first part of the experiment was run again with 30 minute thrombin stimulation (Fig. 5.2A). Again, the downward change in serotonin secretion from δ-granules was detected. Some of the supernatant from the platelet suspension was also used to analyze the amount of platelet factor 4 secreted from alpha granules (Fig. 5.2B) and β-Hex from lysosomes (Fig. 5.2C). For both alpha granules and lysosomes, there was no significant difference in content secretion with opioid stimulation compared to the negative control. This indicates that platelets interacting with opioids are not always more stable as demonstrated with the δ-granule, but also may have no secretion to very little secretion.

The role of the individual receptors and specific agonist-receptor interactions was analyzed using K- and μ-KO mouse platelets. The δ-granule secretion response was monitored in both resting platelets (Fig. 5.3B) and thrombin-stimulated (Fig. 5.3C) platelets relative to the total amount of serotonin they contained (to ensure that the KO platelets were

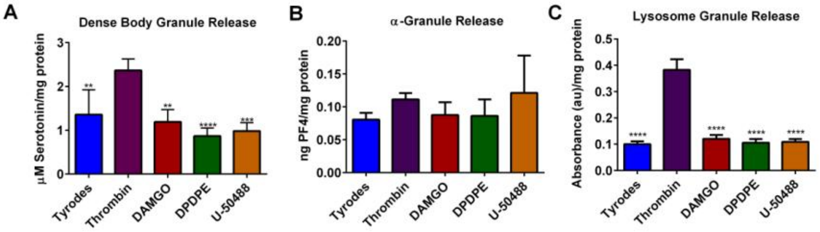

Figure 5.2 C57 platelet granule secretion upon opioid agonist stimulation. δ- granule secreted serotonin (A), α granule-secreted PF4 (B), and lysosome-secreted β-Hex (C) from C57 control mouse platelets after a 30 minute stimulation. All data is relative to the BCA-based protein content to normalize for variable platelet count. ** P≤0.01 *** P≤0.001 **** P≤0.0001 vs. thrombin condition

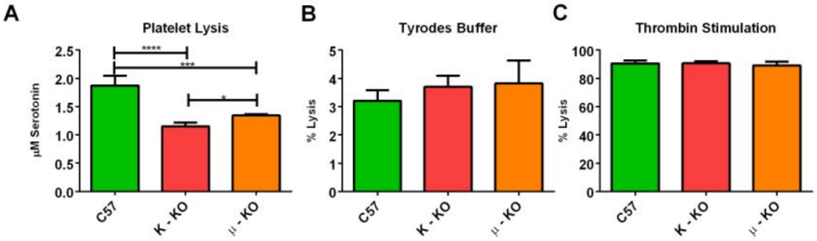

Figure 5.3 Knockout mouse serotonin concentration and secretion in response to thrombin. Initial experiments were performed to determine if the knockout platelets reacted differently from control platelets in control environments. The concentration of serotonin was measured after lysing the platelets with 0.5 µM $HClO_4$ (A), incubating them in a non-stimulant Tyrodes buffer(B), or stimulating them with the natural stimulant thrombin (C). The knockout mice showed significant changes in their total concentration of serotonin (A). However, the percentage of serotonin released in a resting state (B) and upon stimulation (C) was statistically indistinguishable for the knockout platelets compared to the control C57 mouse platelets. *P≤0.05 ***P≤.001 ****P≤0.0001 Vs. indicated position.

functioning normally). Comparing the percent of total serotonin secreted gives general insight into whether the biophysical characteristics of granule secretion may be affected by knocking out the opioid receptors. The control C57 mouse platelets were found to contain the greatest amount of serotonin, which was significantly higher than both K- (p≤0.0001) and µ- (p≤0.001) KO mouse platelets. µ-KO mouse platelets had slightly more serotonin than the K-KO mouse platelets (P≤0.05). Even with this difference in total serotonin content, platelets reacted similarly in Tyrodes buffer and with stimulation by thrombin, releasing similar percentages of their total serotonin content. Without doing single cell analysis, we cannot confirm that granule secretion, trafficking, and kinetics are the same, but the similar response on a bulk cell level helps support the fact that knocking out the receptors did not impact the platelets' ability to secrete granular content. Cholesterol concentrations in the platelets were also measured because cholesterol has been shown to play a role in granular secretion.[21,29,30] In this work, there was no significant difference in the amount of platelet cholesterol in the various strains of mice (data not shown).

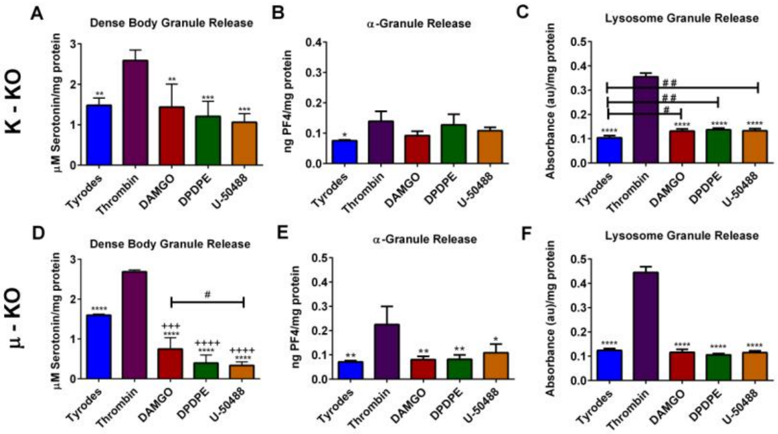

Figure 5.4 KO platelet granule secretion upon opioid agonist stimulation δ-granule-secreted serotonin (A)(D), α granule-secreted PF4 (B)(E), and lysosome-secreted β-Hex (C)(F) granule content release from K-knockout (A, B, C), and µ-knockout mice (D, E, F) platelets after a 30 minute thrombin stimulation. $*P\leq0.05$ $**$ $P\leq0.01$ $***$ $P\leq0.001$ $****$ $P\leq0.0001$ vs. thrombin condition $^{+++}$ $P\leq0.001$ $^{++++}$ $P\leq0.0001$ vs. Tyrodes condition and # $P\leq0.05$ ## $P\leq0.01$ vs. indicated conditions.

When the K- and µ-KO mice platelets (Fig. 5.4) were exposed to the same treatment as the C57 mice (Fig. 5.2), similar trends were seen and, in some cases, enhanced. For K- and µ-KO platelets, the agonists had a decreased change in average secretion of δ-granule contents (significantly different only for the µ-KO platelets $P\leq0.001$) compared to Tyrodes buffer (Fig. 5.4A and D). For the µ-KO platelets, the µ-agonist DAMGO still had a slight impact on δ-granule secretion. However, it significantly secreted over twice the amount of serotonin in the presence of U-50488 stimulation ($p\leq0.05$). This increased change in secretion of serotonin by DAMGO compared to the other agonists is still seen in the control and K-KO platelets, but to a lesser extent, suggesting that some µ-like receptors are still located on the cell surface (which was one hypothesis generated from the western blot data) or the agonist is interacting non-specifically with the platelet.

For alpha granule secretion (Fig. 5.4B and E), the differences in C57 PF4 secretion in the presence of U-50488 is continued in the K–KO and µ-KO platelets with an average increased difference of 0.03 ng PF4/mg protein in both samples compared to Tyrodes. The K-KO platelets average difference was 0.02 and 0.05 ng PF4/mg protein in secretion from DAMGO and DPDPE, respectively compared to Tyrodes. The lysosome secretion was no different between C-57 (Fig. 5.2C) and µ-KO platelets (Fig. 5.4F). However, in the lysosome secretion from the K-KO platelets, there was a significant ($p \leq 0.05$) increase (~0.03 ng PF4/mg protein) for all three agonists compared to Tyrodes buffer (Fig. 5.4C). These data suggest that there might be a role for the K receptor in hindering lysosome secretion when exposed to opioid, whereas the µ receptor could play a potential role in assisting in δ-granule secretion when exposed to opioids. To confirm this association, a more focused study is needed to determine if/how the receptors interact with the granules populations of interest. Finally, even though western blot analysis revealed that the K-receptor was not knocked out as expected, the U50488 K-agonist did not induce a difference in response compared to the other agonists and showed similar secretion trends compared to the C57 and µ-KO platelets. This suggests that the K-agonist is interacting with the same receptor as the other agonists or a receptor that has a similar pathway for granule secretion.

5.4.3 Platelet Adhesion Variations in Knockout Mouse Platelets

Another important component in hemostasis is the platelets' ability to adhere to both the endothelial cell wall and each other to form clots and prevent bleeding. Using a microfluidic channel coated with endothelial cells to mimic vasculature, platelets were flowed through the straight channel device after no stimulation (Tyrodes buffer) (Fig. 5.5A) or activation with ADP (Fig. 5.5B). The number of adherent KO platelets were counted and compared to the number of C57 platelets that adhered (Fig. 5.5). In non-activated platelets, only K-KO mouse platelets adhered significantly less than control platelets ($p \leq 0.05$). Even after activation with ADP, K-KO platelets still had decreased adhesion compared to both the µ - KO and C57 control platelets ($P \leq 0.05$ and $P \leq 0.01$, respectively). To further investigate possible reasons for the K - KO platelet decreased ability to adhere, both the rate of aggregation (Fig. 5.6) and activated platelet images (Fig. 5.7) were acquired.

5.4.4 Platelet Aggregation Variations in Knockout Mouse Platelets

Both aggregation behavior and morphological image analysis showed differences between the KO platelets and the control platelets. For aggregation experiments, the change in light transmission through 2 x 10^8 suspended platelets was measured after thrombin stimulation. Compared to control platelets, µ-KO platelets had a larger change in total transmission (Figure 6A) with a 25.1% change in transmission compared to 22.5% and 18.1% for K-KO and control platelets, respectively. This difference was statistically significant only between C57 and µ-KO platelets ($p \leq 0.05$). Surprisingly, though the overall change in aggregation behavior did not impact the rate of aggregation with both µ-KO and C57 platelets having a 1.1% change in transmission each second. On the other hand, the K-KO platelets took significantly longer to aggregate than both C57 ($p \leq 0.01$) and µ-KO platelets ($p \leq 0.05$) with a change of transmission of 0.82% per second. This slower aggregation could be one possible reason that fewer K-KO platelets adhered to the microfluidic device in the time frame and distance measured. Another factor that has the potential to impact adhesion behavior is activation shape.

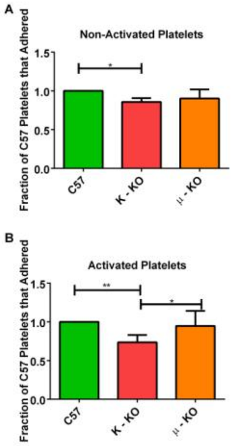

Figure 5.5 Measurement of platelet adhesion in a microfluidic channel coated with endothelial cells. Platelets were not activated (A) or activated with 5µM ADP (B), a natural platelet stimulant, before being flowed through the device. *P≤0.05 ** P≤0.01 **** vs. indicated position

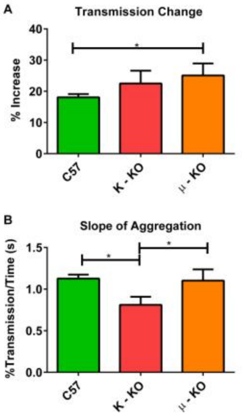

Figure 5.6: Platelet aggregation measurements upon 4.8 U/mL thrombin stimulation. The change in light transmission (A) and the rate of change were measured (B). *P≤0.05 vs. indicated position

5.4.5 Platelet Dark Field Imaging

Images of control (27 images, 2 different samples), K-KO (30 images, 2 different samples), and µ-KO (25 images, 2 different samples) platelets with a minimum of 20 platelets per image were visualized using dark field microscopy to characterize the platelet shape without need for a fluorescent label (Fig. 5.7). Neither the K- nor µ-KO platelets were able to scatter light as efficiently as the C57 platelets. Thus, to obtain an image of these KO activated platelets, exposure time was increased compared to the control platelets. The activation shapes of the different types of platelets were visually distinct. C57 platelets (Fig 5.7A) often showed two to three filopodia spread across the platelet while still maintaining a smaller circular center. The K-KO platelets displayed a more flattened look with a larger lamellipodia structure and small filopodia surrounding the entire platelet, giving the platelets a spiky appearance (Fig. 5.7B). Finally, µ-KO platelets were intermediate in appearance between the K-KO and C57 platelets. They contained distinct filopodia like the C57 platelets, but also contained a greater number of these features than C57 platelets and had a more spread out appearance (Fig. 5.7C).The platelets' ability to flatten out and form filopodia and lamellipodia affect how they adhere. When a platelet's shape flattens out, it enables the platelets to adhere more closely to the endothelial cell surface. The filopodia bind fibrin strands and the long extensions help interwine the platelets while forming a clot, whereas the lamellipodia bind to the wounded surface closing vasculature leaks.[31-33] An experiment performed by Stenberg et al. studied Wistar Furth rats whose platelets had hereditary macrothrombocytopenia. These platelets have previously demonstrated prolonged bleeding times and decreased adhesion. To further explore these phenomena, Stenberg et al. studied the shape change and formation of filopodia and lamellipoida and compared this shape change to normal rat platelets. They found that the Wistar Furth rats had few and short filopodia, but were still able to eventually go to the fully spread platelet stage. They also hypothesized that the limited filopodia formed more fragile clots which increased bleeding time.[32] Like the Wistar Furth rat platelets, the K-KO platelets also demonstrated these smaller filopodia, suggesting that the decrease in adhesion and increasesd aggregation time is likely due to the shape of the activated platelet.

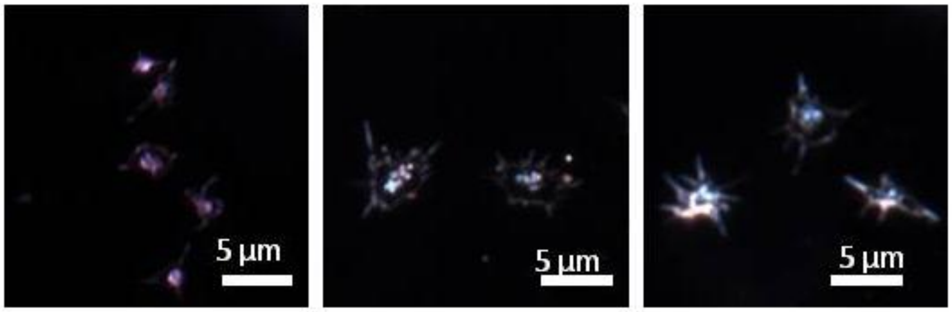

Figure 7 Representative activated platelet dark field scattering images for C57 control mice (A), K-KO mice (B), and µ-KO mice (C). Microscope image exposure time for the knockout mouse platelets was increased compared to the control mouse platelets due to lower scattering efficiency.

5.5 Conclusion

In conclusion, platelets contain opioid receptors; however, control platelets incubated with opioid receptor agonists do not degranulate in direct response to the opioid agonists, and the agonists do not affect platelet δ-granule secretion upon thrombin stimulation. When the receptors are knocked out, several unique features are seen, suggesting subtle roles for the opioid receptors. K-KO mouse platelets display decreased lysosome secretion upon opioid agonist exposure compared to the negative control. In addition, the K-KO platelets are not able to adhere as well, take longer to aggregate and have a more spread out appearance with less distinct filopodia than control platelets. The µ-KO mouse platelets had inhibited δ-granule secretion to a greater extent upon opioid agonist stimulation than both the K-KO and C57 platelets. There was also a difference in the final platelet shape which did not affect adhesion properties but had slightly enhanced aggregation. Medically, these data suggest that normal healthy platelet function will not be adversely affected when exposed to drugs containing opioids, including morphine and ketamine during surgery. However, one caveat is that these experiments do not mimic long-term platelet exposure to opioids nor does it account for how platelet behavior may change downstream of other cell types that are impacted by opioids.

Chapter 6: Platelets in Asthma: Platelet Response to Allergens, CXCL10, and CCL5

This work was completed with the assistance of Xiaojie Wu and Christy L. Haynes

6.1 Overview

Asthma is a chronic respiratory disease initiated by a variety of factors, including allergens. During an asthma attack, the secretion of C-X-C motif chemokine 10 (CXCL10) and chemokine ligand 5 (CCL5) cause the migration of immune cells, including neutrophils, mast cells, and platelets, into the lung and airways. Platelets, which contain three classes of chemical messenger-filled granules, can secrete vasodilators (serotonin, adenosine diphosphate (ADP), adenosine triphosphate (ATP), platelet activating factor (PAF)) and chemokines (CCL5, PAF4, C-X-C-motif chemokine 12 (CXCL12)), amplifying the asthma response. The goal of this work was three fold: 1) to understand if and how IgE affects platelet response to the common platelet activator thrombin associated with clotting and bleeding, therefore allowing us to compare platelet function between people without (no IgE) and with allergies or allergic asthma (IgE). It also gives a benchmark on whether any changes measured are due to IgE attachment or the allergic asthma related stimulants or a synergistic combination of the two; 2) to understand how allergen stimulation compares to thrombin stimulation; and 3) to monitor platelet response to the chemokines CXCL10, CCL5, and *N*-Formylmethionyl-leucyl-phenylalanin (fMLP). Herein, HPLC with electrochemical detection and/or carbon-fiber microelectrode amperometry were utilized to measure granular secretion events from platelets with and without IgE in the presence of an allergen, thrombin, CXCL10 or CCL5. Platelet adhesion and chemotaxis was measured using a microfluidic platform in the presence of the allergen TNP-Ova, CXCL10, or CCL5. Results from this study indicate that IgE binding changes δ-granule secretion in response to platelet stimulation by thrombin in bulk. Single cell results on platelets with exogenous IgE exposure show changes in membrane-granule fusion behavior during chemical messenger delivery events after thrombin stimulation. This change was further enhanced when IgE-incubated platelets were exposed to the allergen TNP-Ova. Extent of platelet chemical messenger secretion in the presence of TNP-Ova is comparable to the secretion levels induced by thrombin stimulation. In addition to secretion, TNP-Ova stimulation enhanced platelet adhesion to endothelial cells. Finally, only after incubation with IgE did platelets secrete chemical messengers in response to stimulation with the chemokines CXCL10, CCL5, or fMLP.

6.2 Introduction

In 2011, Asthma, a chronic respiratory disease affecting around 25 million people in the United States according to the CDC and the prevalence of asthma is rising. [1] Asthma is triggered by a variety of factors, including exercise, air temperature, stress, respiratory infections, and allergen presentation. During an asthma attack, smooth muscle cells contract to narrow the airways while epithelial cells initiate inflammatory processes through the secretion of chemokines, including CXCL10 and CCL5. CXCL10 and CCL5 help influence the movement of eosinophils, activated T-lymphocytes, macrophages, mast cells, and platelets into the lungs and lower airways including the airway smooth muscles and bronchial submucosa through the chemokine receptors CXCR3 and both CCR1 and CCR3, respectively.[2-9]

Allergic asthma is brought on by an allergen crosslinking IgE bound to cell surfaces through the Fcε receptors on a variety of immune cells including mast cells, eosinophils, neutrophils and platelets. Platelets, which have been shown to express both the high and low affinity IgE receptors, have recently garnered attention for their role in the enhancement of asthma symptoms.[9-11]

Platelets, a cell-like body commonly known for their role in hemostasis contain two main types of chemical messenger-filled granules (δ, α). The δ-granules contain small molecules including serotonin, adenosine diphosphate (ADP), adenosine triphosphate, Ca^{2+}, and histamine which enhance vasodilation and cell activation.[12] The α-granules contain a variety of growth factors, clotting factors, platelet factor 4, chemokines such as CCL5, and membrane adhesion molecules such as p-selectin.[13] Upon activation, platelets can secrete their granular contents through exocytosis, which is a highly conserved biological process where the granule docks to the cell membrane, forming a fusion pore between the granule contents and extracellular space. Upon fusion pore formation, part or all of the granular contents are secreted into the extracellular environment. In parallel, platelet shape change and adhesion to endothelial cells and leukocytes additionally enhance the asthmatic response. Platelet attachment to leukocytes allows for migration into the interstitium, and previous research has demonstrated that asthmatic patients show elevated levels of platelet-leukocyte complexes in the lungs.[14] The attachment to endothelial cells causes the secretion of additional chemokines by the endothelial cells, including IL-8, and the expression of the adhesion molecules ICAM on the endothelial cell surface.[15] Finally, exposure to thee adhesion molecule p-selectin on platelets helps to prime eosinophil adhesion to the endothelium and eosinophil migration.[16]

Platelets were first hypothesized to play a role in asthma in the early 1980s, [17] and since then have been shown to augment asthma symptoms through multiple pathways. Platelets with Fcε receptors have been found to migrate both in vitro towards the allergen they are sensitized to and in vivo from the vessels into the airways after an allergen challenge.[9] Platelets also have the ability to activate and secrete their granular contents within ten minutes of an allergic response.[18-

[21] The secretion of chemokines and vasodilators drives the recruitment of eosinophils, leukocytes, and T-helper 2 cells. The expression of p-selectin, CD154, and CD40 on activated platelets then assist with the platelet-cell interaction, activation, and endothelial cell wall migration of these cells.[15,16,19] Studies undertaken in platelet depletion models revealed a decrease in the progression of allergic asthma and reduced airway hyperresponsiveness, suggesting an important role for platelets and new therapeutic routes.[14,19,21,22]

Patient and animal models with allergic asthma present elevated levels of IgE in serum, often increasing with severity of the asthma.[23,24] Platelets exposed to increasing concentrations of serum IgE correlated significantly with platelet abnormalities, including changes in aggregation, and response to strong and weak agonists when compared to control platelets.[25,26] Platelet count was also decreased in patients with persistant asthma compared to healthy patients.[27] In this study, we further explore the role of IgE on platelet response to thrombin, a natural platelet activator, using electrochemistry to monitor serotonin secretion from the δ-granules on both bulk (HPLC with electrochemistry) and single cell (carbon-fiber microelectrode amperometry (CFMA)) levels.

In addition to measuring the effects of IgE on platelet function, the platelet response to allergens and the chemokines, CXCL10, CCL5, and *N*-formylmethionyl-leucyl-phenylalanine (fMLP), was monitored to determine if they can affect platelet secretion. CXCL10 and CCL5 are chemokines known to induce both chemotaxis and activation of mast cells on a bulk and single cell level in the context of asthma and other inflammatory conditions. [2, 28] In contrast, fMLP is a bacteria-derived chemokine that is not associated with asthma, but has been shown to cause platelet chemotaxis and was used as a positive control to assess the microfluidic chemotaxis measurements.[29] To the best of our knowledge, stimulation of platelets by these chemokines has not been probed. The platelets adherence to endothelial cells in a microfluidic device after stimulation in response to these chemokines and TNP-Ova will be discussed due to their role in activating endothelial cells and assisting in migration of leukocyte-platelet complexes into the lung during an asthma attack as discussed above.[14-16] Due to the preliminary nature of this work, the discussion will identify trends seen in the data even when not statistically significant. Ongoing experimental replicates will allow conclusions with more statistical power.

The results presented herein show that IgE-exposed platelet secretion changes with the incubation of IgE on a bulk cell level when responding to thrombin, a natural platelet stimulant. A biophysical change in the character of the membrane-granule fusion behavior during the chemical messenger delivery events was detected. Upon allergen (TNP-Ova) exposure, the membrane-granule fusion pore behavior change was enhanced, and the rate of serotonin secretion was highly variable compared to thrombin stimulation of IgE-incubated platelets. In these data, platelets secrete their δ-granule contents in response to the chosen chemokines only after incubation with IgE. Finally, of the conditions conditions considered, only activation by allergens increased platelet adhesion significantly compared to the negative control.

6.3 Experimental Approach

6.3.1 Reagents

CXCL10 and CCL5 were purchased from Shenandoah Biotechnology, and fMLP was purchased from Sigma Aldrich. Stock powder was diluted into Tyrodes buffer (NaCl, 137 mM; KCl, 2.6 mM; $MgCl_2$, 1.0mM; D-glucose, 5.6 mM; N-2-hydroxyethylpiperazine- N'-2-ethanesulfonic acid (HEPES) 5.0 mM; and 12.1 mM $NaHCO_3$, with pH adjusted to 7.3) at a final concentration of 100 μg/mL. CXCL10 and CCL5 were stored at -80 ^oC, and fMLP was stored at -20 ^oC. Anti-trinitrophenol (TNP) IgE and TNP-Ova were purchased from BD Biosciences and Fischer Scientific, respectively. The TNP-Ova was diluted in Tyrodes buffer before storage at -80 ^oC. All other reagents were purchased from Sigma Aldrich and used as received.

6.3.2 Platelet Preparation

Blood was drawn via cardiac stick from male C57BL/6J mice (Jackson Laboratories) following IACUC protocol #1403-31383A. After CO_2 euthanasia, blood was drawn into syringes filled with 200 μL ACD (2 g citric acid, 5.6 g sodium citrate, 5 g glucose, and 250 mL Milli-Q water pH ~5.1).The blood was diluted with Tyrodes buffer, and centrifuged at 130 xg for 10 minutes with brake level 2. The resultant platelet-rich plasma was put into 1.7 mL eppendorf tubes with 200 μL ACD and Tyrodes buffer before centrifugation at 524 xg for 10 minutes with brake level 2. The pellet was then re-suspended in Tyrodes buffer.

6.3.3 Bulk Serotonin Analysis

For each sample, 125 μL of platelet suspension at 4×10^7 platelets/mL were incubated in either 125 μL of Tyrodes buffer or 1 μg/mL IgE in Tyrodes buffer for two hours at 37^oC. 20 μL ACD was added to each vial, and samples were washed at 800 xg for 5 minutes. The platelets were resuspended in 125 μL Tyrodes buffer and 125 μL of stimulant for a 45 minute stimulation. The final concentration of each stimulant was 100 ng/mL for CXCL10, CCL5, fMLP, and TNP-

Ova, 1 unit/mL thrombin, Tyrodes buffer (negative control), or 0.25 μM $HClO_4$ (lysis). All conditions had 5 biological replicates.

The supernatant was filtered in a 96 well Millipore Multi Screen 0.45 μm filter plate at 3000 xg for 5 min. 180 μL of supernatant was added to 20 μL of 5 μM dopamine internal standard in an HPLC vial. The sample was separated following a previously published protocol [28] using a 5 μm, 4.6 mm × 150 mm Eclipse XDB C18 column on an Agilent 1200 HPLC with a Waters 2465 electrochemical detector. The serotonin was detected with a Waters glassy carbon electrode set at a potential of 700 mV vs. Ag/AgCl. The mobile phase run at 2 mL/min, consisted of 11.6 mg/L of the surfactant sodium octyl sulfate, 170 μL/L dibutylamine, 55.8 mg/L Na_2EDTA, 10% methanol, 203 mg/L sodium acetate anhydrous, 0.1 M citric acid, and 120 mg/L sodium chloride.

In addition, a calibration curve was run with serotonin concentrations ranging from 0.0625 μM to 1 μM. The area underneath the serotonin spike and a dopamine internal standard spike was measured, and the ratio of serotonin to dopamine was recorded.

6.3.4 Carbon-Fiber Microelectrode Fabrication

Microelectrodes were fabricated as previously described.[30] Briefly, carbon-fibers were aspirated through glass capillaries and then halved with a pipette puller. After trimming the carbon-fibers, the electrodes were epoxied using Epon Resin 828 (Miller-Stephenson) and metaphenylene diamine hardener, and finally cured at 25, 100 and 150°C overnight, for 4-16 hours, and then for 2-6 hours, respectively. Before the experiment, the microelectrodes were beveled at 45° with a diamond-coated polishing wheel and placed into isopropyl alcohol until needed.

Glass micropipette puffers for stimulant delivery were made the day of the experiment. Glass capillaries were halved with a pipette puller, and the tips were trimmed to form an opening of 10-50-μm-diameter.

6.3.5 Carbon-Fiber Microelectrode Experiments and Data Analysis

Amperometry experiments were performed using an Axopatch 200B potentiostat (Molecular Devices) with a 5 kHz low-pass Bessel filter, 20 mv/pA output gain, and 20 kHz collection rate. LabVIEW Tar Heel CV software (National Instruments) written by Michael L.A.V. Heien controlled computer interface settings and data acquisition.

The platelet suspension was prepared as described above, and a final concentration of $2x10^7$platelets was incubated with 0.5 μg/mL IgE or Tyrodes buffer for 2 hours and washed at

800 xg for 5 minutes. A couple μL of platelet suspension was pipetted onto a poly-L-lysine-coated cover slip and monitored with an inverted microscope equipped with phase contrast optics at 40x magnification (Nikon Instruments). Before measuring, the puffer (containing either 10 units/mL thrombin or 100 ng/mL TNP-Ova) and electrode were placed near and on top of the platelet, respectively, using Burleigh PCS-5000 piezoelectric micromanipulators (Olympus America). The potentiostat was set to 700 mV vs. Ag/AgCl reference electrode. A picospritzer was used to puff a 3 second bolus of stimulant onto individual platelets, and the current was measured over a 90 second period. Each trace was filtered at 500 Hz and then converted to the correct file type with ABF Utility. The spikes were analyzed in Mini Analysis software written by Justin Lee (Synaptosoft).

The number of spikes or individual granule secretion events in each trace (N) reveals the platelet's ability to traffic granules to the cell membrane and achieve fusion. By analyzing each individual spike, membrane fusion pore stability and chemical messenger secretion kinetics can

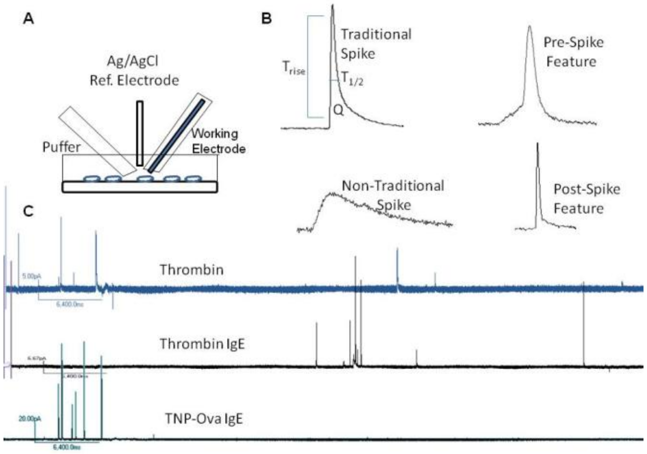

Figure 6.1 Carbon-fiber microelectrode amperometry and example traces. Carbon-fiber microelectrode amperometry electrodes and puffer setup (A) with platelets on a coverglass coated with poly-L-lysine. After stimulation, the change in current for each granule secretion event is seen as a spike. Upon inspection of the spike, several biophysical parameters can be obtained including $T_{rise,}$ $T_{1/2,}$ the slope of the rise (10/90 slope), and the area underneath the spike (Q) which is associated with the molecules of serotonin secreted. The fusion pore stability can be observed by looking at the number of events with pre-, post-, and non-traditional spike features. (B) Finally, the number of granule secretion events per each trace can be counted. A representative trace from each condition is shown. (C)

be observed (Fig. 6.1 A and B). The integrated area underneath each time versus current spike reveals the charge (Q), which is translated to the number of serotonin molecules secreted from that granule using Faraday's law. T_{rise}, the time it takes for the current spike to rise from 10 to 90% of its amplitude, and the 10/90 slope, the change in current over time from 10 to 90% of the total current amplitude, give insight into the opening of the fusion pore. $T_{1/2}$ is the length of time of the full width at half maximum current amplitude and gives insight into how long the fusion event is allowing serotonin secretion. Finally, the presence of non-traditional current events, pre- or post-spike feet features, give indications about the stability of the dynamic fusion pore. More information on these features can be found in the following reference and chapter 2. [31] Current spikes classified as non-traditional events typically had hump-like features and did not follow the traditional quick rise and exponential decay. Pre-spike features included plateaus, ramps, and small spikes in current before the main spike. Typically, post-spike features indicate the granule re-opening causing another current spike or a continuous serotonin flux out of the granule after the initial spike. In this work, the number of traces analyzed for thrombin stimulation only experiments without and with IgE were 23 and 19 amperometric traces, respectively. For the thrombin vs. TNP-Ova conditions, 20 and 32 traces were analyzed, respectively.

6.3.6 Adhesion

Straight channel microfluidic devices were made as previously described. [32, 33] Briefly, the microfluidic channels were fabricated using standard photolithography techniques. The channel patterns were transferred onto the negative photoresist coated-silicon wafer via UV exposure. Polydimethylsiloxane (PDMS) was poured on the silicon wafer and cured overnight before permanent attachment to a glass coverslip. The final dimensions of each channel were 1.5 cm (L) x 100 μm (H) x 1 mm (W). Each device contained 4 channels for parallel adhesion experiments.

To coat the device with human endothelial cells (hy926, ATCC), 2.5 mg/mL human fibronectin (Invitrogen) was incubated in the channel for an hour before endothelial cell injection. Then, an endothelial cell suspension (~60 μL) with the desired cell density ($5\text{-}6 \times 10^6$ cells/mL) was injected into the channel for surface coating. After 2 hours, the media was exchanged to remove any non-adherent cells. The cells in the device were fed with fresh media every day for 3 to 5 days.

On the day of experiments, platelets (4×10^7 platelets/mL) were incubated with 0.5 μM IgE for 2 hours and washed at 800 xg for 5 min after the addition of ADC. The pellet was suspended in 2 mL Tyrodes buffer for a final concentration of $\sim 2 \times 10^7$ platelets/mL. Next, the platelets were incubated with 2 μM 5-chloromethylfluorescein diacetate (CMFDA) dye for 20 minutes at 37 °C with minimal exposure to light before washing at 800 xg and re-suspending in Tyrodes. Finally, 500 μL of platelet suspension was spiked with 0.5 μg/mL TNP-Ova, CXCL10, or CCL5 at a final concentration of 100 ng/mL. Control platelets were kept in Tyrodes buffer. Immediately following exposure to the stimulant, the platelets were flowed through the device at 60 μL/hour for 30 minutes. The device was then washed with Tyrodes buffer at the same rate for 15 minutes to remove unadhered or loosely adherent platelets. Five random 204.8 μm x 204.8 μm areas of each channel were imaged using a Nikon Microscope with a 40x oil immersion objective and a QuantEM Photometrics CCD camera. Metamorph version 7.7.5 image analysis program was used to count the number of platelets adhered in each channel based on the fluorescence signal. The platelet count was compared to the control channel in the same device. 4 devices with 4 channels in each device were used to monitor platelet adhesion giving a total of 4 analytical replicates per condition.

6.3.7 Platelet Chemotaxis

Two adhesion devices were used to monitor chemotaxis. Both microfluidic platforms (Fig. 6.2) were molded and fabricated as previously described.[34] For the gradient device (Fig. 6.2A), 2.5 mg/mL human fibronectin (Invitrogen) was injected into the channel for 1 h to coat the surface before endothelial cell addition. Then, an endothelial cell suspension (20 μL) with the desired cell density (4-5 × 10^6 cells/mL) was introduced into the cell inlet for channel coating. The cells in the device were fed with fresh media every day for 3 to 5 days. To form a chemical gradient, 100 ng/mL fMLP and Tyrodes buffer were injected through left and right inlets, respectively, at a flow rate of 100 μL/h for 30 min.

For the gel device (Fig. 6.2B), the gel chamber was injected with 30 μL of 1 mg/mL poly-D-lysine (PDL) solution and incubated at 37°C for a minimum of four hours before washing with Milli-Q water and putting into the oven at 65 °C for 24-48 hours. After cooling, the gel device chambers were filled with 2 mg/mL Collagen type I gel solution (BD Biosciences) while being kept in a humid pipette box for 40 minutes at 37 °C with 5% CO_2. After gel polymerization, 20 μL of DMEM medium was introduced into each side channel, and the four reservoirs were aspirated before 10 μL endothelial cell suspension was added into one side channel at a density between 8 and 10 × 10^5 cells/mL. All non-adherent cells were washed out with fresh media after 30 min initial incubation, and then the devices were placed in the incubator overnight at 37 °C with 5% CO_2, and a confluent endothelial layer was observed on the side wall of the gel. Before platelet addition, 50 ng/mL fMLP solution was added into the side channel without endothelial cells while Tyrodes buffer was added into the other side channel to create a gradient across the gel chamber. The formation of stable chemical gradients takes 2 h according to the molecular diffusion simulation results.[33]

Platelets, IgE, and CMFDA dye incubation were done as previously described in the adhesion studies. After incubation, platelets were either activated with 5 μM ADP or 100 ng/mL TNP-Ova or not activated before injection into the bottom cell chamber of gradient device and endothelial cell side channel of the gel device, respectively. The fluorescently labeled platelets were imaged on a Nikon Microscope with a 40x oil immersion objective with a QuantEM Photometrics CCD camera. The Metamorph version 7.7.5 image analysis program was used to track platelet movement in the gradient device and count the number of platelets that moved into the gel. In the gradient device, single cell movement was monitored for 30 min with images recorded every 20 seconds. In contrast, the gel device was imaged every other hour for 5 hours.

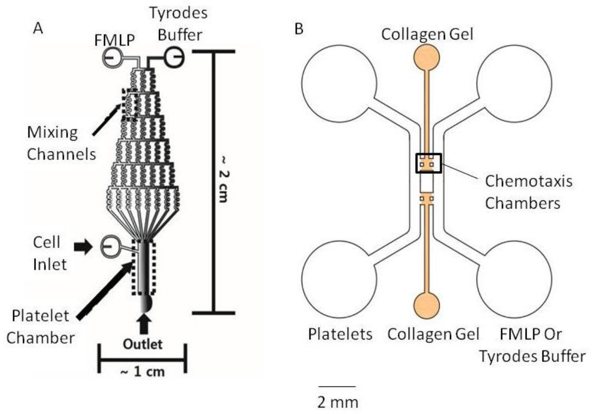

Figure 6.2 Chemotaxis devices. Gradient (A) and gel (B) microfluidic devices used to monitor platelet chemotaxis. To understand chemotaxis, cell motion in the gradient device was monitored, while cell count in the chemotaxis chamber of the gel device was used to characterize platelet infiltration

6.3.8 Data Analysis

All graphs were made and analyzed in Graphpad Prism 6, and the error bars represent the standard error of the mean. Statistical differences were tested using one-way ANOVA. Any outliers in the bulk analysis were q-tested out with 95% confidence. For CFMA, traces with only one granule secretion event were also removed from statistical analysis.

6.4 Results and Discussion

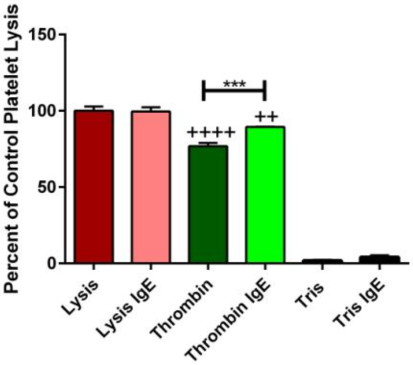

Figure 6.3 Serotonin secretion of platelets with and without IgE in response to thrombin. Percent of total serotonin release from platelets after incubation with or without IgE and then stimulation with $HClO_4$ (lysis) or thrombin (natural platelet stimulant). ++ $p \leq 0.01$ and ++++ $p \leq 0.0001$ vs. both lysis conditions ***$p \leq 0.001$ vs. indicated position.

6.4.1 Thrombin Response after IgE incubation

Bulk platelet serotonin secretion from δ-body granules in response to 1 units/mL thrombin or 0.5 μM $HClO_4$ (lysis condition) was monitored after incubation with 0.5 μg/mL IgE in Tyrodes buffer or Tyrodes buffer alone (Fig. 6.3). The amount of serotonin secreted during IgE incubation was measured, and no difference was noted between platelets incubated with Tyrodes buffer or Tyrodes buffer with IgE (data not shown), suggesting that IgE incubation does not cause platelet activation. In addition, the total platelet serotonin content, determined by cell lysis, did not significantly change after incubation with IgE. When stimulated with thrombin, a strong platelet activator associated with clotting and bleeding, both thrombin conditions secreted less serotonin than both lysis conditions ($p \leq 0.01$ for IgE-incubated platelets and $p \leq 0.0001$ for non-IgE incubated platelets). Between the thrombin conditions, IgE incubated platelets secreted significantly more serotonin than non-IgE incubated platelets ($p \leq 0.001$). This difference suggests that IgE incubation is causing variations in granular secretion, since platelet populations and stimulation are similar.

To investigate these differences, the fusion pore stability and chemical messenger secretion kinetics during the granule-membrane interaction, as well as the platelets' ability to traffic granules to the platelet membrane, were monitored using CFMA. Representative traces for thrombin stimulation can be seen in Fig. 6.1C. Unlike the bulk cell secretion measurements, the total amount of serotonin secreted by individual platelets and the amount secreted per granule were not significantly different when measured with and without IgE incubation (Fig. 6.4A and B). However, it is clear that the average amount of serotonin secretion per platelet after incubation with IgE is more likely the cause of the increased serotonin secretion in the bulk rather than the number of granules being secreted, which did not change between the platelets incubated with and without IgE (Fig. 6.4C). This is reasonable considering that IgE is interacting with the membrane and should not impact the ability for the platelet to transport granules to the membrane surface. The fusion pore kinetics was also not significantly different (Fig. 6.4 D and E). The slight variations suggest there may be small differences in the membrane-granule interaction, but nothing that impacts the net chemical messenger secretion. Finally, the stability of the granule-membrane fusion pore was analyzed by counting the number of spike feature variations often termed feet or non-traditional events as described in Chapter 2 (Fig. 6.1 B and Fig. 6.4F)The number of post-spike feet increased in IgE-incubated platelets compared to non-incubated platelets from 10.1% to 28.5% ($p \leq 0.05$). The percent of post spike feet for the control in this experiment was unusually high considering that post-spike feet are the least common type of spike feature, often seen around 2-4% of the time in PC12 cells and platelets.[31,35] However, the 282 % increase is still a large increase considering that in previous research from our lab, a 31% increase of cholesterol in platelets, which helps with inhibiting both opening and closing of the fusion pore, only caused ~155% increase in post-spike feet features.[31, 36] It was also noticed that both pre- and post-spike feet features would occur in the same spike with an occurrence of 9.5% in platelets incubated with IgE vs. only 1.1% of the time in control platelets. This co-occurrence suggests that the change in membrane in the presence of IgE hinders the ability for the lipids to transition between positive and negative curvatures smoothly to open and close the fusion pore.

Overall, these data suggest that IgE can affect the platelet's ability to secrete δ-granule contents in response to thrombin on a bulk cell level and single cell results show an average increase in secretion from individual granules. This increase might be caused by changes in the opening and closing of the granule's fusion pore that varies with IgE incubation.

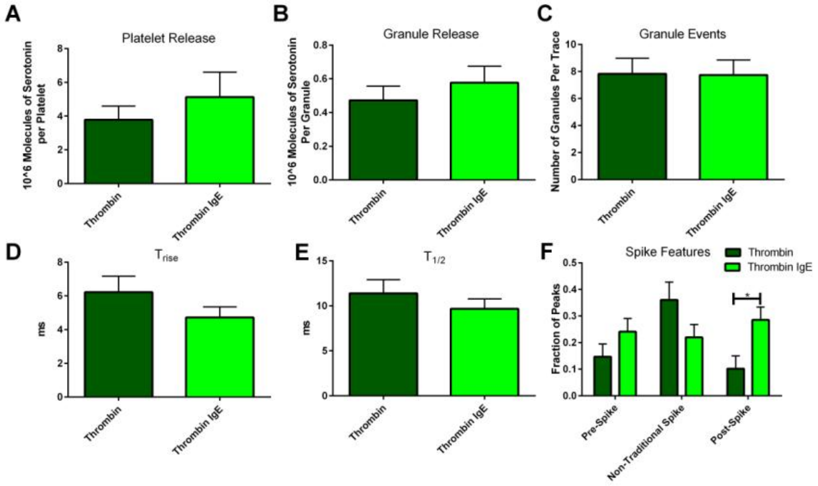

Figure 6.4 Carbon-fiber microelectrode amperometry data for platelets stimulated with thrombin: Single cell comparison of thrombin stimulation after platelets were incubated without or with IgE. The total amount of serotonin secreted per platelet (A) was calculated using the amount of serotonin secretion per granule (B) and number of granule release events (C). Platelets incubated with IgE demonstrated an average decrease in fusion pore opening time (D) and decreased release time (E). The only statistically significant difference was the number of post-spike foot features (F). This accumulated data suggests that the IgE may have a small impact on the fusion pore's ability to appropriately open and close, but this does not impact platelets' δ-granule response to thrombin.

6.4.2 Platelet Response to Allergens

Platelet response to allergens has already been established. [18-21] However, the amount of response relative to thrombin, a strong platelet activator, has not been explored. This information will give a basis for benchmarking how strong of an activator the allergen is compared to the common clotting stimulant thrombin. In preliminary bulk cell studies (Fig. 6.5), as expected, platelet secretion was stimulated by TNP-Ova only after exposure to IgE. The total amount of

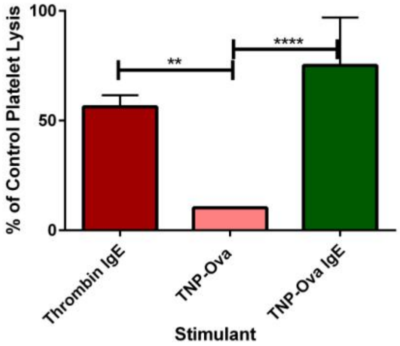

Figure 6.5 Preliminary platelet δ-granule bulk response to thrombin and TNP-Ova stimulation after incubation with IgE. **$p \leq 0.01$ **** $p \leq 0.0001$ vs. indicated conditions

serotonin secreted (75.1% of the control platelet lysis concentration) was comparable to the response seen from thrombin. On a single cell level, platelets and individual granules also secreted the same amount of serotonin in response to stimulation with thrombin and TNP-Ova. (Fig. 6.6 A,B) In addition, no differences were noted in their ability to traffic granules (Fig. 6.6C). This amount of secretion from allergen stimulation further supports the platelets' role in inflammation processes.

The fusion pore kinetics (T_{rise} and $T_{1/2}$) did not significantly change when comparing thrombin and TNP-Ova stimulation (Fig. 6.7A, B). However, many of the amperometric traces were characterized by higher amplitude spikes that generally had steep slopes upon TNP-Ova stimulation, suggesting that the flux of serotonin was more rapid when compared to thrombin stimulation. $T_{1/2}$ values could not capture the fact that these spikes were reaching higher amplitudes since the time was not significantly different than that seen by thrombin. To explore

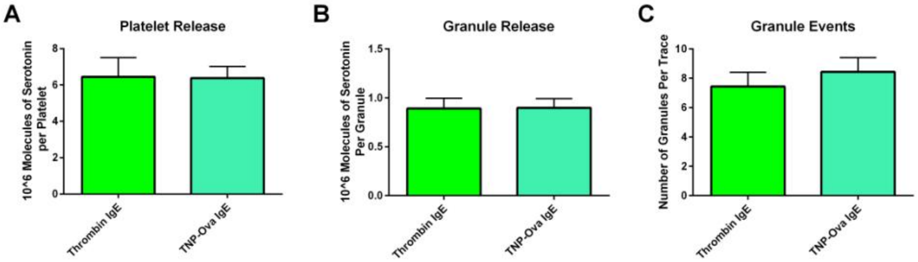

Figure 6.6 Platelet δ-granule response to thrombin and TNP-Ova stimulation after incubation with IgE. No statistical difference was noted in the total amount of serotonin released per platelet (A), or granule (B). The number of granule fusion events also stayed the same (C).

this, the slope from 10 to 90% of the spike amplitude was measured. (Fig. 6.7 C). No significant difference was noticed when all the individual spike values were averaged, but a histogram of the 10/90 slope values show a large spread for stimulation with TNP-Ova compared to thrombin stimulation. All the thrombin conditions had 10/90 slopes at 55 pA/ms or under with 95% of spikes being in the first bin. By contrast, only 64% of TNP-Ova stimulated event values fell into the first bins (Fig. 6.7 D). The quick thrombin induced secretion events often displayed a post-spike foot feature, typically as seen in Fig. 6.1B. This slope contributed to the significant rise in post spike feet features compared to thrombin stimulation from platelets incubated with IgE. (Fig. 6.7 E)

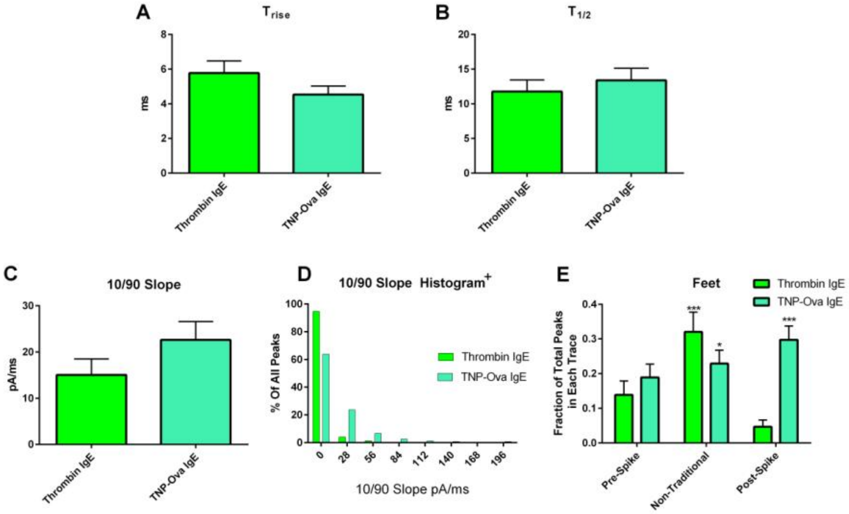

Figure 6.7 Granule fusion pore dynamics upon thrombin and TNP-Ova stimulation. Granule fusion pore kinetics were not changed between stimulation with thrombin and TNP-Ova on IgE-incubated platelets (A,B). TNP-Ova stimulation’s 10/90 slope for each spike showed a slight average increase, indicating that serotonin was released faster from the granule in many cases (C). The histogram of 10/90 slopes shows that TNP-Ova had a greater spread of 10/90 slopes compared to thrombin-stimulated platelets (D). The increased 10/90 slopes often came with post-spike features, which played a role in the significant increase in post spike foot features for allergen stimulation compared to thrombin (E).

$^{+}$2 data points at 410 and 580 pA/ms for TNP-Ova stimulation are hidden *p≤0.05 and ***p≤0.001 vs. thrombin IgE stimulation post spike feet features.

The exact signaling cascade for TNP-Ova stimulation in platelets is not fully known, to the best of our knowledge. However, these data suggest that platelets respond similarly to allergens as to the strong stimulant thrombin in terms of granule trafficking and total serotonin secretion. The ability for allergens to stimulate platelets to the same extent as thrombin indicates that platelets have the potential to play a large role in inflammation processes by the secretion of their granular contents, including vasodilators (ADP, ATP, PAF and serotonin) and chemokines (PAF, CCL5, and CXCL10). However, examination of the individual granule secretion events suggest that there is a wide spread in how fast the serotonin is secreted from the granule and that the stability of fusion pore closure is compromised when exposed to allergens compared to thrombin stimulation of IgE-incubated platelets.

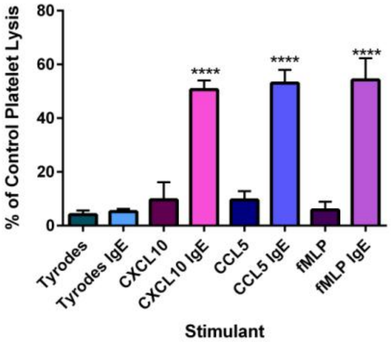

Figure 6.8 Secretion of serotonin in response to CXCL10, CCL5, and fMLP on platelets incubated without and with IgE incubation. All platelets activated with IgE showed significant secretion compared to the negative control. ****P≤0.0001 vs. both Tyrodes conditions and all non IgE incubated platelets exposed to the chemoattractants.

6.4.3 Platelet Response to CXCL10, CCL5, and fMLP

CXCL10, CCL5, and fMLP are known for their involvement in chemotaxis, but not cell exocytosis. However, previous research on mast cells discussed in Chapter 7, have shown that mast cells secrete their granular contents in response to CXCL10 and CCL5.[28] To understand if platelets will respond similarly, platelet secretion was measured after exposure to CXCL10, CCL5, and fMLP for 45 minutes. Only IgE-incubated platelets had significant serotonin secretion compared to the negative control (Tyrodes buffer) (Fig. 6.8). This secretion was significantly different than the negative control (Tyrodes buffer) with and without IgE incubation and all chemoattractant stimulation of platelets without IgE ($p \leq 0.0001$). Further experiments must be performed to understand how these chemoattractants affect granule kinetics and fusion pore stability in platelets at the single cell level.

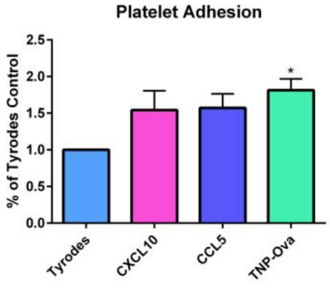

Figure 6.9 Platelet adhesion in response to CXCL10, CCL5, and TNP-Ova. Platelets were stimulated with CXCL10, CCL5, or TNP-Ova before introduction into a microfluidic straight channel device lined with endothelial cells. The number of adherent platelets were counted and compared to the non-stimulated platelets in each device. *$P \leq 0.05$ vs. Tyrodes control condition

6.4.4 Platelet Adhesion

In addition to secretion, the ability for platelets to adhere is important for enhancing the allergic reaction by allowing infiltration of leukocytes and eosinophil into the lung tissue. In addition, attachment of platelets to endothelial cells is known to cause endothelial cells to express ICAM and secrete the chemoattractant IL8.[14-16] IgE-incubated platelets stimulated with CXCL10, CCL5, or TNP-Ova were flowed over a straight microfluidic channel, and the number of platelets that adhered to an endothelial cell layer were counted and compared to non-stimulated platelets. In total 4 analytical replicates were run with 5 images taken along each channel. The control platelets on each device had between 22-40 platelets that adhered with an average of 33 platelets. Platelet adhesion was only significantly increased when the platelets were exposed to the allergen TNP-Ova.

6.4.5 Platelet Chemotaxis

Finally, the ability of platelets to infiltrate the lung can play a large role in enhancing inflammation. Previous literature has demonstrated the ability for platelets to move in response to fMLP at ~ 43.7ng/mL.[29] Initial experiments were performed with 100 ng/mL fMLP to act as a positive control within this simple microfluidic device that was initially created to monitor neutrophil chemotaxis and angiogenesis.[33,34] The aim of this experiment was to determine if platelets follow a chemoattractant gradient and to see if they are able to move through or on an endothelial cell wall, mimicking movement into the lung. In this set of experiments, no platelet movement was detected in response to fMLP, the positive control, in either device under various conditions including IgE-incubated platelets activated by 5 μm ADP, 100 ng/mL TNP-Ova or no activation (data not shown). Therefore, CXCL10 and CCL5 experiments were not performed. Two potential reasons that these experiments may not have worked, include that the endothelial cells may not be expressing the adhesion molecules that are needed for chemotaxis and both devices had flow rates that might have prevented the adhesion and chemotaxis of the platelets.

6.5 Conclusion

The aim of this paper was to gain more in-depth information on the role of platelets in asthma by looking at the interaction with the chemoattractants CXCL10 and CCL5 known to be secreted during an asthma attack, the response to allergens that can trigger asthma, and the effects of IgE on platelet function. Results show that platelet incubation with IgE changes the platelet’s ability to respond to the strong platelet stimulant thrombin. In addition, the membrane fusion pore dynamics change after exposure to IgE. This change in membrane fusion pore dynamics, particularly the increase in post spike feet, was enhanced by stimulating the platelets with TNP-Ova. The post spike-foot increase was partially due to a larger number of spikes, which are characterized by the quick release of large amounts of serotonin, and can be quantified using 10/90 slope. The large 10/90 slope secretion events typically have ramp-like post-spike features indicating that there may be variations in the membrane around the granule fusion pore which inhibit or enhance the closing between platelets stimulated with TNP-Ova or thrombin . TNP-Ova stimulation caused serotonin secretion that is comparable to thrombin stimulation, suggesting that platelets have the ability to play a large role in amplifying asthma, making them a potential therapeutic target. Platelets were also able to adhere to endothelial cells upon stimulation with TNP-Ova which may allow for increased infiltration of immune cells into the lungs.

In preliminary experiments, the chemoattractants CXCL10, CCL5, and fMLP showed platelet stimulation only after incubation with IgE. Previous studies have demonstrated that, when exposed to IgE, platelets up-regulate CD154 which helps with the allergen response.[19] A similar mechanism may be responsible for the platelets ability to respond to chemoattractants only after

IgE incubation. The platelet response to the chemoattractants was not as strong as the platelet response to TNP-Ova. Finally, even though previous studies have demonstrated platelet chemotaxis in response to fMLP, we were not able to verify this with our preliminary work in microfluidic models.

Chapter 7: Time- and Concentration-Dependent Effects of Exogenous Serotonin and Inflammatory Cytokines on Mast Cell Function

Adapted with permission from Sarah M. Gruba[‡], Audrey F. Meyer[‡], Benjamin M. Manning, Yiwen Wang, John W. Thompson, Joseph J. Dalluge, and Christy L. Haynes. Time- and Concentration-Dependent Effects of Exogenous Serotonin and Inflammatory Cytokines on Mast Cell Function. *ACS Chem Biol*, 9, 503-509. Copyright 2014 American Chemical Society

[‡] Authors contributed equally

This manuscript was also included in Audrey F. Meyer's thesis

7.1 Overview

Mast cells play a significant role in both the innate and adaptive immune response; however, the tissue-bound nature of mast cells presents an experimental roadblock to performing physiologically relevant mast cell experiments. In this work, a heterogeneous cell culture containing primary culture murine peritoneal mast cells (MPMCs) was studied to characterize the time-dependence of mast cell response to allergen stimulation, and the time- and concentration-dependence of the ability of the heterogeneous MPMC culture to uptake and degranulate exogenous serotonin using high performance liquid chromatography (HPLC) coupled to an electrochemical detector. Additionally, because mast cells play a central role in asthma, MPMCs were exposed to CXCL10 and CCL5, two important asthma-related inflammatory cytokines that have recently been shown to induce mast cell degranulation. MPMC response to both allergen exposure and cytokine exposure was evaluated for 5-HT secretion and bioactive lipid formation using ultraperformance liquid chromatography coupled to an electrospray ionization triple quadrupole mass spectrometer (UPLC-MS/MS). In this work, MPMC response was shown to be highly regulated and responsive to subtle alterations in a complex environment through time and concentration dependent degranulation and bioactive lipid formation. These results highlight the importance of selecting an appropriate mast cell model when studying mast cell involvement in allergic response and inflammation

7.2 Introduction

Mast cells are tissue-bound cells of hematopoetic origin widely known for their roles in inflammation and allergic response. They also have roles in innate immunity, host defense against parasitic and bacterial infection, wound healing, tissue homeostasis, and disease states such as vasculitis and fibrosis.[1-3] Mast cell function is often thought to be dominated by their cytosolic granules that contain inflammatory mediators, including enzymes such as tryptase and chymase, highly charged biopolymers such as heparin or chondroitin sulfate, and small molecule messengers such as serotonin (5-hydroxytryptamine, 5-HT) and histamine. In addition to granule-stored mediators, mast cells produce and secrete bioactive lipid compounds via enzymatic transformations of their phospholipid membranes. In vivo mast cell secretion of both granule-stored and de novo manufactured inflammatory mediators influence surrounding cell types, leading to symptoms commonly associated with allergic response, including mucus hypersecretion, bronchoconstriction, and vasodilation.[4, 5] Based on their significant involvement in both innate and adaptive immune response, there are many research groups that aim to study mast cell behavior; however, there are several experimental roadblocks to performing physiologically relevant mast cell experiments.

Mature mast cells are tissue bound, and as such, it is difficult to isolate large numbers of pure populations for study; due to this challenge, several different in vitro strategies for mast cell culture are commonly used in experimental work. Isolation of pure populations of mast cells typically requires tissue homogenization followed by several immunomagnetic separation steps, which can affect the activation state of the mast cells and gives low cell yields. To circumvent this challenge, studies of mast cells are often performed using immortal tumor-derived cell lines such as rat basophilic leukemia 2H3 (RBL) cells or the human mast cell lines HMC-1 or LAD2. Benefits of immortal cell lines include homogeneity and ease of culture; however, studies of adherence, receptor expression, and enzyme content have shown each of these mast cell-like cells lines to be only marginally representative of mature, tissue bound, non-transformed mast cells.[6-8] Another strategy for mast cell studies involve culturing mast cell-like cells from bone marrow or blood-derived immature precursors for 4-6 weeks with chemokines to drive mast cell maturation. Such cell cultures produce generally homogeneous mast cell-like cell populations, but they are not ideal due to length of culture time, expense of culture media, scarcity of precursor cells, and disparity between in vivo and in vitro culture conditions. Studies of primary culture mast cells employ the isolation of a cell suspension often from a mouse or rat peritoneal cavity. Cell suspensions generally contain a mixture of cells including ~3% mast cells, ~ 30% macrophages ~50-60% B cells and ~5-10% T cells and are co-cultured with fibroblasts to maintain mast cell viability.[9,10] These heterogeneous cell cultures more closely model the in vivo environment of mast cells, which are in contact with macrophages and connective tissue cells but present challenges because mast cells make up less than 3% of the total cell population. It is already well known that IgE-sensitized mast cells secrete serotonin in several different cell models. However, how mast cell models change their response to their environment and the effects that the environment plays in IgE-allergen secretion over a period of time, in which mediators can stimulate other cell types or be cleared from the extracellular milieu, has not been evaluated. In this work, a heterogeneous cell culture containing primary culture murine peritoneal mast cells (MPMCs) is studied to characterize the time-dependence of mast cell response to allergen stimulation. The serotonin secretion behavior of MPMCs in a heterogeneous cell culture was compared to that from immortal RBL cells. When an unexpected 5-HT secretion trend was observed in the primary culture MPMCs, the time- and concentration-dependence of serotonin uptake in the heterogeneous MPMC culture was examined. Additionally, because mast cells play a central role in inflammatory diseases such as asthma, primary culture mast cells were exposed to CXCL10 and CCL5, two important asthma-related inflammatory cytokines that have recently been shown to induce mast cell degranulation at the single-cell level with different degranulation kinetics than IgE-mediated response to allergen.[11] To further understand these differences in time-dependent mast cell communication mechanisms, MPMC secretion of 5-HT and bioactive lipids was measured at various time points from 10 - 90 min following exogenous 5-HT exposure. These experiments aim to reveal differences in mast cell biochemical pathways leading to exocytosis.

7.3 Experimental Approach

7.3.1 Reagents

All materials used for cell culture were obtained from HyClone. Recombinant murine CXCL10 and CCL5 were purchased from Shenandoah Biotechnology Inc. and stored as suggested. LTC_4, LTD_4, LTE_4, PGD_2, and PAF and internal standards LTC_4-d_5, LTD_4-d_5, LTE_4-d_5, PGD_2-d_9, and PAF-d_4 were purchased from Cayman Chemical and used as received. LC/MS-grade acetonitrile (ACN) and water were purchased from JT Baker. LC/MS grade isopropyl alcohol (IPA) and a penicillin/streptomycin mixture were purchased from Fisher Scientific. Anti-trinitrophenol (TNP) IgE was purchased from BD Biosciences, while TNP-ovalabumin (TNP-Ova) was purchased from Fisher Scientific.

7.3.2 Mast Cell Isolation and Exposure to Chemokines

MPMCs were harvested from 10 week old C57BL/6J mice purchased from The Jackson Laboratory. Briefly, 8-9 mL of DMEM supplemented with 10% bovine calf serum and 1% penicillin and streptomycin (henceforth referred to as media) were injected into the peritoneal cavity of each mouse immediately following euthanasia (by CO_2 asphyxiation according to IACUC-approved protocol #0807A40164). Following a 30 second abdominal massage, approximately 6-7 mL of peritoneal lavage fluid per mouse were recovered. The collected cell suspension was pelleted by centrifugation at 450xg for 10 minutes, resuspended at 2×10^6 cells mL^{-1} in fresh media, and plated over Swiss albino 3t3 fibroblasts (purchased from ATCC). Cells were then cultured overnight with additional 500 µL of fresh media containing anti-TNP IgE such that the concentration of IgE in each well was 0.5 µg mL^{-1}.

After overnight incubation, MPMCs were washed three times with tris buffer (12.5 mM Trizma-HCl, 150 mM NaCl, 4.2 mM KCl, 5.6 mM glucose, 1.5 mM$CaCl_2$, 1.4mM $MgCl_2$) at 37 °C to remove serum-containing media. To investigate 5-HT processing by the cell culture, MPMCs were incubated with 0.1-0.55 µM 5-HT or tris buffer as a control, the supernatant was collected at specific time points, and the cells were lysed with 0.5 µM $HClO_4$ for 30 min. The supernatant and lysate 5-HT content was assessed by HPLC at various timepoints. For experiments evaluating the effect of stimulation with TNP-Ova, CXCL10, or CCL5 on MPMCs, cells were incubated for either 2 hours or particular time points of 10, 30, 60, and 90 minutes with tris buffer or with tris buffer containing 0.2-200 ng mL^{-1} CXCL10, 0.2-200 ng mL^{-1} CCL5, or 100 ng mL^{-1} TNP-Ova. Following incubation, degranulation was terminated by incubating the cells on ice for 10 minutes, and supernatants were collected for analysis by UPLC-MS/MS or HPLC with electrochemical detection.

7.3.3 HPLC Analysis of Serotonin

MPMC-secreted serotonin was detected and quantified by HPLC coupled to an electrochemical detector using a modified version of a previously published protocol.[12] Briefly, following MPMC incubation, 250 µL of supernatant was collected and filtered using a 0.45µm filter plate from Millipore (Billerica, MA) at 3000xg for 5 min. 180 µL of the filtered supernatant was added to 20 µL of 5 µM dopamine (used as an internal standard) in 0.5M $HClO_4$ for final concentrations of 0.5 µM dopamine and 500 mM $HClO_4$. The samples were vortexed and injected by an autosampler into an Agilent 1200 HPLC. Separation was achieved using a 5µm, 4.6 x 150 mm Eclipse XDB C18 column attached to a Waters 2465 electrochemical detector with a glassy carbon-based electrode. The working potential was set at 0.7 V vs. an in situ Ag/AgCl reference electrode with a current range of 50 nA. The HPLC flow rate was 2 mL/min using a mobile phase mixture consisting of 11.6 mg L^{-1} of the surfactant sodium octyl sulfate, 170µL L^{-1} dibutylamine, 55.8 mg L^{-1} Na_2EDTA, 10% methanol, 203 mg L^{-1} sodium acetate anhydrous, 0.1M citric acid, and 120 mg L^{-1} sodium chloride.

A 5 point calibration curve was constructed by plotting the ratio of serotonin to dopamine (internal standard) spike areas in solutions containing 500 nM dopamine and 28-1000 nM serotonin in 0.5 M $HClO_4$. The line of best fit for an average calibration curve for several representative experiments was $y = 2.0578+0.0088$ with $R^2=0.9992$, where y = spike area of 5-HT/spike area of internal standard and x = 5-HT concentration. Cell-secreted serotonin was quantified using the experimentally generated calibration curve.

7.3.4 UPLC-MS/MS Determination of Secreted Lipids

UPLC-MS/MS analysis was performed using a previously published method.[13] Briefly, supernatants from MPMCs were collected, spiked with 25 ppb of each of the internal standards LTC4-d_5, LTD4-d_5, LTE4-d_5, PGD2-d_9, and PAF-d_4 and concentrated in a centrifugal evaporator until the remaining volume was approximately 50 µL. After concentrating, salts were precipitated by the addition of 100 µL ice-cold ethanol containing 0.1% formic acid (FA) and 200 µL mobile phase B (90/10 ACN/IPA containing 0.1% FA). Precipitated salts were removed by centrifuging for 10 minutes at 12,000 RCF, and supernatants were again concentrated to approximately 20 µL. Samples were then resuspended in 100 µL 70/30 mobile phase A/mobile phase B (with A: water containing 0.1% formic acid and B: 90/10 acetonitrile/isopropyl alcohol containing 0.1% formic acid). For UPLC-MS/MS analysis, a Waters Acquity UPLC coupled to a Waters triple quadrupole mass spectrometer (Acquity TQD) were used. Separation was performed on a Waters BEH C-18 2.1 mm x 50 mm column at 45 °C employing the following 5 min gradient separation at a flow rate of 0.6 mL per minute: 30% B, 0 min to 0.5 min; 30% B to 50% B, 0.5 min to 1.0 min; 50% B 1.0 min to 2.0 min; 50% B to 90% B, 2.0 min to 2.2 min; 90% B, 2.2 min to 3.2 min; 90% B to 30% B, 3.2 min to 3.5 min; and 30% B, 3.5 min to 5.0 min.

7.3.5 Assay for β-Hex Secretion

To determine if incubation with 5-HT directly induced MPMC degranulation, supernatant content of the granule-stored enzyme β-hexosaminidase (β-Hex) was assessed as described previously.[13, 14] Briefly, 50 µL supernatant samples were collected in a 96 well plate and stored overnight at -80°C. When thawed, supernatants were incubated for 60 min at 37°C with 100 µL 1 mM 4-nitrophenyl N-acetyl-β-D-glucosaminide in 0.1 M citrate buffer at pH 4.5. After 60 min, 150 µL ice cold 0.1 M carbonate buffer at pH 9 was added, and absorbance of each well was recorded at 405 nm with a background subtraction absorbance reading at 630 nm.

7.4 Results and Discussion

7.4.1 Time-dependent MPMC and RBL Cell Response to IgE-mediated Stimulation

While MPMCs have been used for many studies of single mast cell secretion kinetics (usually tracking events on the ms to s timescale), the longer term (min-hrs) serotonin secretion of MPMCs in a heterogeneous cell culture has not been explored. To examine the time-dependence of mast cell response to IgE-mediated allergen stimulation, MPMCs were incubated overnight

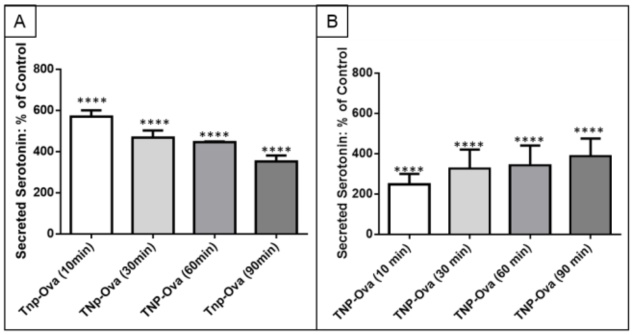

Figure 7.1 Time-dependent effects of serotonin secretion: secretion from A. MPMCs and B. RBL cells. ****$p < 0.0001$ vs. supernatant 5-HT concentration of control (unactivated) MPMCs or RBL cells. Control refers to the concentration of 5-HT in the supernatant of MPMCs for A RBL cells for B exposed to tris buffer, normalized to 100%.

with anti-TNP IgE, washed three times, then exposed to 100 ng mL^{-1} TNP-Ova. After exposure to TNP-Ova, supernatants from the adherent cell culture were collected and analyzed for secreted mediators at discrete time points to probe the kinetics of long-term secretion of preformed granules. As previous research has indicated that exocytotic cells only partially secrete their granule contents upon direct stimulation,[15] it was hypothesized that supernatant 5-HT concentration would steadily increase over the course of 90 min exposure to allergen stimulation. However, Fig. 7.1A shows that over the course of 90 min, exposure to TNP-Ova resulted in an increase followed by a decrease in secreted serotonin. Unsurprisingly, after 10 min of incubation with TNP-Ova, secreted serotonin increased to 571 ± 30% of control serotonin. After 10 min, however, serotonin concentration in MPMC supernatants ([5-HT]$_{\text{supernatant}}$) steadily decreased to 351 ± 30% of 5-HT control cell concentration at 90 min (Fig. 7.1A). MPMCs are cultured in a heterogeneous cellular environment, and although this type of cell culture more closely models the in vivo cellular environment than homogeneous immortal cell lines, heterogeneity can obscure the fate of the secreted serotonin. To probe the effect of the heterogeneous cell culture on secreted serotonin, MPMC 5-HT secretion was compared to that of the homogenous RBL cell line. RBL cells, while widely accepted as different from mast cells, share the common mast cell traits of adherence, FcεRI receptor expression, and degranulation in response to IgE-mediated stimulation.[8] Figure 7.1 shows that the RBL cells continually secrete more serotonin over the course of 90 min, quite distinct from the serotonin secretion trend exhibited by cultured MPMCs. When compared to the steadily increasing RBL cell [5-HT]$_{\text{supernatant}}$ concentration (Fig. 7.1B), the decreasing trend in MPMC [5-HT]$_{\text{supernatant}}$ (Fig. 7.1A) indicates a process of metabolism or reuptake by the cells in culture. This difference demonstrates the importance of the choice of cell culture when examining cell-to-cell communication behavior and interactions in response to changes in the environment.

7.4.2 Exogenous 5-HT Effects on MPMC Culture

Mast cell secretion of 5-HT (along with other granule-stored and de-novo manufactured mediators critical to cell-cell communication and inflammation) has several known downstream effects and potentially many other effects on mast cells themselves and surrounding cell types. Expression of the 5-HT specific reuptake transporter (SERT) has been detected on mast cells, macrophages, and B cells.[16-18] To explore the role that the cell culture microenvironment plays in MPMC 5-HT secretion, MPMCs were incubated with tris buffer containing concentrations of 5-HT ranging from 0.1 µM to 0.55 µM. These incubations were intended to model the environment that un-activated (but IgE-sensitized) cells would experience when in contact with activated MPMCs. Data represented in Fig. 7.1 and 7.4 presented as percent of control show that TNP-Ova stimulated MPMCs generate supernatant 5-HT concentrations of 0.4 – 5 µM, and MPMCs exposed to inflammation-relevant cytokines generate 0.1 – 0.2 µM 5-HT in the cell culture supernatant. To create a similar environment, the number of mice and conditions were accounted for to achieve similar ratios and amount of cells. At 10, 30, and 60 min of serotonin incubation, the cell culture supernatants were collected and analyzed for 5-HT, and the adherent cells were lysed and analyzed for 5-HT content. In Fig. 2, the total system 5-HT is presented as a percentage of the sum of the control supernatant, control cell lysate, and incubation 5-HT concentrations. For this work, the total system 5-HT refers to the 5-HT in the cell supernatants and cell lysates. To account for the exogenous concentration of 5-HT in the cell cultures, Equation 7.1 was used to calculate the total system 5-HT.

Equation 7.1: Total System 5-HT

$$= \frac{[\text{5-HT}]_{\text{Lysate}} + [\text{5-HT}]_{\text{Supernatant}}}{\text{Control}[\text{5-HT}]_{\text{Lysate}} + \text{Control } [\text{5-HT}]_{\text{Supernatant}} + [\text{5-HT}]_{\text{Exogenous}}} \text{x}100\%$$

Surprisingly, the 5-HT content of the cell cultures exhibited a decreasing trend with increasing 5-HT incubation concentrations. The correlation between 5-HT as a percent of control and 5-HT incubation concentration was significant at 30 min ($p = 0.0009$) and 60 min ($p = 0.02$) but not at the earliest time point of 10 min ($p = 0.07$). This indicates that, over the course of 30-60 min, the heterogeneous cell culture, including the macrophages, B cells, and mast cells which have been shown to contain SERT, processes 5-HT.[17-19] Exposing the cell culture to higher concentrations of exogenous 5-HT leads to a proportionally greater degree of cellular processing of 5-HT. To determine if supernatant-contained species were causing degranulation and/or caused the secretion of serotonin to be higher than that of our controls, a β-Hex assay was used to indicate extents of cell degranulation. When the β-Hex data were analyzed using a one-way ANOVA, the supernatants of MPMCs incubated with 0.4 µM and 0.55 µM 5-HT for 60 min secreted significantly more β-Hex than control MPMCs at the same timepoints ($p = 0.03$ and $p = 0.02$ for 0.4 µM 5-HT and 0.55 µM 5-HT incubation, respectively). No significant difference was detected between control β-Hex values and β-Hex values for the 0.1 – 0.55 µM 5-HT incubation at 10 min or 30 min or between controls and 0.1 – 0.3 µM 5-HT incubation at 60 min ($p > 0.05$). So, only the highest exogenous 5-HT concentrations and the longest incubation times induced significant increases in mast cell degranulation, meaning that degranulation alone does not account for the cells' 5-HT processing behavior (β-Hex data not shown). Previous studies on the effects of exogenous 5-HT on mast cells using bone marrow-derived or blood progenitor-derived mast cell models determined that 5-HT affects mast cell adhesion but does not induce mast cell degranulation.[17] It is likely that mast cells in culture with a heterogeneous mix of other cells (as would be present in vivo) experience a different chemical microenvironment than that of mast cells derived from blood or bone marrow progenitor cells, and this may result in different autocrine and/or paracrine effects of exposure to cell-cell communication species, including 5-HT. Changes in chemical microenvironment as a result of incubation with 5-HT after 60 minutes may induce secretion of mediators by surrounding cells, which stimulates mast cell degranulation of β-Hex and 5-HT.

To evaluate whether the trend in cellular processing of 5-HT shown in Fig. 7.2 was a result of supernatant 5-HT metabolism, intracellular 5-HT up-take and metabolism (indicating intracellular MPMC 5-HT metabolism) or a combination of both, Fig. 7.3 shows the MPMC supernatant and lysate 5-HT trends for each 5-HT incubation condition separately. To compare the supernatant 5-HT concentrations of MPMCs incubated with exogenous 5-HT to control MPMC supernatants, the 5-HT values in the solid bars of Fig. 7.3 are represented as a percentage of the sum of the control (MPMC supernatant 5-HT + 5-HT concentration of the MPMC incubation). Trends in MPMC supernatant 5-HT content are shown in Table 7.1; after 10 min, the supernatant concentrations of 5-HT were significantly decreased in comparison to the 5-HT content of the

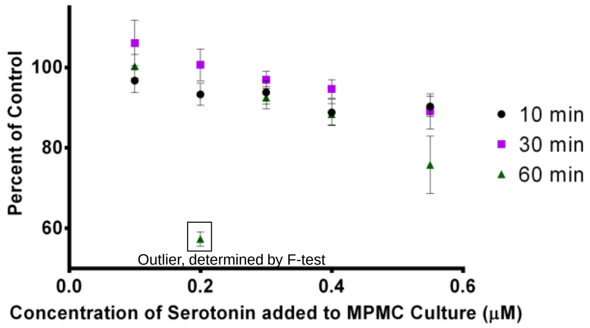

Fig. 7.2 Time-dependent effects of incubating MPMCs with 0.1-0.55 µM 5-HT: Percents of control were calculated using Equation 1. Each data point represents the total system serotonin (the sum of 5-HT concentration in supernatant as well as in lysed cells) as a percentage of the total system serotonin in control cells. The 0.2 µM incubation condition at 60 min was determined to be an outlier using the extra-sum-of-squares F tests ($p \leq 0.05$).

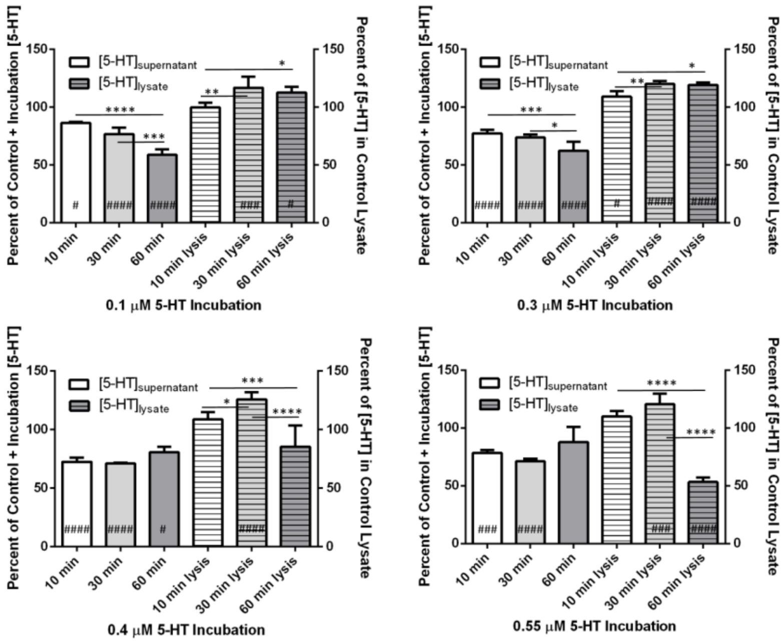

Figure 7.3 Supernatant and lysate 5-HT content of MPMCs incubated with 0.1 – 0.55 µM 5-HT for 10-60 min. #$p \leq 0.05$ vs. control; ###$p < 0.001$ vs. control; ####$p < 0.0001$ vs. control; *$p \leq 0.05$; **$p < 0.01$; ***$p < 0.001$; ****$p < 0.0001$.

Exogenous [5-HT] (μM)	10 min vs. Control MPMCs	10 min vs. 30 min	30 min vs. 60 min	10 min vs. 60 min
0.1	-13.7%	ns	-23.5%	-32.0
0.2	-16.9%	ns	▨	▨
0.3	-22.9%	ns	-15.4%	-19.2%
0.4	-27.7%	ns	ns	ns
0.55	-21.5%	ns	+23.2%	ns

Table 7.1 Trends in MPMC supernatant 5-HT content over the course of 60 min at varying exogenous concentrations of 5-HT. Where significant ($p \leq 0.05$ using one-way ANOVA), the percent increase or decrease is indicated, and ns = not significant, $p > 0.05$ using one-way ANOVA

Exogenous [5-HT] (μM)	10 min vs. Control MPMCs	10 min to 30 min	30 min to 60 min	10 min to 60 min
0.1	ns	+17.1%	ns	+13.0%
0.2	ns	+20.0%	▨	▨
0.3	+9.01%	+9.97%	ns	+9.31%
0.4	ns	+15.8%	-21.4%	-21.4%
0.55	ns	ns	-55.8%	-51.5%

Table 7.2 Trends in MPMC lysate 5-HT content over the course of 60 min at varying exogenous concentrations of 5-HT. Where significant, ($p \leq 0.05$ using one-way ANOVA), the percent increase or decrease is indicated, and ns = not significant, $p > 0.05$ using one-way ANOVA

supernatant of MPMCs exposed to no exogenous 5-HT ($p \leq 0.05$ using one-way ANOVA) at all exogenous 5-HT concentrations examined, when controlling for the concentration of 5-HT added to the cells. After 30 min of incubation with 5-HT, the supernatant 5-HT content did not change significantly from the 10 min timepoint supernatant 5-HT content at any of the exogenous 5-HT conditions ($p > 0.05$). After 60 min of incubation, however, the 5-HT content of MPMC supernatants exhibited a dependence on exogenous [5-HT]. The [5-HT] of supernatants of MPMCs incubated with lower concentrations of 5-HT, 0.1 and 0.3 μM, decreased significantly at 60 min vs. 10 min ($p < 0.0001$ for both). However, as the exogenous 5-HT concentration increased, the reverse effect was observed: at 0.4 μM and 0.55 μM exogenous 5-HT, supernatant 5-HT content did not change significantly at 60 min incubation vs. at 10 min of incubation ($p > 0.05$). In summary, assessing supernatant β-Hex content indicated that at the longest incubation times and highest incubation concentrations, MPMC degranulation was induced, which would increase the 5-HT content of the supernatant. This may explain the trend of decreased supernatant 5-HT in MPMCs incubated with low concentrations of exogenous 5-HT and the opposite trend observed at higher concentrations of exogenous 5-HT. Cells exposed to the 0.4 -0.55 μM exogenous 5-HT for 60 min likely experience a chemical microenvironment similar to what they would experience when MPMCs are responding to allergen (as many mast cells degranulate). MPMC secretion of 5-HT must induce surrounding cells to secrete chemical species that in turn can induce further activation of mast cells. The difference between trends in supernatant 5-HT decrease at low (0.1 and 0.3 μM) and high (0.4 and 0.55 μM) 5-HT incubations indicate that 5-HT metabolism by the cell culture has both time and concentration dependence. Several studies have reported on the mechanisms of clearance of 5-HT in the brain[19-21] and determined that, while SERT has a high binding affinity for 5-HT ($K_d = 6.7$ nM),[22] there are also other mechanisms by which 5-HT is cleared, as SERT-knockout mice demonstrate the ability to clear 5-HT.[21] Although they have lower binding affinity for 5-HT than SERT, the extraneuronal monoamine transporter, plasmalemmal monoamine transporter, and the organic cation transporters 1-3 are several receptors with the ability to clear extracellular 5-HT efficiently.[21] While it is known that mast cells and macrophages express SERT, little is known about the non-SERT clearance of 5-HT by macrophages and mast cells. Additionally, as 5-HT clearance varies by local area within the brain,[23] it is highly likely that 5-HT clearance in non-neuronal tissue by SERT and non-SERT mechanisms will differ from brain synaptosomes. Clearly, further study on the clearance of extracellular 5-HT by peripheral tissues is warranted.

Analysis of the cell lysate 5-HT content revealed interesting trends in the uptake of 5-HT by the cell culture, which are detailed in Table 7.2. Of the 5-HT incubation concentrations examined, only 0.3 µM 5-HT produced a significant increase in cell-stored 5-HT concentration (compared to controls) after 10 min of incubation ($p = 0.05$). The trends in cell-stored 5-HT over the course of 10 to 60 min indicate significant increases at 5-HT incubation concentrations of 0.1 and 0.3 µM and significant decreases for 5-HT incubation concentrations of 0.4 and 0.55 µM. The overall 60 min decrease at the higher exogenous concentrations of 5-HT is likely due in part to the induction of MPMC degranulation by the incubation itself.

7.4.3 Stimulation Effects: Inflammatory Cytokines CXCL10 and CCL5

The concentration and time-dependent trends in supernatant and lysate 5-HT concentration of MPMCs exposed to exogenous 5-HT have potential implications for in vivo effects of intercellular 5-HT. Mast cells are a critical cell type in the pathogenesis of inflammatory diseases such as asthma.[3] Their involvement in inflammatory diseases is influenced by cell-to-cell communication with surrounding cell types, which secrete chemokines recently shown to directly induce mast cell degranulation.[11] Mast cells undergoing degranulation in response to IgE-mediated stimulation secrete more 5-HT than mast cells responding to inflammatory chemokines such as CXCL10 or CCL5. The trends in Tables 7.1 and 7.2 indicate that the cells that surround MPMCs (and potentially mast cells localized to other tissues) will have different rates of uptake or metabolism of 5-HT, and this will likely affect the pathophysiology of surrounding cell response to MPMC secretory behavior following exposure to chemokines vs. allergen.

To further explore MPMC response to stimulation over the course of min-hrs and environmental effects, the long term time-dependent response of MPMCs to inflammatory

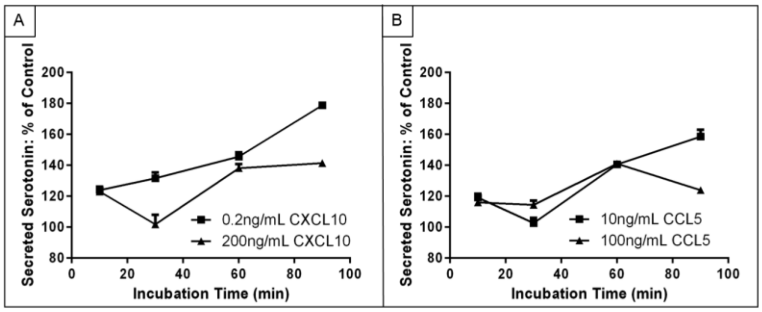

Figure 7.4 Supernatant 5-HT content as a percent of control MPMC supernatant 5-HT content after MPMC exposure to the inflammatory cytokines A. CXCL10 and B. CCL5.

chemokines was compared to TNP-Ova stimulation. Mast cells are most commonly known for their central roles in allergic response, and the TNP-Ova models that response. In this case, the MPMCs were incubated overnight with anti-TNP IgE, and then exposing them to TNP-Ova induces IgE-mediated degranulation. Although response to allergen stimulation is the most widely known function of mast cells, these cells have diverse and complex roles in a number of inflammatory diseases. By comparing the effects of inflammatory disease-relevant chemokines on MPMCs to the widely studied allergen response of MPMCs, this work attempts to probe the complex response of mast cells to subtle changes in chemical microenvironments. The inflammatory chemokines CXCL10 and CCL5 were selected because of their roles in mediating the cell-to-cell communication processes that give rise to asthma. CXCL10 in particular has a central role in the pathogenesis of asthma. IgE-sensitized MPMCs were exposed to 0.2-200 ng mL^{-1} CXCL10 or CCL5, and the 5-HT content of the cell supernatants were measured after 2 hrs of incubation. Direct stimulation of MPMCs was observed at a wide range of concentrations of both CXCL10 and CCL5 (results not shown). Based on the results after 2 hrs of exposure to a wide range of concentrations, two concentrations each of CXCL10 and CCL5 were selected for further time-dependent study based on the robustness of the MPMC response following exposure to them.

MPMCs were exposed to CXCL10 at 0.2 and 200 ng mL^{-1} or CCL5 at 10 and 100 ng mL^{-1}, and supernatants were sampled at 10, 30, 60, and 90 min for 5-HT content measurement. Trends in 5-HT secretion in response to the cytokines are shown in Fig. 7.4. In contrast to the robust degranulation response that decreased over the course of 90 min following MPMC exposure to TNP-Ova, exposing MPMCs to CXCL10 or CCL5 generated a smaller degranulation response with an overall increasing trend in secreted 5-HT over the course of 90 min. Stimulation with CXCL10 induced mast cell degranulation to a lesser extent than TNP-Ova stimulation from the same mast cell population, which on average induced a 4.6 times greater secretion of 5-HT than CXCL10. The two stimulant concentrations of CXCL10 also induced different time-dependent trends in 5-HT secretion. Upon stimulation with 0.2 ng mL^{-1} CXCL10, supernatant 5-HT increased continuously over 90 min. MPMC exposure to 200 ng mL^{-1} CXCL10 resulted in an initial increase in supernatant 5-HT content at 10 min, followed by a return to control 5-HT levels at 30 min and another increase in 5-HT levels from 30-90 min. Interestingly, MPMC stimulation with CCL5 resulted in similar overall trends to stimulation with CXCL10, but the chemokine concentration dependence was reversed: 5-HT secretion following stimulation with 100 ng mL^{-1}

CCL5 followed the same general trend as 5-HT secretion in response to 0.2 ng mL^{-1} CXCL10, and stimulation with 10 ng mL^{-1} CCL5 resulted in similar 5-HT concentration fluctuations as MPMC exposure to 200 ng mL^{-1} CXCL10. Both CXCL10 and CCL5 are mast cell chemoattractants that induce MPMC degranulation over a wide range of chemokine concentrations. The contrast in temporal response of MPMCs to low and high concentrations of these chemokines highlights the complex role of mast cells in inflammatory diseases. While in vivo mast cells are likely exposed simultaneously to multiple chemokines as they move toward the site of inflammation, examining the response of mast cells to individual mediators of inflammatory diseases can reveal information about MPMC response to different aspects of inflammation.

The response of surrounding cells to different concentrations of exogenous 5-HT is also informative of the diverse role of mast cells in inflammation. TNP-Ova stimulation of MPMCs generates supernatant 5-HT concentrations of 0.4-0.55 µM, and stimulation with CXCL10 or CCL5 generates supernatant 5-HT concentrations of 0.1-0.2 µM. As the trends in Table 7.1 highlight, exposing MPMCs to 0.4-0.55 µM 5-HT results in an initial decrease in supernatant 5-HT concentration, likely due to MPMCs and macrophages taking up and/or processing the 5-HT, followed by an increase or no change in the supernatant 5-HT concentration. When the heterogeneous cultures were exposed to lower concentrations of 5-HT, the decrease in supernatant 5-HT concentration was more pronounced and continued for 60 min. When MPMCs are exposed to TNP-Ova, the concentrations of secreted 5-HT are high enough that the surrounding cell culture does not process the secreted 5-HT as efficiently as the lower secreted 5-HT

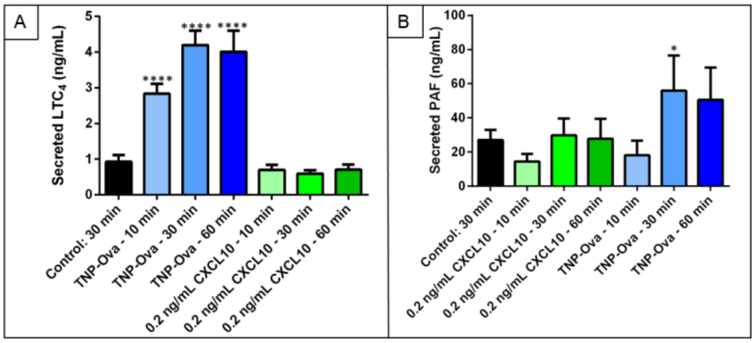

Figure 7.5 MPMC secretion of the bioactive lipids. A. LTC4 and B. PAF in response to TNP-ova or 0.2 ng mL^{-1} CXCL10. *p = 0.02; ****p < 0.0001.

concentrations induced by the inflammatory chemokines CXCL10 and CCL5.

The secretion of 5-HT by mast cells is an important component of understanding mast cell function in both allergic response and inflammatory disease; however, mast cells secrete many other chemical species that contribute to their roles in physiological processes. In asthma, the effect of CXCL10 on mast cells is particularly important,[24, 25] and previous studies have shown that CXCL10 potentially activates MPMCs through a different pathway than IgE-mediated allergen stimulation.[11] To further examine the effects of stimulation by response to allergen vs. inflammatory chemokines on MPMC function, the secretion of bioactive lipids from MPMCs exposed to 0.2 ng mL^{-1} CXCL10 or 100 ng mL^{-1} TNP-Ova was also examined. MPMC supernatant concentrations of LTC_4 and PAF were determined using UPLC-MS/MS, and results are shown in Fig. 7.5. As expected, TNP-Ova activation of MPMCs induced an increase (vs. unactivated MPMCs) of LTC_4 secretion and PAF secretion. CXCL10 exposure, however, did not significantly increase the secretion of LTC_4 or PAF ($p > 0.05$ vs. control MPMCs). In addition to the differences between CXCL10 and TNP-Ova-induced degranulation of MPMCs, the mechanism by which CXCL10 activates mast cells likely does not induce bioactive lipid secretion. Further studies on the effects of cell-secreted cytokines are clearly needed to better understand the complex role that mast cell activation plays in inflammatory diseases.

7.5 Conclusions

In this work, MPMC response is shown to be highly regulated and responsive to subtle alterations in a complex environment through time- and concentration-dependent degranulation and bioactive lipid formation. These results highlight the importance of selecting an appropriate mast cell model when studying mast cell involvement in allergic response and inflammation. This work probed both the effects of 5-HT concentration and time on surrounding cells in culture with MPMCs as well as mast cell response to different stimuli. The MPMC co-culture system actively responds to the presence of 5-HT, which in vivo may correspond to the ability of cells localized near mast cells to limit the concentration of inflammatory mediators in the extracellular microenvironment. The correlation between the processing of exogenous serotonin and time supports that heterogeneous cellular systems are able to efficiently respond to inflammation. When attempting to apply in vitro mast cell results to in vivo systems, considering the environment that the mast cell is experiencing is important for understanding mast cell contribution to inflammation.

MPMCs exhibited controlled secretion dependence when exposed to different agents of mast cell activation. The relatively small degree of degranulation of MPMCs in response to the cytokines CXCL10 and CCL5 in contrast to the robust response of MPMCs to TNP-Ova (allergen) are potentially due to the chemoattractant roles of the cytokines. Mast cell contact with chemoattractants in vivo generally occurs when mast cells are localized away from the site of inflammation. Mast cell secretion of small amounts of serotonin and other granule-associated mediators increases vascular dilation, which allows chemoattractants including CXCL10 and CCL5 to enable mast cells to move more efficiently to the site of inflammation.

Chapter 8: Analysis of Neuropeptide-Induced Mast Cell Degranulation and Characterization of Signaling Modulation in Response To IgE Conditioning

This work was completed with the assistance of Benjamin M. Manning, Audrey F. Meyer, and Christy L. Haynes

Parts of this manuscript also appeared in Benjamin Manning's thesis

8.1 Overview

As tissue-resident immune cells, mast cells are frequently found in close proximity to afferent neurons and are subjected to immunoactive mediators secreted by these neurons, including substance P (SP) and calcitonin gene-related peptide (CGRP). Neurogenic inflammation is thought to play an important role in the pathophysiology of many diseases. Unraveling the cellular mechanisms at the interface between the immune response and the peripheral nervous system is important for understanding how these diseases arise and progress. In this work, mast cell degranulation following direct exposure to CGRP and SP was studied both at the bulk and single-cell levels to characterize the mast cell response to neuropeptides and compare this response to well-studied mast cell activation pathways. Results show that mast cells secrete fewer chemical messenger-filled granules with increased IgE pre-incubation concentrations. The biophysical characteristics of mast cell degranulation in response to SP and CGRP is in many ways similar to calcium ionophore-induced mast cell degranulation; however, neuropeptide-stimulated mast cells secrete fewer chemical messengers per secretion event, resulting in an overall relative decrease in secreted chemical messengers.

8.2 Introduction

Mast cells, often implicated for their role in allergy and inflammation, contain a large number of cytoplasmic granules with preformed mediators including, but not limited to, histamine, serotonin, tumor necrosis factor α (TNF-α), and beta hexosaminidase, which are secreted in response to a diverse set of environmental signals. Additionally, chemokines, growth factors, prostaglandins, leukotrienes and TNF-α can be synthesized *de novo* and secreted into the extracellular environment upon mast cell activation. These secreted mediators enhance inflammation, pain, and vasodilatation at the site of activation. [1, 2] This process has been extensively described in the context of allergy wherein mast cells are activated via multivalent antigen-mediated crosslinking of immunoglobulin E (IgE) bound to the high affinity IgE receptor FcεRI or the low affinity IgE receptor, FcεRII (also known as CD23). [3, 4]

Although the central role of mast cells in allergic (IgE-mediated) processes of the immune system is well established, their role in many other immune functions, including neurogenic inflammation, is not as clearly defined. The localization of mast cells in connective tissue and mucosal sites throughout the body facilitates contact with a wide range of complex and diverse microenvironments. This diversity is magnified by an equally broad set of functions that mast cells perform within their environment, including activation in response to immune signals such as chemoattractants and neuropeptides. [1, 5-8] Activation by neuropeptides can initiate and sustain feedback signaling between mast cells and the surrounding tissue microenvironment.

Of particular interest to this work is the secretion of substance P (SP) and calcitonin gene-related peptide (CGRP) from peripheral neurons. SP is a member of the tachykinin class of peptides which act through the neurokinin family of receptors (NKRs).[9,10] CGRP, as its name suggests, is an alternative splicing product of the calcitonin gene and acts through the calcitonin receptor-like receptor (CRL).[10,11] These neuropeptides are widely recognized for their role in many inflammatory diseases including atopic dermatitis, asthma, and arthritis.[12-17] Both substance P and CGRP are secreted from the same subset of capsaicin-sensitive primary afferent neurons and are co-localized in, and co-secreted from, dense-core secretory granules at peripheral axon terminals.[9,10] Similarly, both substance P and CGRP have been shown to induce mast cell degranulation as part of the pro-inflammatory functionality of these neuropeptides, propagating the inflammatory response through the secretion of histamine and TNF-α, which act on the afferent peripheral neurons.[9,14,18-20] Although substance P-induced mast cell degranulation has been established in certain mast cell subtypes, the data exploring the effects of CGRP on mast cell degranulation are mixed.[8,14,21-23] Furthermore, despite mast cell expression of both CRL and NKRs, it also has been suggested that substance P- and CGRP-induced mast cell degranulation may result from direct activation of GTP-binding (G) proteins rather than receptor-mediated signaling.[2, 8, 9]

This intricate system is critical to neurogenic inflammation, and it is important to clearly understand the individual roles of each cell type and molecular signaling species at the single cell level. However, beyond the limited use of whole-cell patch clamp techniques and fluorescence spectroscopy, [24] neuropeptide-induced mast cell degranulation has not been extensively studied at the single cell level. This work demonstrates the use of carbon-fiber microelectrode amperometry (CFMA) to characterize CGRP- and SP-induced mast cell degranulation from single cells. CFMA provides sub-millisecond resolution and sufficient sensitivity to detect individual cytoplasmic granule secretion events. Here, CFMA was used to explore the biophysical and kinetic properties of mast cell degranulation in response to neurogenic peptide stimulation. [6,7,25]

Several studies by other groups have described IgE-induced upregulation of neuropeptide receptors including the NK 1, 2, and 3 receptors for SP.[8,23] This work describes IgE concentration effects on neuropeptide-induced degranulation of mouse peritoneal mast cells in both bulk assays, utilizing high performance liquid chromatography (HPLC) with electrochemical detection, and single cell CFMA. To the best of our knowledge, IgE-dependent modulation of neuropeptide-induced mast cell degranulation has not been reported and may have significant implications for neurogenic inflammatory diseases.

Our results indicate that exposure to IgE decreases mast cell sensitivity to neuropeptide-induced degranulation. Additionally, CFMA data reveal individual mast cells stimulated by either SP or CGRP demonstrate remarkably similar biophysical degranulation kinetics. At the single-cell level, both neuropeptides induced the secretion of similar levels of serotonin from mast cells relative to the ionophore-stimulated control. The similar kinetics and number of granules secretion events during mast cell degranulation detected by CFMA suggests both neuropeptides act through a similar mechanism.

8.3 Experimental Approach

8.3.1 Reagents

Cell culture media materials were obtained from HyClone. Calcitonin gene related peptide (CGRP) (Rat, Mouse) was purchased from Phoenix Pharmaceuticals, Inc. [Tyr8]-Substance P and A23187 were purchased from Sigma Aldrich. Anti-trinitrophenol (TNP) IgE and TNP-ovalbumin (TNP-Ova) were obtained from BD Biosciences and Fisher Scientific, respectively. TNP-Ova, A23187, SP and CGRP were diluted in Tris buffer (12.5 mM Trizma-HCl, 150 mM NaCl, 4.2 mM KCl, 5.6 mM glucose, 1.5 mM$CaCl_2$, 1.4 mM $MgCl_2$) on the day of the experiment.

8.3.2 Mast Cell Isolation and Exposure to Chemokines

Peritoneal mast cells were isolated as previously described in Chapter 7 and the following references.[5, 7] Briefly, male C57BL/6J male mice from The Jackson Laboratories were euthanized via CO_2 asphyxiation according to IACUC approved protocol # 1403-31383A. 8 mL of high glucose DMEM supplemented with 10% bovine calf serum and 1% penicillin streptomycin (media) was injected into the peritoneal cavity followed by a 30 second abdominal massage. Approximately 6-7 mL of the peritoneal lavage media was collected from each mouse. The collected mast cells were pelleted at 450 xg for 10 minutes and resuspended in fresh media before being plated onto a confluent layer of 3T3-Swiss albino mouse embryo fibroblasts (purchased from ATCC). Mast cells were primed with IgE at the specified concentration from 0 to 1×10^{-7} M, as indicated in the experimental procedure, and incubated overnight at 37 ^{o}C in 5% CO_2. For single cell experiments, the mast cells were plated in 35 x 10 mm^2 Petri dishes while 24 well plates were used for bulk experiments. After overnight incubation, the cells were washed three times with tris buffer and prepared for bulk or single cell experiments.

8.3.3 Carbon-Fiber Microelectrode and Micropipette Fabrication

Microelectrodes were fabricated as previously described.[6, 7] Briefly, individual carbon-fibers were aspirated into glass capillaries which were then halved using a pipette puller. The excess fiber was cut using a surgical blade underneath a microscope. The electrodes were epoxied (Epoxy Technology) and cured at 100°C for 24 hours. On the day of the experiment, the electrodes were beveled at 45 degrees with a diamond-coated polishing wheel and placed into isopropyl alcohol until needed. For the stimulating micropipette, a glass capillary was halved using the pipette puller and trimmed to leave a 10-50 µm-diameter opening for the stimulant release driven by a Parker Picospritzer III.

8.3.4 Carbon-Fiber Microelectrode Experiments

The washed mast cells were placed into a 37°C heated petri dish holder on an inverted microscope. The carbon-fiber microelectrode and micropipette were placed on top and near the mast cell, respectively (Fig. 8.3A). A potential of 700 mV vs. AgAgCl reference electrode (BASi) was set using an Axopatch 200B potentiostat, and a 3 second bolus of stimulant was puffed onto the cell. The stimulants used were 10 µM A23187, 1 µM SP, or 1 µM CGRP. The change in current over time for 90 seconds was recorded using Tar Heel CV software (National Instruments, Austin, TX), written by Michael L.A.V. Heien. The data collected were filtered with a 200 Hz low-pass Bessel filter and converted to an .abf file format in the data analysis software (MiniAnalysis). The individual spikes in each current trace were analyzed for rise time from 10 to 90% of the spike amplitude (T_{rise}), full width at half max time ($T_{1/2}$), and total area; in addition, the total number of current spikes was counted. After the data were analyzed, outliers (any trace with one of more experimental parameters that was greater than 2 log standard deviations from the log mean for that condition) were removed. Data significance was determined using one way ANOVA and error is given in SEM. During the experiment, the secretion of 17, 18, and 14 individual cells was measured for A23187, CGRP, and SP conditions, respectively.

8.3.5 Bulk Mast Cell Experiments

Mast cells were stimulated with 250 µL of the selected neuropeptide at 1, 10, or 100 µM based on the experiment, 100 ng mL^{-1} TNP-Ova, or Tris and incubated at 37°C for 30 minutes for the initial experiments (Fig. 8.1) and 2 hours for the IgE variation experiments (Fig. 8.2) before terminating degranulation stimulation by placing cells on ice. The resulting supernatant was placed in a 96 well Millipore Multi Screen 0.45 µm filter plate and filtered by centrifuge at 3000 xg for 5 min. 180 µL supernatant and 20 µL of 5 µM dopamine internal standard in 0.5 µM perchloric acid were combined and placed into an HPLC vial and run using an Agilent 1200 HPLC with a Waters 2465 electrochemical detector as previously described. [5] Briefly, the solution was separated using a 5 µm, 4.6 mm × 150 mm Eclipse XDB C18, and the serotonin and dopamine were detected using a Waters glassy carbon electrode set at a potential of 700 mV vs. Ag/AgCl. The mobile phase, consisting of 11.6 mg L^{-1} of the surfactant sodium octyl sulfate, 170 µL L^{-1} dibutylamine, 55.8 mg L^{-1} Na_2EDTA, 10% methanol, 203 mg L^{-1} sodium acetate anhydrous, 0.1 M citric acid, and 120 mg L^{-1} sodium chloride, was run at 2 mL min^{-1}. In addition, a 5 point calibration curve was prepared using a 500 nM dopamine internal standard and serotonin concentrations ranging from 62.25-1000 nM serotonin dissolved in 0.5 M $HClO_4$. All spikes in the resulting chromatogram were analyzed by dividing the area of the serotonin spike by the dopamine spike area (5-HT/dopamine internal standard). For all experiments, the R^2 of the calibration curve was over 0.9993 with a minimum of 3 instrumental replicates for each calibration point. All mast cell conditions had 4 biological replicates and were q tested for outliers with 95% confidence. Significance between conditions was determined using one way ANOVA. Error bars represent standard deviation.

8.4 Results and Discussion

The complexity underlying cellular signaling during neurogenic inflammation makes it difficult to decipher the individual contributions of separate cell types. Using bulk and single cell approaches in combination can aid in differentiating the specific role mast cells play within the inflammatory environment. CFMA is used to detect and characterize the real-time secretion of serotonin molecules from individual granule secretion events by single cells, providing detailed information pertaining to the biophysical mechanisms of SP- or CGRP-induced mast cell degranulation. [16, 17, 25] HPLC with electrochemical detection, on the other hand, allows us to understand how cell response varies in more complex environments taking into account cell-cell interactions. While serotonin itself is not directly implicated in the inflammatory response, it is packaged with other small molecule mediators (in dense granules) that are secreted simultaneously, and thus can be measured as a proxy for small molecule inflammatory mediators. Mouse peritoneal mast cells were used in this work as a source of primary culture cells that provided accessibility, abundance, and compatibility with the measurement techniques employed herein.

8.4.1 Bulk Concentration and Initial IgE Incubation Studies

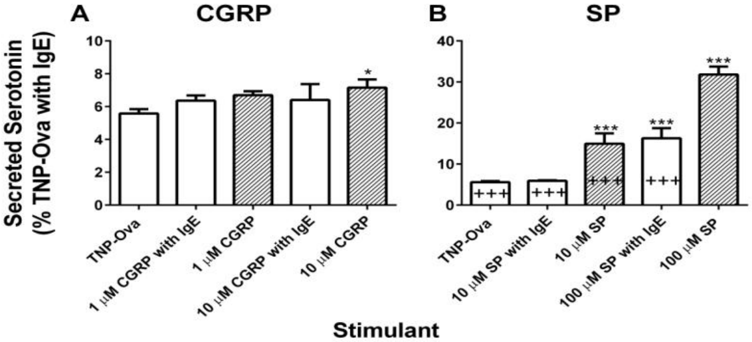

Figure 8.1 Bulk mast cell secretion in response to a 30 minute CGRP (A) or SP (B) stimulation at various concentrations. Results are shown as percent of the natural allergic (IgE-mediated) reaction pathway secretion. IgE concentrations were at 6.66 x10^{-9} M. The negative control was significantly different than 10 μM CGRP ($p<0.05$) and for all SP ($p<0.001$) in all conditions except 10 μM SP with IgE.* $P\leq 0.05$ vs. TNP-Ova *** $P\leq0.001$ vs. 10 μM SP with IgE and TNP-Ova +++ $P\leq0.001$ Vs. 100 μM SP

Studies using bulk assays of mast cell degranulation were conducted to optimize conditions for characterization of neuropeptide-induced mast cell degranulation and to assess the effect of IgE pre-incubation concentration on neuropeptide-induced mast cell secretion. Mast cells were stimulated with varying concentrations of neuropeptide (1 and 10 μM CGRP or 10 and 100 μM SP) for 30 minutes with or without 0.5 μg/mL IgE pre-incubation overnight (Fig. 8.1). Both positive and negative controls were included (TNP-Ova with and without anti-TNP-Ova IgE pre-incubation, respectively). A significant increase in secreted serotonin was only detected from CGRP-stimulated mast cells at the higher concentration (10 μM CGRP) in the absence of IgE pre-incubation ($p<0.05$). For SP stimulation, enhanced degranulation was observed in mast cells at concentrations of 10 μM SP without IgE and 100 μM SP with and without IgE. This information suggests direct mast cell degranulation in response to CGRP and SP. Furthermore, this neuropeptide-induced mast cell degranulation was both concentration- and IgE-dependent. CGRP-stimulated mast cells at low CGRP concentrations (Fig. 8.1A) did not demonstrate significant differences between stimulation conditions, however this could be due in part to the relatively low stimulation concentrations used. Only the 10 μM CGRP stimulation without IgE preincubation induced significantly increased secretion relative to the negative control, suggesting that higher concentrations of CGRP are needed to study IgE effects using bulk cell detection. SP-induced mast cell degranulation was significantly enhanced in response to increased concentration of SP and diminished in the presence of IgE (Fig.8.1B). In the absence of IgE pre-incubation, the total amount of serotonin secretion from mast cells increased by 153% and 96% following stimulation with 10 µM and 100 µM SP, respectively. One possible explanation for this response could be the modulation of SP receptors with the addition of IgE as previously reported.[8, 23] Conversely, downregulation of FcεRI proteins and mRNA has also been demonstrated in mast cells following stimulation with SP.[26] Our data further reinforces the relationship between IgE signaling and the mast cell response to neuropeptides.

8.4.2 IgE Concentration Varriation

To further explore the effect of IgE conditioning on neuropeptide-induced mast cell degranulation, MPMCs were stimulated with either 100 µM SP or CGRP with and without IgE pre-incubation. Pre-incubation concentrations of IgE were selected using the reported dissociation constants of the IgE receptors FcεRI (k_d = 10^{-9}-10^{-10}) and FcεRII (k_d = 10^{-7}).[3, 4] Three IgE concentrations were selected - a high concentration to ensure saturation of both FcεRI and FcεRII (1×10^{-7} M), a moderate IgE concentration between the respective K_d values of the two receptors (3×10^{-9} M), and a low concentration just below the FcεRI K_d (7×10^{-11} M). Mast cells without IgE pre-incubation were also prepared. Mast cells were incubated overnight with their corresponding IgE concentration, and washed before exposure to neuropeptide stimulation. TNP-Ova stimulated mast cells were incubated with 1×10^{-7} M IgE overnight to act as the positive control. In all conditions, mast cell supernatants were collected, and total serotonin content was analyzed using HPLC with electrochemical detection (Fig. 8.2).

At high incubation concentrations of IgE, neither CGRP nor SP induced significant mast cell degranulation relative to the negative control (Fig. 8.2). With decreasing pre-incubation concentrations of IgE, both CGRP (Fig. 8.2A) and SP (Fig. 8.2B) induced increasing amounts of mast cell serotonin secretion. SP stimulated mast cells at moderate IgE pre-incubation levels, whereas CGRP only induced mast cell degranulation at the lowest IgE concentration. In addition, SP-stimulated serotonin secretion did not continue to increase with decreasing concentrations of IgE beyond the 3×10^{-9} M IgE concentration, unlike the CGRP stimulation. This suggests that mast cells are more responsive to SP at normal IgE levels, while CGRP stimulation has a greater dependence on the IgE concentration.

These variations in response to the concentration of IgE may explain conflicting findings in the literature. Previous research has extensively reported mast cell stimulation in response to SP, while contradictory results have been reported for CGRP.[8,14,21-23] Most often, mast cells are primed with IgE at concentrations of 0.5 µg/mL or ~7 x10^{-9} M (assuming a molecular weight of 75 KDa as reported by BD-BioSciences who produces the IgE antibody used in these experiments) overnight. [5, 6, 8, 26] This concentration is above the K_d of FcεRI but below the K_d of FcεRII. Our findings suggest that this concentration of IgE incubation would significantly limit the degree of CGRP-induced mast cell degranulation, while permitting SP-induced serotonin secretion as seen in Fig. 8.1B.

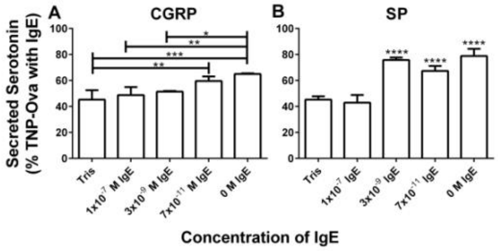

Figure 8.2 IgE concentration effects after a two hour MC stimulation with 100 µM CGRP (A) or 100 µM Substance P (B). * P≤0.05 ** P≤0.01 ***P≤0.001 vs indicated positions. ****P≤0.0001 vs tris and 1x10^{-7} M IgE with SP stimulation

8.4.3 Carbon-Fiber Microelectrode Amperometry

Neuropeptide-induced mast cell degranulation was also observed at the single cell level using CFMA. These experiments were conducted to achieve a more detailed and mechanistic understanding of how mast cell degranulation is impacted by SP and CGRP. Mast cell CFMA is a technique where a sub-10-μm-diameter carbon-fiber microelectrode is set to a fixed, oxidizing potential and placed in direct contact with a single mast cell (Fig. 8.3A).[25] The selected mast cell is then stimulated using a micropipette to deliver a local dose of a stimulating substance. The subsequent secretion of granular contents is monitored as discrete spikes in current, each corresponding to the exocytosis of a single cytoplasmic granule. For CFMA experiments in this work, a 3-second delivery of 1 µM substance P, 1 µM CGRP, or 10 µM A23187 (a calcium ionophore) were used to stimulate MPMC degranulation. The secreted serotonin from each granule is oxidized and monitored as current over time as the selected cell undergoes exocytosis (Fig. 8.3B). The sub-millisecond time resolution of these measurements facilitates detailed insight into the granule/membrane behavior. Within the collected current trace, individual granule secretion events (individual spikes) are analyzed for several kinetic parameters including spike rise-time (T_{rise}), full-width at half maximum ($T_{1/2}$), and total charge underneath the spike (Q) which is used to quantify the amount of serotonin secreted from each granule using Faraday's law (Fig. 8.3C). T_{rise} is a measure of the time between 10 to 90% of the full spike height during the initial rise in current and reflects the fast secretion of serotonin unassociated with the intragranular matrix immediately following fusion pore formation between the cytoplasmic and cell membranes. $T_{1/2}$ measures the length of time the granule fusion pore stays open for chemical messenger secretion. This is also associated with the rate at which the biopolymer matrix expands and unfolds to secrete a partial amount of its serotonin content. In addition to these kinetic parameters, the number of spikes (N) can be counted to determine the number of exocytotic events the individual mast cell experiences upon activation, taking into account that the microelectrode contacts ~10% of the total cell surface area.[25] Together, these parameters provide a detailed picture of the biophysical mechanics that underlie specific changes in mast cell secretory function. In particular, observed changes in the pattern of these parameters are often very useful when comparing different modes of mast cell stimulation that result in modulation of exocytosis.

To understand if the IgE concentration affects the secretion from isolated mast cells on a

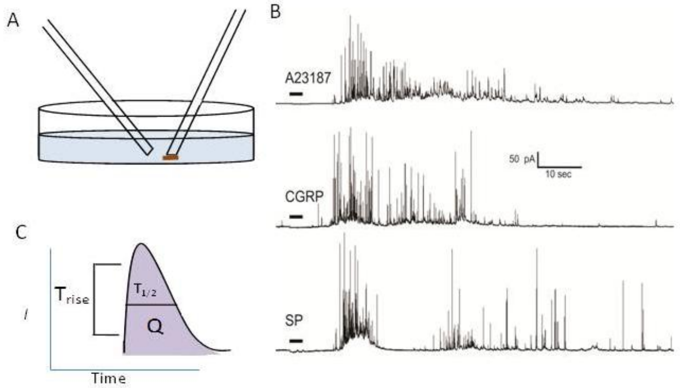

Figure 8.3 Schematic CFMA setup and example traces. A) CFMA setup (Ag/AgCl reference electrode not shown) B) Representative traces of single cell MC secretion C) Schematic current spike resulting from MC secretion of a single dense-body granule showing T_{rise} (the time from 10 to 90% of the spike height), $T_{1/2}$ (length of time for full width at half maximum), and Q (amount of serotonin secretion in units of charge).

single cell level, the mast cells were incubated overnight with or without 0.5 µg/mL IgE. After washing, individual cells were stimulated with SP or CGRP. No granule secretion was detected with CFMA for mast cells in either condition incubated with IgE. Mast cells not incubated overnight with IgE showed degranulation when stimulated with SP, CGRP or the positive control (10 µM A23187). Representative amperometric traces can be seen in Fig. 8.3B. In addition to demonstrating the effects of IgE on mast cells, the biophysical characteristics following stimulation were quantified using the parameters discussed above (Fig. 8.4 and 8.5).

8.4.4 CFMA Analysis

Analysis of the CFMA results revealed that individual mast cells stimulated with either SP or CGRP each yielded in less total serotonin than A23187-stimulated controls (SP- and CGRP-stimulated mast cells both secreted 39% less serotonin per cell than the A23187-stimulated cells, Fig. 8.4A). Further analysis of the CFMA data reveals this marked difference in the degree of mast cell degranulation is largely accounted for by a lower amount of serotonin secretion per granule, with no measureable difference in the number of secretion events per cell (Fig. 8.4B and 8.4C). SP- and CGRP-stimulated mast cells secreted 29% and 34% less serotonin per granule, respectively, relative to A23187-stimulated controls, with negligible changes in the number of granule fusion events. The stimulation-dependent alterations in spike area observed in the absence of different cell culture conditions suggests regulated control of the amount of chemical messenger

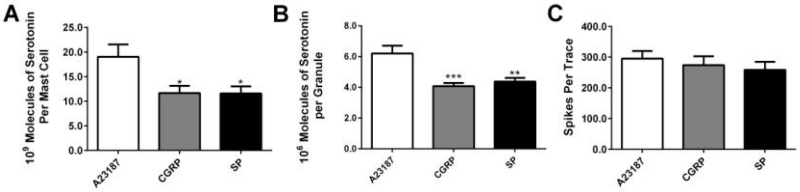

Figure 8.4 CFMA serotonin secretion and granule trafficking in response to neuropeptides and A23187. (A) Total amount of serotonin secreted per mast cell, (B) Amount of serotonin secreted per granule, as measured using CFMA, for each stimulation condition (C) Number of granules secreted per stimulation event, as measured using CFMA accounting for 10% coverage of cell by the electrode. *P≤0.05 ***P≤0.001 and ** P≤0.01 vs. A23187

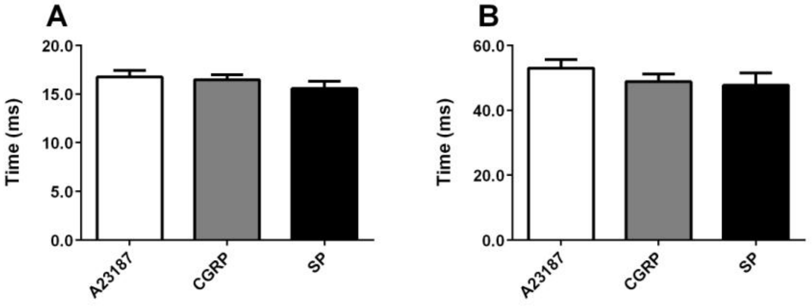

Figure 8.5 CFMA granule fusion pore kinetics in response to CGRP, SP, and A23187. T_{rise} (A) and $T_{1/2}$ (B) of the granule secretion events, as measured using CFMA, for each stimulation type. There is no statistical difference among the presented conditions.

secreted per granule rather than altered granule loading effects. The absence of spike number effects also suggests that the granule trafficking and/or docking machinery can be regulated independently of the processes that regulate the percentage of granular contents secreted during degranulation.

Decreased secretion of serotonin per granule could be a result of shorter granule fusion times if diffusion played the primary role in releasing serotonin upon granule fusion with the cell membrane. However, analysis of the kinetic parameters of mast cell degranulation following CGRP- and SP-stimulation reveal that the substantially smaller spike area values observed in the substance P- and CGRP-stimulated mast cells, compared to A23187 stimulation, were not associated with measureable differences in either spike half-width or spike rise-time (Fig. 8.5). Together, these findings indicate a remarkably simple mechanism of modulated mast cell degranulation that is largely characterized by a decreased fraction of the granule cargo secretion during exocytosis in the setting of neuropeptide stimulation compared to IgE-mediated mast cell degranulation.

8.4.5 Bulk and Single Cell Comparison

Previous findings have indicated decreased degranulation for TNP-Ova compared to ionophore-based stimulation, with anti-TNP-Ova inducing secretion of 79% of the serotonin secreted during A23187-induced degranulation on a single cell level.[6] For the current study, CGRP and SP each induced mast cell secretion equal to 61% of A23187 degranulation, therefore showing similar trends to the bulk cell level with CGRP/SP releasing less total serotonin than TNP-Ova stimulation. However, with similar stimulation concentrations (1μM SP or 1μM

CGRP), the bulk mast cells did not secrete measurable serotonin, whereas TNP-Ova stimulation induced significant chemical messenger secretion. The unexpected lack of degranulation is most likely due to the decreased amount of serotonin secretion per granule and that only a fraction of total mast cells degranulate following bulk exposure to CGRP and SP, which is not shown in the single cell data analysis.

8.5 Conclusion

The complex relationship between mast cells and peripheral nerve fibers is fundamental to the pathophysiology of many neurogenic inflammatory processes. [12-15] This work characterizes the direct stimulation of mast cell degranulation in response to both SP and CGRP, critical neurogenic inflammatory mediators, using both bulk assays and single-cell electrochemical approaches. Our findings indicate that SP and CGRP induce mast cell degranulation in a concentration- and IgE-dependent manner. The observed IgE effects suggest that mast cells may respond to neuropeptides more effectively in the absence of high levels of circulating IgE. Further work will be necessary to understand the signaling mechanisms that drive the decreased sensitivity to neuropeptide stimulation. Single cell analysis of SP- and CGRP-induced mast cell degranulation show that both neuropeptides induce a similar pattern of mast cell degranulation. Mast cell degranulation in response to SP or CGRP stimulation resulted in a similar granule secretion times and number of secretion events relative to A23187-stimulated control cells. This lack of variation in granule kinetics is consistent with the hypothesis that SP and CGRP activate mast cells through a similar mechanism.

Finally, when compared to previously reported findings,[6] the amount of serotonin secretion following both TNP-Ova and A23187 stimulation is greater than the amount secreted due to either SP or CGRP stimulation for both bulk and single cell degranulation. The percentage of TNP-Ova serotonin secretion caused by stimulation from SP and CGRP on a bulk cell level is significantly less than expected when compared to the releasate on a single cell level, likely due to the fact that single cell data only takes into account cells that have granule secretion, whereas bulk cell studies include the averaged behavior of all cells. Bulk assays may also be influenced by additional mechanisms such as serotonin re-uptake, giving the cells more control over their surroundings. [5] In conclusion, neurogenic inflammation is a highly complex process involving activation of mast cells by CGRP and SP, which can in return stimulate additional neurons. However, secretion in the bulk cell environment is decreased compared to single cell results and is dependent upon the IgE concentration the mast cells are exposed to.

Bibliography

Chapter 1

1. Galler, K., Brautgam, K., Popp, J., and Neugebauer, U. (2014) Making a big thing of a small cell-recent advances in single cell analysis, *Analyst 139*, 1237-1273.
2. Trouillon, R., Passarelli, M. K., Wang, J., Kurczy, M. E., and Ewing, A. G. (2013) Chemical Analysis of Single Cells, *Anal Chem 85*, 552-542.
3. Yin, H., and Marshall, D. (2012) Microfluidics for single cell analysis, *Curr Opin Biotechnol 23,* 110-119.
4. Zare, R. N., and Kim, S. (2010) Microfluidic platforms for single-cell analysis, *Annu Rev Biomed Eng 12*, 187-201.
5. Huang, N.T., Zhang, H.L., Chung, M.T., Seo, H. J., and Kurabayashi, K. (2014) Recent advancements in optofluidics-based single-cell analysis: optical on-chip cellular manipulation, treatment, and property detection, *Lab Chip 14*, 1230-1245.
6. Jung, S.K., Gorski, W., Aspinwall, C. A., Kauri, L. M., and Kennedy, R. T. (1999) Oxygen microsensor and its application to single cells and mouse pancreatic islets, *Anal Chem 71*, 3642-3649.
7. Amatore, C., Arbault, S., Guille, M., and Lemaitre, F. (2008) Electrochemical monitoring of single cell secretion: vesicular exocytosis and oxidative stress, *Chem Rev 108*, 2585-2621.
8. Actis, P., Tokar, S., Clausmeyer, J., Babakinejad, B., Mikhaleva, S., Cornut, R., Takahashi, Y., Lopez Cordoba, A., Novak, P., Shevchuck, A. I., Dougan, J. A., Kazarian, S. G., Gorelkin, P. V., Erofeev, A. S., Yaminsky, I. V., Unwin, P. R., Schuhmann, W., Klenerman, D., Rusakov, D. A., Sviderskaya, E. V., and Korchev, Y. E. (2014) Electrochemical nanoprobes for single-cell analysis, *ACS Nano 8*, 875-884.
9. Anderson, S. E., and Bau, H. H. (2015) Carbon nanoelectrodes for single-cell probing, *Nanotechnology 26,* doi: 10.1088/0957-4484/26/18/185101.
10. Adams, R. N. (1958) Carbon paste electrodes, *Anal Chem 30*, 1576.
11. Zoski, C. (2002) Ultramicroelectrodes: design, fabrication, and characterization, *Electroanalysis 14*, 1041-1051.
12. Yu, Y., Zhou, Y., Wu, L., Zhi, J., Yu, Y., Zhou, Y., Wu, L., and Zhi, J. (2012) Electrochemical biosensor based on boron-doped diamond electrodes with modified surfaces, *Int J of Electrochem2012,* 1-10.
13. Kim, D., Koseoglu, S., Manning, B. M., Meyer, A. F., and Haynes, C. L. (2011) Electroanalytical eavesdropping on single cell communication, *ACS Anal Chem 83*, 7242-7249.
14. Huffman, M. L., and Venton, B. J. (2009) Carbon-fiber microelectrodes for in vivo applications, *Analyst 134*, 18-24.
15. Ponchon, J. L., Cespuglio, R., Gonon, F., Jouvet, M., and Pujol, J. F. (1979) Normal pulse polarography with carbon fiber electrodes for in vitro and in vivo determination of catecholamines, *Anal chem 51*, 1483-1486.
16. Wightman, R. M., Jankowski, J. A., Kennedy, R. T., Kawagoe, K. T., Schroeder, T. J., Leszczyszyn, D. J., Near, J. A., Diliberto, E. J., Jr., and Viveros, O. H. (1991) Temporally resolved catecholamine spikes correspond to single vesicle release from individual chromaffin cells, *Proc Natl Acad Sci U S A 88*, 10754-10758.
17. Lugo-Morales, L. Z., Loziuk, P. L., Corder, A. K., Toups, J. V., Roberts, J. G., McCaffrey, K. A., and Sombers, L. A. (2013) Enzyme-modified carbon-fiber microelectrode for the

quantification of dynamic fluctuations of non-electroactive analytes using fast-scan cyclic voltammetry, *Anal Chem 85*, 8780-8786.

18. Tiwari, S., and Bijwe, J. (2014) Surface treatment of carbon fibers-a review, *Procedia Tech 14*, 505-512.
19. Kakhki, R. M. (2014) A review to recent developments in modification of carbon fiber electrodes, *Arabian J Chem*, 1-12.
20. Uchiyama, Y., Maxson, M. M., Sawada, T., Nakano, A., and Ewing, A. G. (2007) Phospholipid mediated plasticity in exocytosis observed in PC12 cells, *Brain Res 1151*, 46-54.
21. Ge, S., Woo, E., White, J. G., and Haynes, C. L. (2011) Electrochemical measurement of endogenous serotonin release from human blood platelets, *Anal Chem 83*, 2598-2604.
22. Marquis, B. J., and Haynes, C. L. (2008) The effects of co-culture of fibroblasts on mast cell exocytotic release characteristics as evaluated by carbon-fiber microelectrode amperometry, *Biophys Chem 137*, 63–69.
23. Koseoglu, S., Love, S. A., and Haynes, C. L. (2011) Cholesterol effects on vesicle pools in chromaffin cells revealed by carbon-fiber microelectrode amperometry, *Anal Bioanal Chem 400*, 2963-2971.
24. Ge, S., White, J. G., and Haynes, C. L. (2009) Quantal release of serotonin from platelets, *Anal Chem 81*, 2935-2943.
25. Ge, S. C., White, J. G., and Haynes, C. L. (2010) Critical role of membrane cholesterol in exocytosis revealed by single platelet study, *ACS Chem Biol 5*, 819-828.
26. Mundorf, M. L., and Wightman, R. M. (2002) Amperometry and cyclic voltammetry with carbon fiber microelectrodes at single cells, *Curr Protoc Neurosci*, 6.12.11-16.14.22.
27. Amos, A. N., Roberts, J. G., Qi, L., Sombers, L. A., and McCarty, G. S. (2014) Reducing the sampling rate of biochemical measurements using fast-scan cyclic voltammetry for in vivo applications, *IEEE Sens. J. 14*, 2975-2980.
28. Travis, E. R., and Wightman, R. M. (1998) Spatio-tempo resolution of exocytosis from individual cells, *Annu Rev Biophys Biomol Struct 27*, 77-103.
29. Kile, B.M., Walsh, P.L., McElligott, Z.A., Bucher, E.S., Guillot, T.S., Salahpour, A., Caron, M.G., and Wightman, M.R. (2012) Optimizing the temporal resolution of rast-scan cyclic voltammetry, *ACS Chem Neurosci 3*, 285-292.
30. Schmidt, A. C., Dunaway, L. E., Roberts, J. G., McCarty, G. S., and Sombers, L. A. (2014) Multiple scan rate voltammetry for selective quantification of real-time enkephalin dynamics, *Anal Chem 86*, 7806-7812.
31. Roberts, J. G., Toups, J. V., Eyualem, E., McCarty, G. S., and Sombers, L. A. (2013) An in situ electrode calibration strategy for voltammetric measurements in vivo, *Anal Chem 85*, 11568-11575.
32. Ge, S., Wittenberg, N. J., and Haynes, C. L. (2008) Quantitative and real-time detection of secretion of chemical messengers from individual platelets, *ACS Biochem 47*, 7020-7024.
33. Chen, T. K., Luo, G., and Ewing, A. G. (1994) Amperometric monitoring of stimulated catecholamine release from rat pheochromocytoma (PC12) cells at the zeptomole level, *ACS Anal Chem 66*, 3031-3035.
34. Cookson, E. A., Conte, I. L., Dempster, J., Hannah, M. J., and Carter, T. (2013) Characterisation of Weibel- Palade body fusion by amperometry in endothelial cells reveals fusion pore dynamics and the effect of cholesterol on exocytosis, *J Cell Sci 126*, 5490-5499.
35. Meunier, A., Bretou, M., Darchen, F., Collignon, M. G., Lemaitre, F., and Amatore, C. (2014) Amperometric detection of vesicular exocytosis from BON cells at carbon fiber microelectrodes, *Electrochim Acta 126*, 74-80.

36. Finkenstaedt-Quinn, S. F., Gruba, S. M., and Haynes, C. L. (2016) Variations in fusion pore formation in cholesterol-treated platelets, *Biophys. J. 110*, 922-929.
37. Li, X., Majdi, S., Dunevall, J., Fathali, H., and Ewing, A. G. (2015) Quantitative measurement of transmitters in individual vesicles in the cytoplasm of single cells with nanotip electrodes, *Angew Chem Int Ed Engl 54*, 11978-11982.
38. Omiatek, D. M., Dong, Y., Heien, M. L., and Ewing, A. G. (2010) Only a fraction of quantal content is released during exocytosis as revealed by electrochemical cytometry of secretory vesicles, *ACS Chem Neurosci 1*, 234-245.
39. Mellander, L. J., Trouillon, R., Svensson, M. I., and Ewing, A. G. (2012) Amperometric post spike feet reveal most exocytosis is via extended kiss-and-run fusion, *Sci Rep 2*, 1-6.
40. Van Kempen, G. T., VanderLeest, H. T., Van Den Berg, R. J., Eilers, P., and Westerink, R. H. (2011) Three distinct modes of exocytosis revealed by amperometry in neuroendocrine cells, *Biophys J 100*, 968-977.
41. Amatore, C., Arbault, S., Bonifas, I., and Guille, M. (2009) Quantitative investigations of amperometric spike feet suggest different controlling factors of the fusion pore in exocytosis at chromaffin cells, *Biophys Chem 143*, 124–131.
42. Koseoglu, S., Meyer, A. F., Kim, D., Meyer, B. M., Wang, Y., Dalluge, J. J., and Haynes, C. L. (2015) Analytical characterization of the role of phospholipids in platelet adhesion and secretion, *Anal Chem 87*, 413-421.
43. Manning, B. M., Meyer, A. F., Gruba, S. M., and Haynes, C. L. (2015) Single-cell analysis of mast cell degranulation induced by airway smooth muscle-secreted chemokines, *BBA 1850*, 1862-1868.
44. Manning, B. M., Hebbel, R. P., Gupta, K., and Haynes, C. L. (2012) Carbon-fiber microelectrode amperometry reveals sickle cell-induced inflammation and chronic morphine effects on single mast cells, *ACS Chem Biol 7*, 543-551.
45. Wang, C.W., Pan, C.Y., Wu, H.C., Shih, P.Y., Tsai, C.C., Liao, K.T., Lu, L.L., Hsieh, W.H., Chen, C.D., and Chen, Y.T. (2007) In situ detection of chromogranin A released from living neurons with a single walled carbon nanotube field effect transistor, *Small 3*, 1350-1355.
46. Tsai, C. C., Yang, C. C., Shih, P. Y., Wu, C. S., Chen, C. D., Pan, C. Y., and Chen, Y. T. (2008) Exocytosis of a single bovine adrenal chromaffin cell: the electrical and morphological studies, *J Phys Chem B 112*, 9165-9173.
47. Susloparova, A., Koppenhofer, D., Vu, X. T., Weil, M., and Ingebrandt, S. (2013) Impedance spectroscopy with field-effect transistor arrays for the analysis of anti-cancer drug action on individual cells, *Biosens Bioelectron 40*, 50-56.
48. Koppenhofer, D., Susloparova, A., Docter, D., Stauber, R. H., and Ingebrandt, S. (2013) Monitoring nanoparticle induced cell death in H441 cells using field-effect transistors, *Biosens Bioelectron 40*, 89-95.
49. Susloparova, A., Koppenhofer, D., Law, J. K., Vu, X. T., and Ingebrandt, S. (2015) Electrical cell-substrate impedance sensing with field-effect transistors is able to unravel cellular adhesion and detachment processes on a single cell level, *Lab Chip 15*, 668-679.
50. Zhang, Y., Clausmeyer, J., Babakinejad, B., Lopez Cordoba, A., Ali, T., Shevchuk, A., Takahashi, Y., Novak, P., Edwards, C., Lab, M., Gopal, S., Chiappini, C., Anand, U., Magnani, L., Coombes, R. C., Gorelik, J., Matsue, T., Schuhmann, W., Klenerman, D., Sviderskaya, E. V., and Korchev, Y. (2016) Spearhead nanometric field-effect transistor sensors for single-cell analysis, *ACS Nano 10*, 3214-3221.
51. Rituper, B., Gucek, A., Jorgacevski, J., Flasker, A., Kreft, M., and Zorec, R. (2013) High-resolution membrane capacitance measurements for the study of exocytosis and endocytosis, *Nat Protoc 8*, 1169-1183.

52. Homann, U., and Tester, M. (1998) Patch-clamp measurements of capacitance to study exocytosis and endocytosis, *Trends Plant Sci 3*, 110-114.
53. Dernick, G., Toledo, G. A. D., and Lindau, M. (2007) The patch amperometry technique: design of a method to study exocytosis of single vesicles, In *Electrochemical Methods for Neuroscience* (Michael, A. C., and Borland, L. M., Eds.), CRC Press/Taylor & Francis, Boca Raton FL.
54. Zhao, Y., Inayat, S., Dikin, D. A., Singer, J. H., Ruoff, R. S., and Troy, J. B. (2008) Patch clamp technique: review of the current state of the art and potential contributions from nanoengineering, *J of Nanoengineering and Nanosystems 222*, 1-11.
55. Kodandaramaiah, S. B., Franzesi, G. T., Chow, B. Y., Boyden, E. S., and Forest, C. R. (2012) Automated whole-cell patch-clamp electrophysiology of neurons in vivo, *Nat Methods 9*, 585-587.
56. Date, S., Mizuno, H., Tsuyama, N., Harada, T., and Masujima, T. (2012) Direct drug metabolism monitoring in a live single hepatic cell by video mass spectrometry, *Anal Sci 28*, 201-203.
57. Masujima, T. (2009) Live single-cell mass spectrometry, *Anal Sci 25*, 953-960.
58. Kuster, S. K., Fagerer, S. R., Verboket, P. E., Eyer, K., Jefimovs, K., Zenobi, R., and Dittrich, P. S. (2013) Interfacing droplet microfluidics with matrix-assisted laser desorption/ionization mass spectrometry: label-free content analysis of single droplets, *Anal Chem 85*, 1285-1289.
59. Aerts, J. T., Louis, K. R., Crandall, S. R., Govindaiah, G., Cox, C. L., and Sweedler, J. V. (2014) Patch clamp electrophysiology and capillary electrophoresis-mass spectrometry metabolomics for single cell characterization, *Anal Chem 86*, 3203-3208.
60. Fujii, T., Matsuda, S., Tejedor, M. L., Esaki, T., Sakane, I., Mizuno, H., Tsuyama, N., and Masujima, T. (2015) Direct metabolomics for plant cells by live single-cell mass spectrometry, *Nat Protoc 10*, 1445-1456.
61. Zavalin, A., Todd, E. M., Rawhouser, P. D., Yang, J., Norris, J. L., and Caprioli, R. M. (2012) Direct imaging of single cells and tissue at sub-cellular spatial resolution using transmission geometry MALDI MS, *J Mass Spectrom 47*, 1473-1481.
62. Passarelli, M. K., and Winograd, N. (2011) Lipid imaging with time-of-flight secondary ion mass spectrometry (ToF-SIMS), *BBA 1811*, 976-990.
63. Passarelli, M. K., and Ewing, A. G. (2013) Single-cell imaging mass spectrometry, *Curr Opin Chem Biol 17*, 854-859.
64. Klitzing, H. A., Weber, P. K., and Kraft, M. L. (2013) Secondary ion mass spectrometry imaging of biological membranes at high spatial resolution, *Methods Mol Biol 950*, 483-501.
65. Park, J. W., Jeong, H., Kang, B., Kim, S. J., Park, S. Y., Kang, S., Kim, H. K., Choi, J. S., Hwang, D., and Lee, T. G. (2015) Multi-dimensional TOF-SIMS analysis for effective profiling of disease-related ions from the tissue surface, *Sci Rep 5*, 11077.
66. Hanrieder, J., Malmberg, P., Lindberg, O. R., Fletcher, J. S., and Ewing, A. G. (2013) Time-of-flight secondary ion mass spectrometry based molecular histology of human spinal cord tissue and motor neurons, *Anal Chem 85*, 8741-8748.
67. Bloom, A., and Winograd, N. (2014) Dye-enhanced imaging of mammalian cells with SIMS, *Surf Interface Anal 46*, 177-180.
68. Bloom, A. N., Tian, H., and Winograd, N. (2016) C60-SIMS imaging of nanoparticles within mammalian cells, *Biointerphases 11*.
69. Tarolli, J. G., Jackson, L. M., and Winograd, N. (2014) Improving secondary ion mass spectrometry image quality with image fusion, *J Am Soc Mass Spectrom 25*, 2154-2162.

70. Carlred, L., Gunnarsson, A., Sole-Domenech, S., Johansson, B., Vukojevic, V., Terenius, L., Codita, A., Winblad, B., Schalling, M., Hook, F., and Sjovall, P. (2014) Simultaneous imaging of amyloid-beta and lipids in brain tissue using antibody-coupled liposomes and time-of-flight secondary ion mass spectrometry, *J Am Chem Soc 136*, 9973-9981.
71. Spengler, B., and Hubert, M. (2002) Scanning microprobe matrix-assisted laser desorption ionization (SMALDI) mass spectrometry: instrumentation for sub-micrometer resolved LDI and MALDI surface analysis, *J Am Soc Mass Spectrom 13*, 735-748.
72. Boggio, K. J., Obasuyi, E., Sugino, K., Nelson, S. B., Agar, N. Y., and Agar, J. N. (2011) Recent advances in single-cell MALDI mass spectrometry imaging and potential clinical impact, *Expert Rev Proteomics 8*, 591-604.
73. Xie, W., Gao, D., Jin, F., Jiang, Y., and Liu, H. (2015) Study of phospholipids in single cells using an integrated microfluidic device combined with matrix-assisted laser desorption/ionization mass spectrometry, *Anal Chem 87*, 7052-7059.
74. Phelps, M. S., Sturtevant, D., Chapman, K. D., and Verbeck, G. F. (2016) Nanomanipulation-coupled matrix-assisted laser desorption/ ionization-direct organelle mass spectrometry: a technique for the detailed analysis of single organelles, *J Am Soc Mass Spectrom 27*, 187-193.
75. Wong, M. T., Chen, J., Narayanan, S., Lin, W., Anicete, R., Kiaang, H. T., De Lafaille, M. A., Poidinger, M., and Newell, E. W. (2015) Mapping the diversity of follicular helper T cells in human blood and tonsils using high-dimensional mass cytometry analysis, *Cell Rep 11*, 1822-1833.
76. Bendall, S. C., Nolan, G. P., Roederer, M., and Chattopadhyay, P. K. (2012) A deep profiler's guide to cytometry, *Trends Immunol 33*, 323-332.
77. Gaudilliere, B., Ganio, E. A., Tingle, M., Lancero, H. L., Fragiadakis, G. K., Baca, Q. J., Aghaeepour, N., Wong, R. J., Quaintance, C., El-Sayed, Y. Y., Shaw, G. M., Lewis, D. B., Stevenson, D. K., Nolan, G. P., and Angst, M. S. (2015) Implementing mass cytometry at the bedside to study the immunological basis of human diseases: distinctive immune features in patients with a history of term or preterm birth, *Cytometry Part A 87*, 817-829.
78. Leipold, M. D., Ornatsky, O., Baranov, V., Whitfield, C., and Nitz, M. (2011) Development of mass cytometry methods for bacterial discrimination, *Anal Biochem 419*, 1-8.
79. Giesen, C., Wang, H. A., Schapiro, D., Zivanovic, N., Jacobs, A., Hattendorf, B., Schuffler, P. J., Grolimund, D., Buhmann, J. M., Brandt, S., Varga, Z., Wild, P. J., Gunther, D., and Bodenmiller, B. (2014) Highly multiplexed imaging of tumor tissues with subcellular resolution by mass cytometry, *Nat Methods 11*, 417-422.
80. Schermelleh, L., Heintzmann, R., and Leonhardt, H. (2010) A guide to super-resolution fluorescence microscopy, *J Cell Biol 190*, 165-175.
81. Lippincott-Schwartz, J. (2015) Profile of Eric Betzig, Stefan Hell, and W. E. Moerner, 2014 Nobel Laureates in Chemistry, *PNAS 112*, 2630-2632.
82. Olshausen, P. V., Defeu Soufo, H. J., Wicker, K., Heintzmann, R., Graumann, P. L., and Rohrbach, A. (2013) Superresolution imaging of dynamic MreB filaments in B. subtilis-a multiple-motor-driven transport?, *Biophys J 105*, 1171-1181.
83. Honigmann, A., Mueller, V., Ta, H., Schoenle, A., Sezgin, E., Hell, S., and Eggeling, C. (2014) Scanning STED-FCS reveals spatiotemporal heterogeneity of lipid interaction in the plasma membrane of living cells, *Nat. Commun. 5*.
84. Wilmes, S., Staufenbiel, M., Lisse, D., Richter, C. P., Beutel, O., Busch, K. B., Hess, S. T., and Piehler, J. (2012) Triple-color super-resolution imaging of live cells: resolving submicroscopic receptor organization in the plasma membrane, *Angew Chem Int Ed Engl 51*, 4868-4871.

85. Paar, M., Jüngst, C., Steiner, N. A., Magnes, C., Sinner, F., Kolb, D., Lass, A., Zimmermann, R., Zumbusch, A., Kohlwein, S. D., and Wolinski, H. (2012) Remodeling of lipid droplets during lipolysis and growth in adipocytes, *J Biol Chem 287*, 11164-11173.
86. Potcoava, M. C., Futia, G. L., Aughenbaugh, J., Schlaepfer, I. R., and Gibson, E. A. (2014) Raman and coherent anti-stokes Raman scattering microscopy studies of changes in lipid content and composition in hormone-treated breast and prostate cancer cells, *J Biomed Op 19*, 111605.

Chapter 2

1. Salaun, C., James, D. J., and Chamberlain, L. H. (2004) Lipid rafts and the regulation of exocytosis, *Traffic 5*, 255-264.
2. Ge, S. C., White, J. G., and Haynes, C. L. (2010) Critical role of membrane cholesterol in exocytosis revealed by single platelet study, *ACS Chem Biol 5*, 819-828.
3. Wang, N., Kwan, C., Gong, X., de Chaves, E. P., Tse, A., and Tse, F. W. (2010) Influence of cholesterol on catecholamine release from the fusion pore of large dense core chromaffin granules, *J Neurosci 30*, 3904-3911.
4. Wightman, R. M., and Haynes, C. L. (2004) Synaptic vesicles really do kiss and run, *Nature Neurosci 7*, 321-322.
5. Omiatek, D. M., Dong, Y., Heien, M. L., and Ewing, A. G. (2010) Only a fraction of quantal content is released during exocytosis as revealed by electrochemical cytometry of secretory vesicles, *ACS Chem Neurosci 1*, 234-245.
6. Mellander, L. J., Trouillon, R., Svensson, M. I., and Ewing, A. G. (2012) Amperometric post spike feet reveal most exocytosis is via extended kiss-and-run fusion, *Sci Rep 2*.
7. Mellander, L. J., Kurczy, M. E., Najafinobar, N., Dunevall, J., Ewing, A. G., and Cans, A. S. (2014) Two modes of exocytosis in an artificial cell, *Sci Rep 4*.
8. Cabeza, J. M., Acosta, J., and Alés, E. (2013) Mechanisms of granule membrane recapture following exocytosis in intact mast cells, *J of Biol Chem 288*, 20293-20305.
9. Staal, R. G., Mosharov, E. V., and Sulzer, D. (2004) Dopamine neurons release transmitter via a flickering fusion pore, *Nat Neurosci 7*, 341-346.
10. White, J. (2007) Platelet Structure, In *Platelets* (Michelson, A., Ed.) 2 ed., pp 45-74, Academic/Elsevier, Amsterdam.
11. Ge, S., White, J. G., and Haynes, C. L. (2009) Quantal release of serotonin from platelets, *Anal Chem 101*, 2351-2359.
12. Ge, S., Wittenberg, N. J., and Haynes, C. L. (2008) Quantitative and real-time detection of secretion of chemical messengers from individual platelets, *Biochemistry 47*, 7020-7024.
13. Gruba, S. M., Koseoglu, S., Meyer, A. F., Meyer, B. M., Maurer-Jones, M. A., and Haynes, C. L. (2015) Platelet membrane variations and their effects on delta-granule secretion kinetics and aggregation spreading among different species, *BBA-Biomemb 1848*, 1609-1618.
14. Amatore, C., Arbault, S., Bonifas, I., and Guille, M. (2009) Quantitative investigations of amperometric spike feet suggest different controlling factors of the fusion pore in exocytosis at chromaffin cells, *Biophys Chem 143*, 124–131.
15. Cookson, E. A., Conte, I. L., Dempster, J., Hannah, M. J., and Carter, T. (2013) Characterisation of Weibel- Palade body fusion by amperometry in endothelial cells

reveals fusion pore dynamics and the effect of cholesterol on exocytosis, *J Cell Sci 126*, 5490-5499.

16. Hochgraf, E., Levy, Y., Aviram, M., Brook, J. G., and Cogan, U. (1994) Lovastatin decreases plasma and platelet cholesterol levels and normalized elevated platelet fluidity and aggregation in hypercholesterolemic patients, *Metab 43*, 11-17.
17. Lijnen, P., Echevaria-Vazquez, D., and Petrov, V. (1996) Influence of cholesterol-lowering on plasma membrane lipids and function, *Meth Find Exp Clin Pharmacol 18*, 123-136.
18. Shattil, S. J., Anaya-Galindo, R., Bennett, J., Colman, R. W., and Cooper, R. A. (1975) Platelet hypersensitivity induced by cholesterol incorporation., *J Clin Invest 55*, 636-643.
19. Grgurevich, S., Krishnan, R., White, M. M., and Jennings, L. K. (2003) Role of in vitro cholesterol depletion in mediating human platelet aggregation, *J Thromb Haemost 1*, 576-586.

Chapter 3

1. Flaumenhaft, R. (2003) Molecular basis of platelet granule secretion, *Arterioscler Thromb Vasc Biol 23*, 1152-1160.
2. Omori, T., Mihara, H., Kurihara, T., and Esaki, N. (2010) The distribution of phosphatidyl-D-serine in the rat, *Biosci Biotech and Biochem 74*, 1953-1955.
3. Heemskerk, J., Bevers, E., and Lindhout, T. (2002) Platelet activation and blood coagulation, *Thromb Haemost 88*, 186-193.
4. Zwaal, R.F., Comfurius, P., and Bevers, E. (1998) Lipid-protein interactions in blood coagulation, *BBA-Reviews on Biomemb 1376*, 433-453.
5. Zwaal, R. F., Comfurius, P., and Van Deenen, L. L. (1977) Membrane asymmetry and blood coagulation, *Nature 268*, 358-360.
6. Fadok, V. A., Savill, J. S., Haslett, C., Bratton, D. L., Doherty, D. E., Campbell, P. A., and Henson, P. M. (1992) Different populations of macrophages use either the vitronectin receptor or the phosphatidylserine receptor to recognize and remove apoptotic cells, *J of Immunol 149*, 4029-4035.
7. Martin, S. J., Reutelingsperger, C. P. M., McGahon, A. J., Rader, J. A., Vanschie, R., Laface, D. M., and Green, D. R. (1995) Early redistribution of plasma-membrane phosphatidylserine is a general feature of apoptosis regardelss of the initiating stimulus-inhibition by overexpression of BCL-2 and ABL, *J of Exp Med 182*, 1545-1556.
8. Bennett, M. R., Gibson, D. F., Schwartz, S. M., and Tait, J. F. (1995) Binding and phagocytosis or apoptotic vascular smooth-muscle cells is mediated in part by exposure of phosphatidylserine, *Circ Res 77*, 1136-1142.
9. Casciolarosen, L. A., Anhalt, G. J., and Rosen, A. (1995) DNA-dependent protein-kinase is one of a subset of autoantigens specifically cleaved early during apoptosis, *J Exp Med 182*, 1625-1634.
10. Tanaka, Y., and Schroit, A. J. (1983) Insertion of fluorescent phosphatidylserine into the plasma-membrane of red-blood-cells- recognition by autologous macrophages, *J Biol Chem 258*, 1335-1343.
11. Schroit, A. J., Madsen, J. W., and Tanaka, Y. (1985) Invivo recognition and clearance of red blood-cells containing phosphatidylserine in their plasma-membranes, *J Biol Chem 260*, 5131-5138.

12. Fadok, V. A., Voelker, D. R., Campbell, P. A., Cohen, J. J., Bratton, D. L., and Henson, P. M. (1992) Exposure of phosphatidylserine on the surface of apoptoticlymphocytes triggers specific recognition and removal by macrophages, *J Immunol 148*, 2207-2216.
13. Fadok, V. A., Laszlo, D. J., Noble, P. W., Weinstein, L., Riches, D. W. H., and Henson, P. M. (1993) Particle digestibility is required for induction of the phosphatidylserine recognition mechanism used by murine macrophages to phagocytose apoptotic cells, *J Immunol 151*, 4274-4285.
14. Koseoglu, S., Meyer, A. F., Kim, D., Meyer, B. M., Wang, Y., Dalluge, J. J., and Haynes, C. L. (2015) Analytical characterization of the role of phospholipids in platelet adhesion and secretion, *Anal Chem 87*, 413-421.
15. Gruba, S. M., Koseoglu, S., Meyer, A. F., Meyer, B. M., Maurer-Jones, M. A., and Haynes, C. L. (2015) Platelet membrane variations and their effects on delta-granule secretion kinetics and aggregation spreading among different species, *BBA-Biomemb 1848*, 1609-1618.
16. Meyer, A. F., Thompson, J. T., Wang, Y., Koseoglu, S., Haynes, C. L., and Dalluge, J. J. (2013) Isotope-dilution UPLC-MS/MS determination of mast cell-secreted bioactive lipids, *Analyst 138*, 5697-5705.
17. Blank, U., and Rivera, J. (2006) Assays for regulated exocytosis of mast cells, In *Current Protocols in Cell Biology*, John Wiley & Sons, Inc.
18. Kim, D., Lin, Y. S., and Haynes, C. L. (2011) On-chip evaluation of shear stress effect on cytotoxicity of mesoporous silica nanoparticles, *ACS Anal Chem 83*, 8377-8382.
19. Bach, D., and Wachtel, E. (2003) Phospholipid/cholesterol model membranes: formation of cholesterol crystallites, *BBA-Biomemb 1610*, 187-197.
20. Tandon, N., Harmon, J.T., Rodbard, D., and Jamieson, G.A. (1983) Thrombin receptors define responsiveness of cholesterol-modified platelets, *J Biol Chem 258, 11840-11845.*

Chapter 4

1. Saito, H., Matsushita, T., Yamamoto, K., Kojima, T., and Kunishima, S. (2005) Giant platelet syndrome, *Hematol 10*, 41-46.
2. Baldini, M. G. (1972) Nature of the platelet defect in the Wiskott-Aldrich syndrome, *Annals of the New York Academy of Sciences 201*, 437-444.
3. Zwaal, R. F. A., Comfurius, P., and Bevers, E. M. (2004) Scott syndrome, a bleeding disorder caused by defective scrambling of membrane phospholipids, *BBA-Molec and Cell Biol of Lipids 1636*, 119-128.
4. Gader, A. G., Ghumlas, A. K., Hussain, M. F., Haidari, A. A., and White, J. G. (2008) The ultrastructure of camel blood platelets: a comparative study with human, bovine, and equine cells, *Platelets 19*, 51-58.
5. Pelagalli, A., Belisario, M. A., Tafuri, S., Lombardi, P., d'Angelo, D., Avallone, L., and Staiano, N. (2003) Adhesive properties of platelets from different animal species, *J Comp Pathol 128*, 127-131.
6. Choi, W., Karim, Z. A., and Whiteheart, S. W. (2010) Protein expression in platelets from six species that differ in their open canalicular system, *Platelets 21*, 167-175.
7. White, J. G. (1999) Platelet membrane interactions, *Platelets 10*, 368-381.
8. White, J. (2007) Platelet Structure, In *Platelets* (Michelson, A., Ed.) 2 ed., pp 45-74, Academic/Elsevier, Amsterdam.

9. White, J. G. (2000) Platelet secretion during clot retraction, *Platelets 11*, 331-343.
10. Hikasa, Y., Masuda, K., Asakura, Y., Yamashita, Y., Sato, C., Kamio, M., Miura, A., Taniguchi, T., and Minamizuru, N. (2013) Identification and characterization of platelet alpha(2)-adrenoceptors and imidazoline receptors in rats, rabbits, cats, dogs, cattle, and horses, *Eur J Pharmacol 720*, 363-375.
11. Ge, S., Koseoglu, S., and Haynes, C. L. (2010) Bioanalytical tools for single-cell study of exocytosis, *Anal Bioanal Chem 397*, 3281-3304.
12. Ge, S., Wittenberg, N. J., and Haynes, C. L. (2008) Quantitative and real-time detection of secretion of chemical messengers from individual platelets, *Biochemistry 47*, 7020-7024.
13. Ge, S., White, J. G., and Haynes, C. L. (2009) Quantal release of serotonin from platelets, *Anal Chem 101*, 2351-2359.
14. Ge, S. C., White, J. G., and Haynes, C. L. (2010) Critical role of membrane cholesterol in exocytosis revealed by single platelet study, *ACS Chem Biol 5*, 819-828.
15. Gruba, S. M., Meyer, A. F., Manning, B. M., Wang, Y., Thompson, J. W., Dalluge, J. J., and Haynes, C. L. (2014) Time- and concentration-dependent effects of exogenous serotonin and inflammatory cytokines on mast cell function, *ACS Chem Biol 9*, 503-509.
16. (2004) *Platelets and megakaryocytes: Volume 1. functional assays*, Humana Press Inc, Towowa, NJ.
17. Koseoglu, S., Meyer, A. F., Kim, D., Meyer, B. M., Wang, Y., Dalluge, J. J., and Haynes, C. L. (2015) Analytical characterization of the role of phospholipids in platelet adhesion and secretion, *Anal Chem 87*, 413-421.
18. Rainville, P. D., Stumpf, C. L., Shockcor, J. P., Plumb, R. S., and Nicholson, J. K. (2007) Novel application of reversed-phase UPLC-oaTOF-MS for lipid analysis in complex biological mixtures: a new tool for lipidomics, *J Proteome Res 6*, 552-558.
19. Ammar, M. R., Kassas, N., Chasserot-Golaz, S., Bader, M.-F., and Vitale, N. (2013) Lipids in regulated exocytosis: what are they doing?, *Frontiers Endocrinol 4*, 125-125.
20. Churchward, M. A., and Coorssen, J. R. (2009) Cholesterol, regulated exocytosis and the physiological fusion machine, *Biochem J 423*, 1-14.
21. Salaun, C., James, D. J., and Chamberlain, L. H. (2004) Lipid rafts and the regulation of exocytosis, *Traffic 5*, 255-264.
22. Dennison, S. M., Bowen, M. E., Brunger, A. T., and Lentz, B. R. (2006) Neuronal SNAREs do not trigger fusion between synthetic membranes but do promote PEG-mediated membrane fusion, In *Biophys J*, pp 1661-1675.
23. White, J. G. (1987) The secretory pathway of bovine platelets, *Blood 69*, 878-885.
24. Omiatek, D. M., Dong, Y., Heien, M. L., and Ewing, A. G. (2010) Only a fraction of quantal content is released during exocytosis as revealed by electrochemical cytometry of secretory vesicles, *ACS Chem Neurosci 1*, 234-245.
25. Kim, D., Koseoglu, S., Manning, B. M., Meyer, A. F., and Haynes, C. L. (2011) Electroanalytical eavesdropping on single cell communication, *ACS Anal Chem 83*, 7242-7249.
26. Amatore, C., Bouret, Y., Travis, E. R., and Wightman, R. M. (2000) Interplay between membrane dynamics, diffusion and swelling pressure governs individual vesicular exocytotic events during release of adrenaline by chromaffin cells, *Biochimie 82*, 481-496.
27. Koseoglu, S., Love, S. A., and Haynes, C. L. (2011) Cholesterol effects on vesicle pools in chromaffin cells revealed by carbon-fiber microelectrode amperometry, *Anal Bioanal Chem 400*, 2963-2971.

28. Feng, D., Crane, K., Rozenvayn, N., Dvorak, A. M., and Flaumenhaft, R. (2002) Subcellular distribution of 3 functional platelet SNARE proteins: human cellubrevin, SNAP-23, and syntaxin 2, *Blood 99*, 4006-4014.
29. Grouse, L. H., Rao, G. H., Weiss, D. J., Perman, V., and White, J. G. (1990) Surface-activated bovine platelets do not spread, they unfold, *Am J Pathol 136*, 399-408.
30. Pike, L. J., Han, X., Chung, K. N., and Gross, R. W. (2002) Lipid rafts are enriched in arachidonic acid and plasmenylethanolamine and their composition is independent of caveolin-1 expression: a quantitative electrospray ionization/mass spectrometric analysis, *Biochem 41*, 2075-2088.
31. Peters, C. G., Michelson, A. D., and Flaumenhaft, R. (2012) Granule exocytosis is required for platelet spreading: differential sorting of alpha-granules expressing VAMP-7, *Blood 120*, 199-206.

Chapter 5

1. National Institute of Health. (2003) National institutes of health state-of-the-science conference statement: symptom management in cancer: pain, depression, and fatigue, July 15–17, 2002, *JNCI 95*, 1110-1117.
2. A.G.S. Panel. (2002) The management of persistent pain in older persons, *J Am Geriatr Soc 50*, S205-224.
3. Smith, H. S. (2009) Opioid metabolism, *Mayo Clinic Proceedings 84*, 613-624.
4. Governale, L. (2010) Outpatient prescription opioid utilization in the U.S., years 2000-2009, *U.S. Food and Drug Administration*.
5. Walker, D. H., Evans, C., and Henderson, L. (2009) Treatment episode data set (TEDS) 1997-2007, Department of Health and Human Services.
6. Smith, H. S. (2011) The Metabolism of opioid agents and the clinical impact of their active metabolites, *Clinic J of Pain 27*, 824-838.
7. Farr, S. J., and Otulana, B. A. (2006) Pulmonary delivery of opioids as pain therapeutics, *Adv Drug Deliv Rev 58*, 1076-1088.
8. Pathan, H., and Williams, J. (2012) Basic opioid pharmacology: an update, *Br J Pain 6*, 11-16.
9. Cachia, E., and Ahmedzai, S. H. (2011) Transdermal opioids for cancer pain, *Current opinion in supportive and palliative care 5*, 15-19.
10. Dhawan, B., Cesselin, F., Raghubir, R., Reisine, T., Bradley, P., Portoghese, P., and Hamon, M. (1996) International union of pharmacology. XII. classification of opioid receptors, *Pharmacol Rev 48*, 567-592.
11. Kieffer, B. L. (1999) Opioids: first lessons from knockout mice, *Trends Pharmacol Sci 20*, 19-26.
12. Manning, B. M., Hebbel, R. P., Gupta, K., and Haynes, C. L. (2012) Carbon-fiber microelectrode amperometry reveals sickle cell-induced inflammation and chronic morphine effects on single mast cells, *ACS Chem Biol 7*, 543-551.
13. Vallejo, R., De Leon-Casasola, O., and Benyamin, R. (2004) Opioid therapy and immunosuppression: a review, *Am J Ther 11*, 354-365.
14. Bidlack, J. M. (2000) Detection and function of opioid receptors on cells from the immune system, *Clin Diagn Lab Immunol 7*, 719-723.
15. White, J. (2007) Platelet structure, In *Platelets* (Michelson, A., Ed.) 2 ed., pp 45-74, Academic/Elsevier, Amsterdam.

16. Reed, G. (2007) Platelet secretion, In *Platelets* (Michelson, A., Ed.) 2 ed., pp 309-318, Academic/Elsevier, Amsterdam.
17. Gotta A. W. Gould, P. S., C.A. Goldiner, P. (1980) The effect of enflurane and fentanyl anaesthesia on human platelet aggregation in vivo, *Can. Anaest. Soc J 27*, 319-322.
18. Kozek-Langenecker, S. A. (2002) The effects of drugs used in anaesthesia on platelet membrane receptors and on platelet function, *Curr Drug Targets 3*, 247-258.
19. Gibbs, N. M. (1991) The effect of anesthetic agents on platelet function, *Anaesth Intensive Care 19*, 495-520.
20. Mehrishi, J. N. M., Ivor. (1983) Opiate receptors on lymphocytes and platelets in man, *Clin Immunol Immunopathol 27*, 240–249.
21. Gruba, S. M., Koseoglu, S., Meyer, A. F., Meyer, B. M., Maurer-Jones, M. A., and Haynes, C. L. (2015) Platelet membrane variations and their effects on delta-granule secretion kinetics and aggregation spreading among different species, *BBA-Biomemb 1848*, 1609-1618.
22. Gruba, S. M., Meyer, A. F., Manning, B. M., Wang, Y., Thompson, J. W., Dalluge, J. J., and Haynes, C. L. (2014) Time- and concentration-dependent effects of exogenous serotonin and inflammatory cytokines on mast cell function, *ACS Chem Biol 9*, 503-509.
23. Blank, U., and Rivera, J. (2006) Assays for regulated exocytosis of mast cell granules. *In Current Protoc Cell Biol*, John Wiley & Sons, Inc.
24. Kim, D., Lin, Y. S., and Haynes, C. L. (2011) On-chip evaluation of shear stress effect on cytotoxicity of mesoporous silica nanoparticles, *ACS Anal Chem 83*, 8377-8382.
25. Koseoglu, S., Meyer, A. F., Kim, D., Meyer, B. M., Wang, Y., Dalluge, J. J., and Haynes, C. L. (2015) Analytical characterization of the role of phospholipids in platelet adhesion and secretion, *Anal Chem 87*, 413-421.
26. (2004) *Platelets and megakaryocytes: Volume 1. functional assays*, Humana Press Inc, Towowa, NJ.
27. Zucker, M. B., Nachmias, V.T. (1985) Platelet activation, *Arteriosclerosis 5*, 2-18.
28. Scharf, R. E. (2012) Drugs that affect platelet function, *Semin Thromb and Hemost 38*, 865-883.
29. Ge, S. C., White, J. G., and Haynes, C. L. (2010) Critical role of membrane cholesterol in exocytosis revealed by single platelet study, *ACS Chem Biol 5*, 819-828.
30. Finkenstaedt-Quinn, S. F., Gruba, S. M., and Haynes, C. L. (2016) Variations in fusion pore formation in cholesterol-treated platelets, *Biophys. J. 110*, 922-929.
31. Cramer, E. M., and Fontenay, M. (2006) *Platelets: structure related to function*, 5th ed.
32. Stenberg, P. E., Barrie, R. J., Pestina, T. I., Steward, S. A., Arnold, J. T., Murti, A. K., Hutson, N. K., and Jackson, C. W. (1998) Prolonged bleeding time with defective platelet filopodia formation in the Wistar Furth rat, *Blood 91*, 1599-1608.
33. Brass, L. F., Tomaiuolo, M., Stalker, and J., T. (2013) Harnessing the platelet signaling network to produce an optimal hemostatic response, *Hematol Oncol Clin North Am 27*, 381-409.

Chapter 6

1. CDC. (2012) National health interview survey (NHIS) data: 2011 lifetime and current asthma, (U.S. Deparment of Health and Human Services), Atlanta Georgia.
2. Manning, B. M., Meyer, A. F., Gruba, S. M., and Haynes, C. L. (2015) Single-cell analysis of mast cell degranulation induced by airway smooth muscle-secreted chemokines, *BBA 1850*, 1862-1868.
3. Hershenson, M. B., Brown, M., Camoretti-Mercado, B., and Solway, J. (2008) Airway smooth muscle in asthma, *Annu Rev Pathol Mech Dis 3*, 523-555.
4. John, M., Hirst, S. J., Jose, P. J., Robichaud, A., Berkman, N., Witt, C., Twort, C. H., Barnes, P. J., and Chung, K. F. (1997) Human airway smooth muscle cells express and release RANTES in response to T helper 1 cytokines: regulation by T helper 2 cytokines and corticosteroids, *J Immunol 158*, 1841-1847.
5. Brightling, C. E., Ammit, A. J., Kaur, D., Black, J. L., Wardlaw, A. J., Hughs, J. M., and Bradding, P. (2005) The CXCL10/CXCR3 axis mediates human lung mast cell migration to asthmatic airway smooth muscle, *Am J Respir Crit Care Med 171*, 1103-1108.
6. Sauty, A., Dziejman, M., Taha, R. A., Iarossi, A. S., Neote, K., Garcia-Zepeda, E. A., Hamid, Q., and Luster, A. D. (1999) The T cell-specific CXC chemokines IP-10, Mig, and I-TAC are expressed by activated human bronchial epithelial cells, *J Immunol 162*, 3549-3558.
7. Yeganeh, B., Xia, C., Movassagh, H., Koziol-White, C., Chang, Y., Al-Alwan, L., Bourke, J. E., and Oliver, B. G. (2013) Emerging mediators of airway smooth muscle dysfunction in asthma, *Pulm Pharmacol Ther 26*, 105-111.
8. Alrashdan, Y. A., Alkhouri, H., Chen, E., Lalor, D. J., Poniris, M., Henness, S., Brightling, C. E., Burgess, J. K., Armour, C. L., Ammit, A. J., and Hughes, J. M. (2012) Asthmatic airway smooth muscle CXCL10 production: mitogen-activated protein kinase JNK involvement, *Am J Physiol Lung Cell Mol Physiol 302*, 1118-1127.
9. Pitchford, S. C., Momi, S., Baglioni, S., Casali, L., Giannini, S., Rossi, R., Page, C. P., and Gresele, P. (2008) Allergen induces the migration of platelets to lung tissue in allergic asthma, *Am J Resp Crit Care Med 177*, 604-612.
10. Joseph, M., Gounni, A. S., Kusnierz, J. P., Vorng, H., Sarfati, M., Kinet, J. P., Tonnel, A. B., Capron, A., and Capron, M. (1997) Expression and functions of the high-affinity IgE receptor on human platelets and megakaryocyte precursors, *Eur J Immunol 27*, 2212-2218.
11. Hasegawa, S., Pawankar, R., Suzuki, K., Nakahata, T., Furukawa, S., Okumura, K., and Ra, C. (1999) Functional expression of the high affinity receptor for IgE (FceRI) in human platelets and its' intracellular expression in human megakaryocytes, *Blood 93*, 2543-2551.
12. White, J. (2007) Platelet Structure, In *Platelets* (Michelson, A., Ed.) 2 ed., pp 45-74, Academic/Elsevier, Amsterdam.
13. Blair, P., and Flaumenhaft, R. (2009) Platelet α-granules: basic biology and clinical correlates, *Blood Rev 23*, 177–189.
14. Pitchford, S. C., Yano, H., Lever, R., Riffo-Vasquez, Y., Ciferri, S., Rose, M. J., Giannini, S., Momi, S., Spina, D., O'Connor, B., Gresele, P., and Page, C. P. (2003) Platelets are essential for leukocyte recruitment in allergic inflammation, *J Allergy Clin Immunol 112*, 109-118.
15. Henn, V., Slupsky, J. R., Grafe, M., Anagnostopoulos, I., Forster, R., Muller-Berghaus, G., and Kroczek, R. A. (1998) CD40 ligand on activated platelets triggers an inflammatory reaction of endothelial cells, *Nature 391*, 591-594.

16. Pitchford, S. C., Momi, S., Giannini, S., Casali, L., Spina, D., Page, C. P., and Gresele, P. (2005) Platelet P-selectin is required for pulmonary eosinophil and lymphocyte recruitment in a murine model of allergic inflammation, *Blood 105*, 2074-2081.
17. Morley, J., Sanjar, S., and Page, C. P. (1984) The platelet in asthma, *The Lancet*, 1142-1143.
18. Knauer, K. A., Lichtenstein, L. M., Adkinson, N. F., and Fish, J. E. (1981) Platelet activation during antigen-induced airway reactions in asthmatic subjects, *NEJM 304*, 1404-1407.
19. Tian, J., Zhu, T., Juan, L., Guo, Z., and Cao, X. (2015) Platelets promote allergic asthma through the expression of CD154, *Cell Mol Bio 12*, 700-707.
20. Pitchford, S. C., and Page, C. P. (2006) Platelet activation in asthma: integral to the inflammatory response, *Clin Exp Allergy 36*, 399-401.
21. Benton, A. S., Kumar, N., Lerner, J., Wiles, A., Foerster, M., Teach, S. J., and Freishtat, R. J. (2010) Airway platelet activation is associated with airway eosinophilic inflammation in asthma, *J Investig Med 58*, 987-990.
22. Coyle, A. J., Page, C. P., Atkinson, L., Flanagan, R., and Metzger, W. J. (1990) The requirement for platelets in allergen-induced late asthmatic airway obstruction. Eosinophil infiltration and heightened airway responsiveness in allergic rabbits, *Am Rev Respir Dis 142*, 587-593.
23. Sherrill, D. L., Stein, R., Halonen, M., Holberg, C. J., Wright, A., and Martinez, F. D. (1999) Total serum IgE and its association with asthma symptoms and allergic sensitization among children, *J Allergy Clin Immunol 104,* 28-36.
24. Sunyer, J., Anto, J. M., Sabria, J., Roca, J., Morell, F., Rodriguez-Roisin, R., and Rodrigo, M. J. (1995) Relationship between serum IgE and airway responsiveness in adults with asthma, *J Allergy Clin Immunol 95,* 699-706.
25. Maccia, C. A., Gallagher, J. S., Ataman, G., Glueck, H. I., Brooks, S. M., and Bernstein, I. L. (1977) Platelet thrombopathy in asthmatic patients with elevated immunoglobulin E, *J Allergry Clin Immunol 59*, 101-108.
26. Moritani, C., Ishioka, S., Haruta, Y., Kambe, M., and Yamakido, M. (1998) Activation of platelets in bronchial asthma, *Chest 113,* 452–458.
27. Buyukyilmaz, G., Soyer, O. U., Buyuktiryaki, B., Alioglu, B., and Dallar, Y. (2014) Platelet aggregation, secretion, and coagulation changes in children with asthma, *Blood Coagul Fibrinolysis 25,* 738-744.
28. Gruba, S. M., Meyer, A. F., Manning, B. M., Wang, Y., Thompson, J. W., Dalluge, J. J., and Haynes, C. L. (2014) Time- and concentration-dependent effects of exogenous serotonin and inflammatory cytokines on mast cell function, *ACS Chem Biol 9*, 503-509.
29. Czapiga, M., Gao, J.-L., Kirk, A., and Lekstrom-Himes, J. (2005) Human platelets exhibit chemotaxis using functional N-formyl peptide receptors, *Exp Hematol 33,* 73-84.
30. Ge, S., Wittenberg, N. J., and Haynes, C. L. (2008) Quantitative and real-time detection of secretion of chemical messengers from individual platelets, *ACS Biochem 47,* 7020-7024.
31. Finkenstaedt-Quinn, S. F., Gruba, S. M., and Haynes, C. L. (2016) Variations in fusion pore formation in cholesterol-treated platelets, *Biophys J 110,* 922-929.
32. Kim, D., Lin, Y. S., and Haynes, C. L. (2011) On-chip evaluation of shear stress effect on cytotoxicity of mesoporous silica nanoparticles, *ACS Anal Chem 83,* 8377-8382.
33. Wu, X., Newbold, M. A., Gao, Z., and Haynes, C. L. (2016) A versatile microfluidic platform for the study of angiogenesis and inflammation, *In Preperation*.
34. Kim, D., and Haynes, C. L. (2012) Neutrophil chemotaxis within a competing gradient of chemoattractants, *Anal Chem 84,* 6070-6078.
35. Mellander, L. J., Trouillon, R., Svensson, M. I., and Ewing, A. G. (2012) Amperometric post spike feet reveal most exocytosis is via extended kiss-and-run fusion, *Sci Rep 2,* 1-6.

36. Ge, S., Woo, E., White, J. G., and Haynes, C. L. (2011) Electrochemical measurement of endogenous serotonin release from human blood platelets, *Anal Chem 83*, 2598-2604.

Chapter 7

1. Page, S., Ammit, A. J., Black, J. L., and Armour, C. L. (2001) Human mast cell and airway smooth muscle cell interactions: implications for asthma, *Am J Physiol-Lung Cell Molec Physiol 281*, L1313-L1323.
2. Metcalfe, D. D., Baram, D., and Mekori, Y. A. (1997) Mast cells, *Physiol Rev 77*, 1033-1079.
3. Bradding, P., Walls, A. F., and Holgate, S. T. (2006) The role of the mast cell in the pathophysiology of asthma, *J Allergy and Clin Immunol 117*, 1277-1284.
4. Theoharides, T. C., Alysandratos, K. D., Angelidou, A., Delivanis, D. A., Sismanopoulos, N., Zhang, B. D., Asadi, S., Vasiadi, M., Weng, Z. Y., Miniati, A., and Kalogeromitros, D. (2012) Mast cells and inflammation, *BBA-Molec Bas Dis 1822*, 21-33.
5. Theoharides, T. C., and Kalogeromitros, D. (2006) The critical role of mast cells in allergy and inflammation, *Neuroendocrine and Immune Crosstalk 1088*, 78-99.
6. Guhl, S., Babina, M., Neou, A., Zuberbier, T., and Artuc, M. (2010) Mast cell lines HMC-1 and LAD2 in comparison with mature human skin mast cells - drastically reduced levels of tryptase and chymase in mast cell lines, *Exp Derm 19*, 845-847.
7. Passante, E., Ehrhardt, C., Sheridan, H., and Frankish, N. (2009) RBL-2H3 cells are an imprecise model for mast cell mediator release, *Inflamm Res 58*, 611-618.
8. Passante, E., and Frankish, N. (2009) The RBL-2H3 cell line: its provenance and suitability as a model for the mast cell, *Inflamm Res 58*, 737-745.
9. Marquis, B. J., and Haynes, C. L. (2008) The effects of co-culture of fibroblasts on mast cell exocytotic release characteristics as evaluated by carbon-fiber microelectrode amperometry, *Biophys Chem 137*, 63-69.
10. Ray, A., and Dittel, B. N. (2010) Isolation of mouse peritoneal cavity cells, *J Vis Exp 35*, doi:10.3791/1488.
11. Manning, B. M., Meyer, A. F., Gruba, S. M., and Haynes, C. L. (2015) Single-cell analysis of mast cell degranulation induced by airway smooth muscle-secreted chemokines, *BBA 1850*, 1862-1868.
12. Gruba, S. M., Koseoglu, S., Meyer, A. F., Meyer, B. M., Maurer-Jones, M. A., and Haynes, C. L. (2015) Platelet membrane variations and their effects on delta-granule secretion kinetics and aggregation spreading among different species, *BBA-Biomemb 1848*, 1609-1618.
13. Meyer, A. F., Thompson, J. T., Wang, Y., Koseoglu, S., Haynes, C. L., and Dalluge, J. J. (2013) Isotope-dilution UPLC-MS/MS determination of mast cell-secreted bioactive lipids, *Analyst 138*, 5697-5705.
14. Blank, U., and Rivera, J. (2006) Assays for regulated exocytosis of mast cells, In *Cur Protoc Cell Biol*, John Wiley & Sons, Inc.
15. Omiatek, D. M., Dong, Y., Heien, M. L., and Ewing, A. G. (2010) Only a fraction of quantal content is released during exocytosis as revealed by electrochemical cytometry of secretory vesicles, *ACS Chem Neurosci 1*, 234-245.
16. O'Connell, P. J., Wang, X. B., Leon-Ponte, M., Griffiths, C., Pingle, S. C., and Ahern, G. P. (2006) A novel form of immune signaling revealed by transmission of the inflammatory mediator serotonin between dendritic cells and T cells, *Blood 107*, 1010-1017.

17. Rudd, M. L., Nicolas, A. N., Brown, B. L., Fischer-Stenger, K., and Stewart, J. K. (2005) Peritoneal macrophages express the serotonin transporter, *J of Neuroimmunol 159*, 113-118.
18. Ahern, G. P. (2011) 5-HT and the immune system, *Cur Opin Pharmacol 11*, 29-33.
19. Blackburn, K. J., French, P. C., and Merrills, R. J. (1967) 5-hydroxytryptamine uptake by rat brain in vitro, *Life Sci 6*, 1653-1663.
20. Blakely, R. D., Berson, H. E., Fremeau, R. T., Caron, M. G., Peek, M. M., Prince, H. K., and Bradley, C. C. (1991) Cloning and expression of a functional serotonin transporter from rat-brain, *Nature 354*, 66-70.
21. Hagan, C. E., Schenk, J. O., and Neumaier, J. F. (2011) The Contribution of low-affinity transport mechanisms to serotonin clearance in synaptosomes, *Synapse 65*, 1015-1023.
22. Neubauer, H. A., Hansen, C. G., and Wiborg, O. (2006) Dissection of an allosteric mechanism on the serotonin transporter: A cross-species study, *Molec Pharmacol 69*, 1242-1250.
23. Daws, L. C., and Toney, G. M. (2007) High-speed chronoamperometry to study kinetics and mechanisms for serotonin clearance in vivo, *Electrochem Meth Neurosci 1*, 63-81.
24. Bradding, P. (2008) Asthma: eosinophil disease, mast cell disease, or both?, *Allergy, Asthma, and Clinic Immunol 4*, 84-90.
25. Brightling, C. E., Ammit, A. J., Kaur, D., Black, J. L., Wardlaw, A. J., Hughs, J. M., and Bradding, P. (2005) The CXCL10/CXCR3 axis mediates human lung mast cell migration to asthmatic airway smooth muscle, *Am J Resp and Critic Care Medic 171*, 1103-1108.

Chapter 8

1. Theoharides, T. C., Alysandratos, K. D., Angelidou, A., Delivanis, D. A., Sismanopoulos, N., Zhang, B. D., Asadi, S., Vasiadi, M., Weng, Z. Y., Miniati, A., and Kalogeromitros, D. (2012) Mast cells and inflammation, *BBA-Mol Basis Dis 1822*, 21-33.
2. Theoharides, T. C., Donelan, J. M., Papadopoulou, N., Cao, J., Kempuraj, D., and Conti, P. (2004) Mast cells as targets of corticotropin-releasing factor and related peptides, *Trends Pharmacol Sci 25*, 563-568.
3. Sutton, B., Beavil, R., and Beavil, A. (2000) Inhibition of IgE-receptor interactions, *Brit Med Bull 56*, 1004-1018.
4. Turner, H., and Kinet, J.-P. (1999) Signalling through the high-affinity IgE receptor FcεRI, *Nature 402*, 24-30.
5. Gruba, S. M., Meyer, A. F., Manning, B. M., Wang, Y., Thompson, J. W., Dalluge, J. J., and Haynes, C. L. (2014) Time- and concentration-dependent effects of exogenous serotonin and inflammatory cytokines on mast cell function, *ACS Chem Biol 9*, 503-509.
6. Manning, B. M., Meyer, A. F., Gruba, S. M., and Haynes, C. L. (2015) Single-cell analysis of mast cell degranulation induced by airway smooth muscle-secreted chemokines, *1850*, 1862–1868.
7. Manning, B. M., Hebbel, R. P., Gupta, K., and Haynes, C. L. (2012) Carbon-fiber microelectrode amperometry reveals sickle cell-induced inflammation and chronic morphine effects on single mast cells, *ACS Chem Biol 7*, 543-551.
8. Kulka, M., Sheen, C. H., Tancowny, B. P., Grammer, L. C., and Schleimer, R. P. (2008) Neuropeptides activate human mast cell degranulation and chemokine production, *Immunol 123*, 398-410.

9. Roosterman, D., Goerge, T., Schneider, S. W., Bunnett, N. W., and Steinhoff, M. (2006) Neuronal control of skin function: the skin as a neuroimmunoendocrine organ, *Physiol Rev 86*, 1309-1379.
10. Maggi, C. A. (1995) Tachykinins and calcitonin gene-related peptide (CGRP) as co-transmitters released from peripheral endings of sensory nerves, *Prog Neurobiol 45*, 1-98.
11. Watkins, H. A., Rathbone, D. L., Barwell, J., Hay, D. L., and Poyner, D. R. (2013) Structure-activity relationships for alpha-calcitonin gene-related peptide, *Br J Pharmacol 170*, 1308-1322.
12. Veres, T. Z., Rochlitzer, S., and Braun, A. (2009) The role of neuro-immune cross-talk in the regulation of inflammation and remodelling in asthma, *Pharmacol Ther 122*, 203-214.
13. Elsenbruch, S. (2011) Abdominal pain in irritable bowel syndrome: a review of putative psychological, neural and neuro-immune mechanisms, *Brain Behav Immun 25*, 386-394.
14. Rosa, A. C., and Fantozzi, R. (2013) The role of histamine in neurogenic inflammation, *Br J Pharmacol 170*, 38-45.
15. O'Connor, T. M., O'Connell, J., O'Brien, D. I., Goode, T., Bredin, C. P., and Shanahan, F. (2004) The role of substance p in inflammatory disease, *J Cell Physiol 201*, 167-180.
16. Holzer, P. (1998) Neurogenic vasodilatation and plasma leakage in the skin, *Gen Pharmacol 30*, 5-11.
17. Birklein, F., and Schmelz, M. (2008) Neuropeptides, neurogenic inflammation and complex regional pain syndrome (CRPS), *Neurosci Lett 437*, 199-202.
18. Black, P. H. (2002) Stress and the inflammatory response: a review of neurogenic inflammation, *Brain Behav Immun 16*, 622-653.
19. Levy, D. (2012) Endogenous mechanisms underlying the activation and sensitization of meningeal nociceptors: the role of immuno-vascular interactions and cortical spreading depression, *Curr Pain Headache Rep 16*, 270-277.
20. Ren, K., and Dubner, R. (2010) Interactions between the immune and nervous systems in pain, *Nat Med 16*, 1267-1276.
21. Kawana, S., Liang, Z., Nagano, M., and Suzuki, H. (2006) Role of substance P in stress-derived degranulation of dermal mast cells in mice, *J Dermatol Sci 42*, 47-54.
22. De Jonge, F., De Laet, A., Van Nassauw, L., Brown, J. K., Miller, H. R., van Bogaert, P. P., Timmermans, J. P., and Kroese, A. B. (2004) In vitro activation of murine DRG neurons by CGRP-mediated mucosal mast cell degranulation, *Am J Physiol Gastrointest Liver Physiol 287*, G178-191.
23. Bischoff, S. C., Schwengberg, S., Lorentz, A., Manns, M. P., Bektas, H., Sann, H., Levi-Schaffer, F., Shanahan, F., and Schemann, M. (2004) Substance P and other neuropeptides do not induce mediator release in isolated human intestinal mast cells, *Neurogastroenterol Motil 16*, 185-193.
24. Lorenz, D., Wiesner, B., Zipper, J., Winkler, A., Krause, E., Beyermann, M., Lindau, M., and Bienert, M. (1998) Mechanism of peptide-induced mast cell degranulation. Translocation and patch-clamp studies, *J Gen Physiol 112*, 577-591.
25. Kim, D., Koseoglu, S., Manning, B. M., Meyer, A. F., and Haynes, C. L. (2011) Electroanalytical eavesdropping on single cell communication, *ACS Anal Chem 83*, 7242-7249.
26. McCary, C., Tancowny, B. P., Catalli, A., Grammer, L. C., Harris, K. E., Schleimer, R. P., and Kulka, M. (2010) Substance P downregulates expression of the high affinity IgE receptor (FcεRI) by human mast cells, *J Neuroimmunol 220*, 17-24.